



## **Master Thesis**

Ida Torkjellsdatter Storehaug

# Improving the Atmospheric Neutrino Flux Estimation in IceCube

Supervisor: Dr. D. Jason Koskinen

September 3, 2019



## Abstract

In neutrino oscillation studies in IceCube, the neutrinos making up the signal are of atmospheric origin. An accurate and precise estimate of the atmospheric neutrino flux is therefore crucial in analyses. In recent IceCube analyses, the uncertainty on the atmospheric neutrino flux is the third-largest source of systematic uncertainty, and the contribution from the atmospheric neutrino flux on the overall systematic uncertainty in IceCube is expected to increase with the IceCube Upgrade. This thesis presents work on developing a more accurate and precise atmospheric neutrino estimate, based on an analytic solution of the cascade equation with MCEq. In this respect, one of the key considerations is the re-interactions of hadrons in the air shower. As part of this work, the event generator PYTHIA has been extended to be used as a hadronic interaction model for air showers. The final result of this work is the development of a new treatment of the atmospheric neutrino flux within low energy analyses in IceCube. A tau neutrino appearance analysis with three years of IceCube data is repeated with the developed method of estimating the atmospheric neutrino flux and its uncertainty. When no other sources of uncertainty are taken into account, the systematic uncertainty on the physics value is improved by around 35%.



# Acknowledgements

I want to thank my supervisor, Jason Koskinen, for introducing me to a field of physics that grows increasingly fascinating. The healthy mix of criticism and encouragement has kept me motivated throughout this year.

I am grateful to Anatoli Fedynitch for his guidance, and I am deeply regretting that I called his program a «black box» the first time we met. It has been a joy to work on MCEq the last year, as it is structured and comprehensive. I am in awe of the intellectual work that has gone into it.

During the spring of 2019, Christian Bierlich contacted the IceCube group with a proposal of extending PYTHIA/Angantyr to air-shower simulations. I want to thank Christian for showing me confidence and guiding me through the project.

I feel privileged for all the physics discussions I've had with the IceCube group members at NBI: Étienne Bourbeau, Thomas Stuttard, Markus Ahlers, Mohammed Rameez, Morten Medici, Lea Halser, Mia-Louise Nilsen and Thomas Schandorf Halberg. I am particularly grateful to Tom Stuttard for all his help. Without his extensive knowledge and educational skills, my thesis would undoubtedly be worse off.

Lastly, thank you, Martin, for reminding me that there is a world outside the office.

# Author's Contributions

The main result presented in this thesis is the development of a new flux stage for the PISA framework, used in low energy ( $E_\nu \lesssim 100$  GeV) IceCube analyses. I wrote the interface between MCEq generated tables and PISA, and performed testing of the new stage. T. Stuttard considerably improved the stage by making it more computationally efficient. The flux stage is based on MCEq, a program authored by A. Fedynich, R. Engel, T.K. Gaisser, F. Riehn and T. Stanev [1].

Chapter 6 reports work done in collaboration with C. Bierlich. C. Bierlich and collaborators have derived the theory of section 6.1, but Section 6.2 and Section 6.3 is my work. All plots of Chapter 6 are made in collaboration with C. Bierlich.

The method of implementing Barr uncertainties in MCEq described in Chapter 7 is written by A. Fedynich. I did the computational setup for restricting the uncertainty on  $\pi^-$  production, and implementing combinations of all sources of uncertainty.

In Chapter 8, I show tests of the flux stage that was developed by T. Stuttard and myself. The stage was applied to the an already compiled tau neutrino appearance analysis on three years of IceCube data.

In general, all plots not made by me are cited with a reference in the figure caption.

# Units and Constants

$c$  Speed of light,  $c = 2.998 \cdot 10^8 \text{ m s}^{-1}$

$b$  A barn is used to express cross sections,  $b = 10^{-28} \text{ m}^2$

$\hbar$  Planck constant,  $\hbar = 1.055 \cdot 10^{-34} \text{ Js} = 6.582 \cdot 10^{-16} \text{ GeV}$

$eV$  Electron-volt,  $1 \text{ eV} = 1.602 \cdot 10^{-19} \text{ J}$

$G_F$  Fermi constant,  $G_F = 1.663787(6) \cdot 10^{-5} \text{ GeV}^{-2}$

$e$  Elementary charge,  $e = 1.602\,176\,634 \cdot 10^{-19} \text{ C} \approx 0.302\,822\,121 \sqrt{\hbar c}$

**Natural units** provide a well-motivated basis for expressing quantities in particle physics. The use of natural units entails omitting constants from mathematical expressions of physical laws, i.g., by choosing  $\hbar = c = 1$ . In this way, all quantities are expressed in GeV, as shown in Table 0.1. Natural units are used throughout this thesis.

**Table 0.1.** – Relationship between S.I. and natural units

Quantity	[kg, m, s]	$[\hbar, c, \text{GeV}]$	$\hbar = c = 1$
Energy	$\text{kg m}^2 \text{s}^{-2}$	GeV	GeV
Momentum	$\text{kg m s}^{-1}$	GeV/ $c$	GeV
Mass	kg	GeV/ $c^2$	GeV
Time	s	$(\text{GeV}/\hbar)^{-1}$	$\text{GeV}^{-1}$
Length	m	$(\text{GeV}/\hbar c)^{-1}$	$\text{GeV}^{-1}$
Area	$\text{m}^2$	$(\text{GeV}/\hbar c)^{-2}$	$\text{GeV}^{-2}$

# Contents

<b>Acknowledgements</b>	<b>iii</b>
<b>Author's Contributions</b>	<b>iv</b>
<b>Units and Constants</b>	<b>v</b>
<b>1 Introduction</b>	<b>1</b>
<b>2 Neutrinos in the Standard Model and Beyond</b>	<b>3</b>
2.1 The Standard Model of Particle Physics . . . . .	3
2.2 Neutrino Properties . . . . .	5
2.3 Neutrino Oscillations . . . . .	6
2.4 Neutrinos Beyond the Standard Model . . . . .	8
2.5 Neutrino-Nucleus Interactions . . . . .	8
<b>3 The IceCube Detector</b>	<b>11</b>
3.1 Cherenkov Radiation . . . . .	11
3.2 The Detector Medium . . . . .	12
3.3 Digital Optical Module (DOM) . . . . .	12
3.4 Detector Layout . . . . .	13
3.5 Event Signatures in DeepCore . . . . .	14
3.6 Neutrino Oscillation Studies in DeepCore . . . . .	17
3.7 The IceCube Upgrade . . . . .	18
<b>4 Atmospheric Neutrinos</b>	<b>20</b>
4.1 Cosmic Rays . . . . .	20
4.2 Air Showers . . . . .	21
4.3 The Cascade Equation . . . . .	22
4.4 Overview of Neutrino Flux Calculations . . . . .	25
4.5 The Geomagnetic Field and the Azimuth Dependence of the Neutrino Flux . . . . .	28
4.6 The Atmospheric Density and Zenith Dependence of the Neutrino Flux . . . . .	30
<b>5 Calculating the Atmospheric Neutrino Flux with MCEq</b>	<b>32</b>
5.1 Inclusive and Exclusive Neutrino Flux Estimates . . . . .	32
5.2 Hadronic Interaction Models . . . . .	32
5.3 Limits of MCEq . . . . .	33

5.4	The Matrix Cascade Equation . . . . .	34
5.5	The Inputs of MCEq . . . . .	36
5.5.1	Hadron-air cross section . . . . .	36
5.5.2	Decay Length . . . . .	36
5.5.3	Reinterctions in the Air Shower . . . . .	36
5.5.4	Energy Loss . . . . .	37
5.6	The Physical Models of MCEq . . . . .	38
<b>6</b>	<b>PYTHIA/Angantyr as an Interaction Model in Atmospheric Flux Calculations</b>	<b>39</b>
6.1	Deriving the Cross Section . . . . .	39
6.2	Introducing Kaon Projectiles . . . . .	42
6.3	Comparing the Kaon-proton Cross Section to Data . . . . .	44
6.4	Kaon-nucleus Collisions . . . . .	47
6.5	Implementation in MCEq and Outlook . . . . .	48
<b>7</b>	<b>Uncertainties on the Atmospheric Neutrino Flux</b>	<b>50</b>
7.1	Uncertainties on the Particle Production . . . . .	50
7.1.1	Comparing Hadronic Interaction Models . . . . .	50
7.1.2	The Barr Scheme . . . . .	51
7.1.3	The Barr Scheme in MCEq . . . . .	54
7.1.4	Spread in Interaction Model is Sub-dominant . . . . .	56
7.2	Uncertainties on the Cosmic Ray Flux . . . . .	57
7.3	Overall Uncertainty on the Atmospheric Neutrino Flux . . . . .	58
7.4	Uncertainties of Neutrino Ratios . . . . .	59
<b>8</b>	<b>Implementation of MCEq in PISA</b>	<b>64</b>
8.1	The PISA Framework . . . . .	64
8.2	The Honda Flux Stage . . . . .	65
8.3	A New Flux Stage in PISA . . . . .	67
8.4	Flux Nuisance Parameters . . . . .	68
8.5	The MCEq stage vs. the Honda stage . . . . .	72
8.6	Atmospheric Tau Neutrino Appearance in DeepCore . . . . .	74
<b>9</b>	<b>Summary and Outlook</b>	<b>77</b>
	<b>List of Figures</b>	<b>79</b>
	<b>List of Tables</b>	<b>81</b>
	<b>List of Abbreviations</b>	<b>82</b>
	<b>Appendices</b>	<b>85</b>
<b>A</b>	<b>Derivation of Oscillation Probability</b>	<b>86</b>
<b>B</b>	<b>Models of MCEq</b>	<b>89</b>
B.1	Hadronic Interaction Models in MCEq . . . . .	89

---

B.2	Density Profile of the Atmosphere . . . . .	89
B.3	Cosmic Ray Models . . . . .	89
<b>C</b>	<b>Theory of the Angantyr Model</b>	<b>91</b>
C.1	Diffractive Cross Sections . . . . .	91
C.2	Distribution of T . . . . .	92
<b>D</b>	<b>Results on the Atmospheric Electron Neutrino Flux</b>	<b>93</b>
<b>E</b>	<b>Breakdown of Uncertainties on Neutrino Ratios</b>	<b>98</b>
<b>F</b>	<b>Atmospheric Flux Nuisance Parameters</b>	<b>99</b>
	<b>References</b>	<b>99</b>

*«I have done a terrible thing, I have postulated a particle that cannot be detected.» [2]*

Wolfgang Pauli first postulated the neutrino in 1930. He called his idea *«a desperate remedy»*[3], and the problem it was supposed to remedy was a puzzling observation in the measurements of  $\beta$ -decay. At the time it was believed that the atom consisted of equal numbers of electrons and protons, and thus  $\beta$ -decay would be a two-body decay. If energy, spin, and momentum are conserved, one can expect discrete emission lines in a two-body decay. This was indeed observed in  $\alpha$ - and  $\gamma$ -decay, and it came as a surprise when J. Chadwick discovered a continuous energy spectrum of electrons emitted in  $\beta$ -decay [4].

In an attempt to save the laws of conservation, Pauli suggested that *«... there could exist in the nuclei electrically neutral particles... which have spin 1/2 and obey the exclusion principle, and additionally different from light quanta in that they do not travel with the velocity of light»*[3]. When emitted, the theorized particle, later named the *neutrino*, would carry away some of the energy, causing a continuous energy spectrum of the emitted electron. Today we know  $\beta$ -decay to be the process of  $n \rightarrow p + e^- + \bar{\nu}_e$ .

Contrary to Pauli's beliefs, the neutrino could be detected. This was done by C. Cowan and F. Reines in 1956 [5]. Using neutrinos from the Hanford reactor (and later at the Savannah River Plant), they studied inverse  $\beta$ -decay:  $\bar{\nu}_e + p \rightarrow e^+ + n$ . The cross section for this reaction is tiny, but it has a unique signature: the positron quickly annihilates with an electron producing two coincident  $\gamma$ -rays, and after a delay, a neutron capture reaction produces a third  $\gamma$ -ray.

The anti-electron neutrino discovered by Cowan and Reines is only one of several neutrino flavors. In 1962 it was demonstrated by Lederman, Schwartz, and Steinberger that the electron neutrino,  $\nu_e$ , differs from the muon neutrino,  $\nu_\mu$  [6]. The tau neutrino,  $\nu_\tau$ , was later observed by the DONUT experiment in 2000 [7].

In our proximity, the largest producer of neutrinos is the Sun. In nuclear fusion chains, like the the proton-proton cycle,  $2 \cdot 10^{38} \nu_e$  are produced each second [8]. The Homestake experiment, placed in a mine in South Dakota, was originally designed to confirm the fusion reactions in the Sun, by measuring the electron neutrino flux [9]. The detector was a 615-ton tank of dry cleaning fluid,  $C_2Cl_4$ . When the electron neutrino interacted with the chlorine atoms a radioactive isotope of argon was produced via inverse  $\beta$ -decay:  $\nu_e + Cl_{17}^{37} \rightarrow Ar_{18}^{37} + e^-$ . The radioactive argon isotopes were extracted from the tank and counted, providing a number for  $\nu_e$  interactions. However, they observed only  $\sim 30\%$  of the expected number of events. This deficit of electron neutrinos became known as the *solar neutrino problem*.

Experimental proof of the theory solving the problem was found at Sudbury Neutrino Observatory (SNO)[10] and at Super-Kamiokande (SK)[11] around 2000. Taking advantage of different ways of detecting neutrinos, SNO was sensitive to both the electron neutrino flux *and* the total neutrino flux. The total neutrino flux matched the prediction, but they found the same 60% deficit of the

electron neutrino flux as earlier experiments, implying a large component of muon and/or tau neutrinos in the total solar flux. Since  $\nu_\mu/\nu_\tau$  cannot be produced in the fusion chains of the Sun, SNO provided clear evidence of neutrino oscillations: Electron neutrinos are produced in the Sun but change flavor as they propagate toward the Earth.

The neutrino is a mysterious particle. We do not know its mass, or whether it is its own antiparticle. It is quite a paradox that although so little is known about the neutrino, it is the second most abundant particle in our Universe. Every second 100 trillion neutrinos pass through your body, without ever interacting<sup>1</sup>. The topic of this thesis is how that number – or the flux, being the number of neutrinos per area over a certain time interval – is calculated. I am studying a subset of the neutrinos that flow through your body: those that are created in the atmosphere.

Many experiments study neutrino oscillations by observing how the flavor ratio of atmospheric neutrinos changes over distance. However, it is useless to study the change of a system without knowing its initial state. In this thesis, methods of estimating that initial state are presented. Though most of the work presented is generally applicable, it has been done with the intention of being used in the IceCube experiment.

IceCube is the world's largest neutrino detector and is located at the South Pole. When its data is being used for oscillation studies, the signal is atmospheric neutrinos that have propagated through the Earth. My task in that regard has been to estimate the flux of neutrinos at the surface of the Earth, prior to potential oscillation. In recent analyses, the uncertainty on the atmospheric neutrino flux has been one of the largest sources of systematic uncertainty. I have intended to limit this uncertainty, and thus provide an accurate and precise estimate of the atmospheric neutrino flux.

Though sometimes used for oscillation studies, IceCube was designed to search for astrophysical sources of neutrinos. Atmospheric neutrinos are a source of background in these searches, and limiting the uncertainty on the background will result in more sensitive measurements.

---

<sup>1</sup>The number varies quite a bit (which is another reason why we need good flux estimates – so master students know which number to quote!). This estimate is taken from <https://icecube.wisc.edu/news/view/546>

The objective of this chapter is to answer the question: What is a neutrino? In Section 2.1, the neutrino will be described within a Standard Model of extremely reduced complexity, focusing on the weak force. The concepts developed are then used to list some of the properties of the neutrino in Section 2.2. We will see that the neutrino exhibits some properties that are not predicted by the Standard Model – they oscillate (Section 2.3) – forcing us to modify, or even move beyond, the Standard Model (Section 2.4). Sometimes being dubbed «the ghost particle», the neutrino has eluded scientists ever since its discovery. In Section 2.5, we will see why giving an overview of how neutrinos interact with matter.

## 2.1 The Standard Model of Particle Physics

The Standard Model is a relativistic quantum field theory that describes the interactions between elementary particles. The four types of interactions observed are the electromagnetic, weak, strong, and gravitational forces. The Standard Model does not describe the latter, but the three former can be described mathematically as relativistic quantum fields.

Particles are often called the building blocks of nature, but in the framework of quantum field theory nature consists of fields, and particles are just excited states (or quanta) of those underlying fields. If fields are to interact, the fundamental physics of the quantum field must be unchanged by transformation. The group of transformations, called gauge transformations, that leaves the field invariant is called a symmetry group. For each generator of the group, there arises a corresponding field. The quanta of these fields are the integer spin bosons. The bosons can be understood as «force-carriers», mediating the interactions between matter particles, described as fermion fields. As seen in Figure 2.1, fermions include all quarks and leptons.

**The electromagnetic force** (QED) is a U(1) symmetry and has one generator giving rise to one field, which quantum is the photon. According to Noether's theorem, there is a conserved quantity for each symmetry. For the U(1) group, the conserved quantum number is electric charge. The photon couples to the charged leptons ( $e^-$ ,  $\mu^-$ ,  $\tau^-$ ) and the quarks, also having electric charge.

**The strong force** The conserved charge of the strong force is color. QCD is a SU(3) symmetry group, meaning that it has eight generators, corresponding to eight gluons. Unlike the photon, gluons are self-interacting, and therefore, colored objects are confined: no objects of non-zero color charge can propagate as free particles. Quarks, having color charge, must combine to form *hadrons*. The quarks that contribute to the quantum numbers of the hadrons are called *valence quarks*, and they are some of the *partons* of the hadrons. A hadron with baryon number 0 is a combination of a valence quark and anti-quark and is called a *meson*. A hadron with baryon number 1 consists of three quarks and is called a *baryon*. Leptons do not have color charge and are hence not confined.

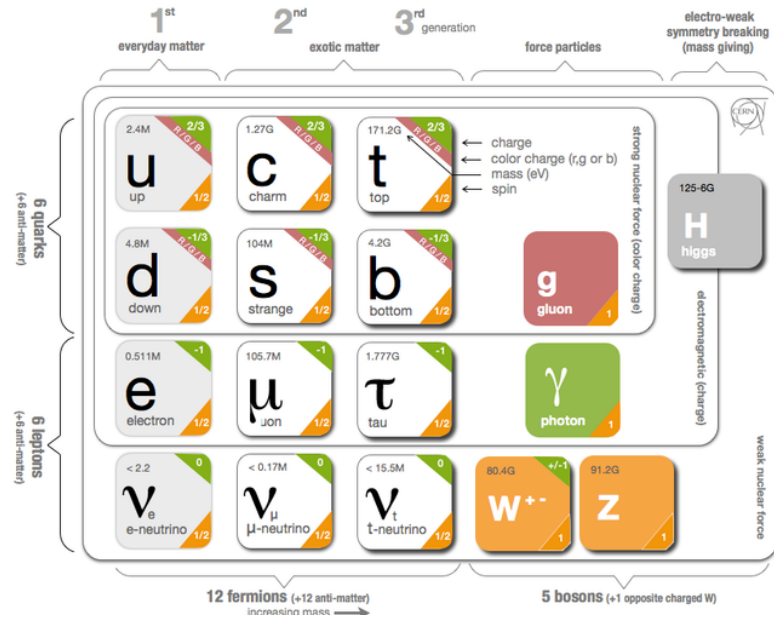


**Figure 2.1.** – Graphical depiction of the Standard Model. Figure from [12]

**The weak force** SU(2) conserves weak isospin and has three generators,  $W^{\pm,0}$ . The weak force is observed to be parity-violating. Conservation of parity means that the laws of physics are invariant if the spatial coordinates of a system are inverted through the origin. This entails that it is impossible to distinguish right from left and clockwise from counter-clockwise. The weak force does, however, see «left» and «right». By «left» and «right» I mean a fundamental property of the particle, called *chirality*, which is related to how the wave function of a particle behaves when it is rotated. For massless particles, the chirality coincides with the *helicity*, which is the projection of the particle spin onto the direction of momentum. The nature of the  $W^{\pm}$ -boson is such that it will only couple to left-handed particle chiral states and right-handed antiparticle chiral states.

Despite its name, the weak force is intrinsically stronger than the electromagnetic force, with a coupling constant of  $\alpha_w \sim 1/30$ , compared to  $\alpha \sim 1/137$ . To explain why the weak force appears weaker than the QED force at low-energy scales, we must introduce heavy mediators. To illustrate this, consider the  $\beta$ -decay process of  $n \rightarrow p + e^- + \bar{\nu}_e$ . Increasing the level of detail, this is the process of a neutron emitting a  $W^-$  boson, which decays into  $e^-$  and  $\bar{\nu}_e$ . If the  $W^-$  boson is massive, the process is more likely to happen once the momentum transfer,  $q$ , is around, or higher, than the mass of the boson. Thus, at small momentum transfer, the probability of this interaction happening is very small, and the force appears weak. When the momentum transfer is much larger than the mass of the mediating boson, the weak force and QED will be of similar strength.

**The electroweak force** The similarity of the coupling strength at high energy points to the underlying physics: at high energy QED and weak force are unified, in a  $U(1) \otimes SU(2)$ -symmetry group, with four generators. The physical bosons are linear combinations of the four fields that arise, in such a way that the  $W^{\pm}$  boson is a combination of fields from the weak interaction gauge group, whereas

the  $Z$  boson and  $\gamma$  boson are mixtures of the third field associated with the weak interaction gauge group and the field associated with QED. Thus the  $Z$  boson couples to both left- and right-handed chiral states, but not equally.

**The Higgs mechanism** Introducing massive mediators of the weak force, breaks the electroweak symmetry<sup>1</sup>. To avoid this, the Higgs mechanism spontaneously breaks the symmetry by introducing a Higgs field, that «slows down» the particles of weak charge, giving them mass.

All of the fermions fall into three «generations»: particles of the same quantum numbers, but differentiated by mass. The quark and lepton fields also couple to the Higgs field, and acquire mass through spontaneous symmetry breaking. The strength of the coupling determines the mass. The physics of this is not yet fully understood. We will see that the picture is even more complicated for neutrinos.

With the introduction of the Higgs mechanism, the Standard Model assumed the form we know today, as a  $SU(3)\otimes SU(2)\otimes U(1)$  symmetry group.

## 2.2 Neutrino Properties

We now turn to the neutrino and its properties, using some of the notions explained above.

**Quantum numbers** A neutrino is an electrically neutral spin 1/2 fermion. It carries an empirically defined lepton number, resulting in three different flavor states: electron neutrino ( $\nu_e$ ), muon neutrino ( $\nu_\mu$ ), and tau neutrino ( $\nu_\tau$ ). From measurements of the  $Z$  boson width at LEP, we know that there are no additional neutrino flavors that interact weakly [14].

The neutrino is unaffected by QED as it has no charge, and QCD as it has no color. As it only interacts weakly, the neutrino is never directly detected, unlike charged leptons, which can be detected from the ionization track they leave in matter. The neutrino flavor is therefore defined by the charged lepton that contributes to the interaction. As an example  $\nu_e$  is *defined* as the neutrino state produced along with an electron. It follows that no flavor can be assigned for a neutrino in propagation or interacting with a  $Z$  boson.

**Chirality and mass** As neutrinos interact through the weak force, which is parity-violating, only left-handed neutrinos and right-handed antineutrinos have been observed. The Standard Model only postulates the existence of left-handed neutrinos (right-handed antineutrinos). The Standard Model also determines the neutrinos to be massless.

All fermions have an associated antiparticle with the same mass but opposite physical charges. However, the right-handed neutrino (left-handed antineutrino) has no gauge charge, and can potentially be its own antiparticle. In this case the neutrino is a *Majorana* fermion, as opposed to a *Dirac* fermion.

---

<sup>1</sup>As shown by 't Hooft, only theories with local gauge invariance are renormalizable, meaning that if the invariance is broken unitarity violation, e.g. in the  $W^+W^- \rightarrow W^+W^-$  cross section, will arise[13].

## 2.3 Neutrino Oscillations

For years it was believed that  $\nu_e$ ,  $\nu_\mu$ , and  $\nu_\tau$  were massless fundamental particles. However, the solar neutrino problem can only be solved if neutrinos oscillate. *Neutrino oscillations* does here refer to the periodic change of the probability of a neutrino being created with flavor  $\alpha$  to be later detected as flavor  $\beta$ . For such a phenomenon to occur, the neutrino must propagate in a basis different to that in which it interacts, and interference among the states should occur during propagation.

The neutrino interacts as a flavor eigenstate  $\nu_\alpha$ , which is defined by the charged lepton involved in the interaction vertex:  $\alpha = e, \mu, \tau$ . The flavor eigenstate is, however, a superposition of the mass eigenstates,  $\nu_k$ .

$$|\nu_\alpha\rangle = \sum_k U_{\alpha k}^* |\nu_k\rangle, \quad (2.1)$$

where  $U_{\alpha k}$  are elements of the unitary Pontecorvo-Maki-Nakagawa-Sakata (PMNS) mixing matrix [15]. The PMNS matrix can be parameterized by three rotations  $\theta_{12}$ ,  $\theta_{13}$ , and  $\theta_{23}$  and three complex phases  $\delta$ ,  $\alpha_1$ , and  $\alpha_2$ .

$$U_{\text{PMNS}} = \begin{pmatrix} 1 & 0 & 0 \\ 0 & c_{23} & s_{23} \\ 0 & -s_{23} & c_{23} \end{pmatrix} \begin{pmatrix} c_{13} & 0 & s_{13}e^{-i\delta} \\ 0 & 1 & 0 \\ -s_{13}e^{i\delta} & 0 & c_{13} \end{pmatrix} \begin{pmatrix} c_{12} & s_{12} & 0 \\ -s_{12} & c_{12} & 0 \\ 0 & 0 & 1 \end{pmatrix} \cdot \text{diag}(e^{i\alpha_1/2}, e^{i\alpha_2/2}, 1), \quad (2.2)$$

where  $s_{ij} = \sin \theta_{ij}$  and  $c_{ij} = \cos \theta_{ij}$ . The last matrix, depending on  $\alpha_1$  and  $\alpha_2$ , is only included if neutrinos are Majorana particles.

**Neutrino oscillations in vacuum** A physical description of neutrino oscillations require that the particles are described as wave packets. This is mathematically complicated, and in the following we will treat the particle as a plane wave, to develop the idea. The Schrödinger equation implies that the neutrino mass states evolve in time,  $t$ , as plane waves<sup>2</sup>

$$|\nu_k(t)\rangle = e^{-iE_k t} |\nu_k\rangle, \quad (2.3)$$

where  $E_k$  is the energy of mass state  $\nu_k$ . The flavor state  $|\nu_\alpha(t)\rangle$  is a neutrino of flavor  $\alpha$  created at  $t=0$ . From equation (2.1) and (2.3) the flavor state will evolve in time like:

$$|\nu_\alpha(t)\rangle = \sum_k U_{\alpha k}^* e^{-iE_k t} |\nu_k\rangle. \quad (2.4)$$

Since  $U$  is unitary,  $U^\dagger U = \mathbf{1} \equiv \sum_\alpha U_{\alpha k}^* U_{\alpha j} = \delta_{jk}$ , where  $\delta$  is the Kronecker delta function. Thus we can invert equation (2.1)

$$|\nu_k\rangle = \sum_\alpha U_{\alpha k} |\nu_\alpha\rangle. \quad (2.5)$$

<sup>2</sup>This derivation follows closely that of C. Giunti and C.W. Kim [16]

Substituting equation (2.5) into equation (2.4), we obtain

$$|\nu_\alpha(t)\rangle = \sum_{\beta=e,\mu,\tau} \left( \sum_k U_{\alpha k}^* e^{-iE_k t} U_{\beta k} \right) |\nu_\beta\rangle. \quad (2.6)$$

Hence, though the initial flavor state was  $|\nu_\alpha(t)\rangle$  at  $t=0$ , it has become a superposition of different flavor states at  $t > 0$ , given that the matrix  $U$  is not diagonal. The transition probability is

$$P_{\nu_\alpha \rightarrow \nu_\beta}(t) = |\langle \nu_\beta | \nu_\alpha(t) \rangle|^2 = \sum_{k,j} U_{\alpha k}^* U_{\beta k} U_{\alpha j} U_{\beta j}^* e^{-i(E_k - E_j)t}. \quad (2.7)$$

As neutrinos are ultra-relativistic we can make two assumptions: (1) they travel at the speed of light so we can approximate  $t = L$ , (2)  $E_k$  can be approximated as  $E_k \approx E + m_k^2/2E$ , where  $E = |\vec{p}|$ . In this case

$$E_k - E_j \approx \frac{\Delta m_{kj}^2}{2E}, \quad (2.8)$$

where  $\Delta m_{kj}^2 \equiv m_k^2 - m_j^2$ . In this approximation the transition probability of equation (2.7) is

$$P_{\nu_\alpha \rightarrow \nu_\beta}(L, E) = \sum_{k,j} U_{\alpha k}^* U_{\beta k} U_{\alpha j} U_{\beta j}^* \exp\left(-i \frac{\Delta m_{kj}^2 L}{2E}\right). \quad (2.9)$$

In Appendix A it is shown that equation (2.9) can be written as

$$\begin{aligned} P_{\nu_\alpha \rightarrow \nu_\beta}(L, E) = & \delta_{\alpha\beta} - 4 \sum_{k>j} \text{Re}(U_{\alpha k}^* U_{\beta k} U_{\alpha j} U_{\beta j}^*) \sin^2\left(\frac{\Delta m_{kj}^2 L}{4E}\right) \\ & \pm 2 \sum_{k>j} \text{Im}(U_{\alpha k}^* U_{\beta k} U_{\alpha j} U_{\beta j}^*) \sin\left(\frac{\Delta m_{kj}^2 L}{2E}\right), \end{aligned} \quad (2.10)$$

where  $\delta$  is the Kronecker delta function. The sign of the imaginary part depends on whether neutrinos (+) or antineutrinos (-) are being considered.

The frequency of the oscillation probability is determined by  $L$ ,  $E$ , and the mass squared difference  $\Delta m_{kj}^2$ , the latter being a physical constant. The amplitude of the oscillation probability is determined by the elements of the mixing matrix  $U$ , which are fundamental constants.

There are two take-away messages from this derivation: (1) The free parameters of the oscillation probability are the neutrino energy  $E$  and the propagation length  $L$ , and (2) if a transition is to occur there must be a mass difference  $\Delta m_{kj}^2 \neq 0$ . The latter notion implies that neutrinos must have mass to oscillate.

Note that equation (2.10) is derived for a neutrino propagating in vacuum. When neutrinos propagate through matter, they can scatter coherently with electrons in the matter, giving an additional potential that will affect the oscillation probabilities. One type of matter effect is *Mikheyev-Smirnov-Wolfenstein*[17].

## 2.4 Neutrinos Beyond the Standard Model

Within the Standard Model, neutrinos do not have mass. Yet, as seen in the previous section, neutrinos must have mass to oscillate. Thus neutrino oscillations are one of the only experimental deviations from the otherwise successful Standard Model.

The neutrino mass can be introduced in the Standard Model in the same way as for other fermions, i.e., with the Higgs mechanism. This can be done by introducing a new fermion field for a right-handed chiral neutrino that is completely neutral under  $U(1) \otimes SU(2)$ . When coupling to the Higgs field, this would yield a neutrino mass, presumably comparable to that of the electron. However, neutrino masses are extremely small. The most stringent upper bounds on the  $\bar{\nu}_e$  mass is  $m_{\bar{\nu}_e} < 2.05$  eV (at 95% CL), and cosmological data indicate  $\sum_j m_j \lesssim (0.3\text{--}1.3)$  eV (at 95% CL) [17]. This would imply an unnaturally small coupling to the Higgs field. While this is possible, the *seesaw mechanism* provides an attractive explanation for the smallness of the neutrino masses.

**The seesaw mechanism** Because the right-handed chiral neutrinos (left-handed chiral antineutrinos) transform as singlets under Standard Model gauge transformations, we can introduce mass to these fields alone without breaking the gauge invariance, via a Majorana mass term. The right-handed chiral neutrinos (left-handed chiral antineutrinos) can couple to left-handed neutrinos (right-handed antineutrinos) with a Dirac mass term, that is generated through the Higgs mechanism and have a similar size as the other fermions,  $\mathcal{O}(1)$  eV. The Majorana mass is not arising from the Higgs mechanism, and is therefore expected to be tied to some energy scale of new physics beyond the Standard Model,  $\mathcal{O}(10^{15})$  eV. Thus, any process involving right-handed neutrinos will be suppressed at low energies. The corrections due to the suppression effectively give the left-handed neutrino a mass that is inversely proportional to the right-handed Majorana mass. This mechanism would explain both the smallness of the left-handed neutrino and the absence of right-handed neutrinos in observation.

**Neutrino mass ordering** It is not only the mechanism behind the neutrino mass which is an open question. The absolute values of the neutrino masses are also unknown. Vacuum oscillations depend on the (squared) mass difference in a sine or cosine function, equation (2.10). Thus, the oscillation probabilities are insensitive to the sign of the (squared) mass difference. In other words, neither the absolute mass nor the ordering of the neutrino mass states can be derived from vacuum neutrino oscillation studies. We can either have *normal* ( $\Delta m_{32}^2$  is larger than  $\Delta m_{21}^2$ ) or *inverted* ordering (the other way around).

## 2.5 Neutrino-Nucleus Interactions

The neutrino interacts only via the weak force (and gravitationally). The weak interaction is either mediated by the  $W^\pm$  boson, in a so-called charged current (CC) interaction, or by the Z boson in a neutral current (NC) interaction. In a charged current interaction, the neutrino is converted to the corresponding charged lepton (left diagram of Figure 2.2a). In a neutral current interaction, the

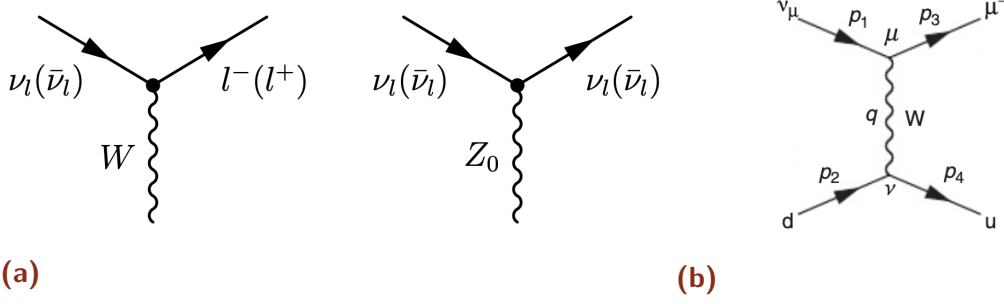


**Figure 2.2.** – (a) Neutrinos can interact weakly either via charged current (left) or neutral current (right) interactions. (b) The diagram of a neutrino-quark scattering interaction. From [18].

neutrino can change energy and momentum but is not converted (right diagram of Figure 2.2a). It will be useful for later discussions of the experimental setup of IceCube to review how neutrinos interact with matter in the relevant energy regime. Matter consists of both leptons and hadrons, but as the electron-neutrino cross section is tiny, it will be ignored henceforth.

**CC neutrino-quark scattering** In the energy range relevant for this work,  $E_\nu \gtrsim 10$  GeV, neutrinos dominantly interact with hadrons through deep inelastic scattering (DIS). This means that the neutrino is scattering on the constituents of the hadrons within the atomic nucleus. The nucleon is then broken apart and the quarks hadronize. Figure 2.3 shows that deep inelastic scattering is the only significant interaction above 100 GeV. The measurements show that at high energies the cross section is almost independent of the energy, confirming that the neutrinos are indeed scattering of partons.

An example of a deep inelastic scattering process is  $\nu_\mu + d \rightarrow \mu^- + u$ , depicted in Figure 2.2b. A muon neutrino with four-momentum  $p_1$  scatters off a quark within the nucleon with four-momentum  $p_2$ , and a muon and a different quark, with momentum  $p_3$  and  $p_4$  respectively, are produced in the interaction. Looking at the diagram of Figure 2.2b, we can define some variables that will be useful in later chapters

$$s \equiv (p_1 + p_2)^2 \quad (\text{center-of-mass energy}), \quad (2.11)$$

$$-Q^2 \equiv q^2 \equiv (p_1 - p_3)^2 \quad (\text{momentum transfer}), \quad (2.12)$$

$$x \equiv \frac{Q}{2p_2 \cdot q} \quad (\text{elasticity of interaction}). \quad (2.13)$$

As the  $W^\pm$  boson only couples to left-handed chiral states, the only possible combination in the neutrino-quark scattering of Figure 2.3 is  $LL \rightarrow LL$ . In the low energy range where  $|q|^2 \ll m_W^2$ , the strength of the weak interaction is given by the Fermi constant,  $G_F$ . Assuming that the energy of the neutrino is much

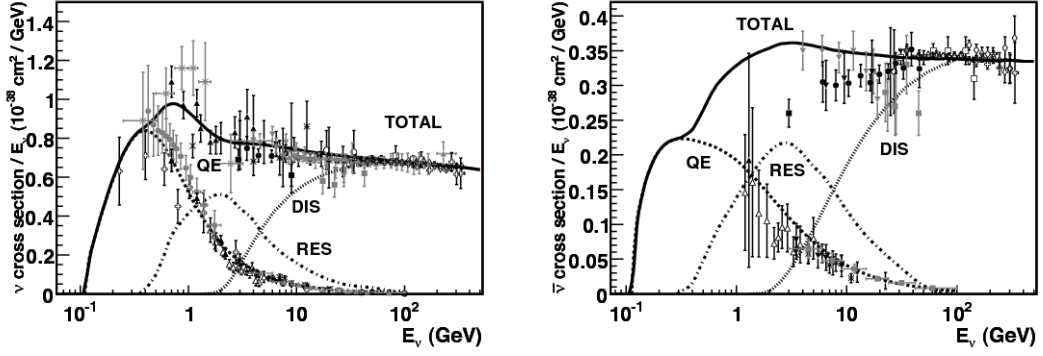


**Figure 2.3.** – Total neutrino (left) and antineutrino (right) per nucleon charged current cross sections divided by neutrino energy and plotted as a function of energy. From [19].

larger than the mass of the contributing lepton,  $E_\nu \gg m_l$ , the total cross section for neutrino-quark scattering is given by

$$\sigma = \frac{G_F^2 s}{\pi}. \quad (2.14)$$

Note that the cross section grows linearly with center-of-mass energy,  $s$ . It can be shown that due to the chiral nature of the weak force the cross section of antineutrino-quark scattering,  $\bar{\nu}_\mu + u \rightarrow \mu^+ + d$ , is three times smaller than the neutrino-quark cross section. As seen in Figure 2.3, this translates to a considerably smaller cross section for antineutrino-nucleus charged current interactions (right), when compared to neutrino-nucleus CC interactions (left).

The strength of the weak force in the low energy range is given by

$$G_F = \frac{\sqrt{2}g_W^2}{8m_W^2} = 1.1663787(6) \times 10^{-5} \text{GeV}^{-2}, \quad (2.15)$$

which means that the neutrino-quark cross section is tiny. As the neutrino only interacts weakly with matter, the neutrino cross section with matter is extremely small compared to that of other elementary particles. In the next chapter, we will see how this property puts specific requirements on the experimental setup of neutrino experiments.

The detection of neutrinos is always challenging due to their small cross section. A huge detector volume is required to observe a significant number of neutrinos. The IceCube Neutrino Observatory is the largest neutrino detector in the world and uses about a cubic kilometer of the glacial ice sheet at the South Pole as a detection medium. It has been fully operational since 2011. Its primary scientific objective has been the search for neutrinos originating from outside our solar system, which was achieved in 2013 [20]. The physics program also includes studies of neutrino oscillations, supernova detection, dark matter detection, and searches for exotic particles.

## 3.1 Cherenkov Radiation

When neutrinos hit the ice molecules, charged particles are produced, either in CC interactions or in the hadronic cascade from DIS NC interactions. As a charged particle transverses the ice, it will polarize the molecules along its track, since ice is a dielectric medium. After its passage, the molecules will return to the unpolarized state through the emission of photons. The photons will travel at a phase speed of light in the medium,  $v_\gamma = c/n$ ,  $n$  being the index of refraction of the medium. If the velocity of the particle is greater than the speed of light in that medium  $v_p > c/n$ , constructive interference occurs. The coherent wavefront emitted is called Cherenkov radiation[21]. The IceCube detector is based on the observation of this Cherenkov emission.

Cherenkov radiation has two characteristics: (1) photons are emitted a unique angle, and (2) it has a particular frequency spectrum.

In figure 3.1, a charged particle travels in a medium with speed  $v_p = \beta c$ ,  $\beta = v_p/c$ . In time  $t$ , the particle travels a distance  $x_p = \beta ct$ . In this time the wavefront emitted at  $t = 0$  has traveled a distance of  $x_\gamma = (ct)/n$ . The emission angle  $\theta_c$  is therefore

$$\cos \theta_c = \frac{x_\gamma}{x_p} = \frac{1}{n\beta}. \quad (3.1)$$

In ice the emission angle – or Cherenkov angle – is around  $40^\circ$ .

Cherenkov radiation has a continuous frequency spectra: the intensity increases with increasing frequency up to a certain cut-off. The cut-off occurs when equation (3.1) is no longer satisfied. As the refractive index is dependent on the frequency,  $n$  will approach zero at high frequencies – around x-ray frequencies. Therefore, most Cherenkov radiation is in the ultraviolet region of the electromagnetic spectrum. It can also extend down to the visible region and is then observed as blue light.

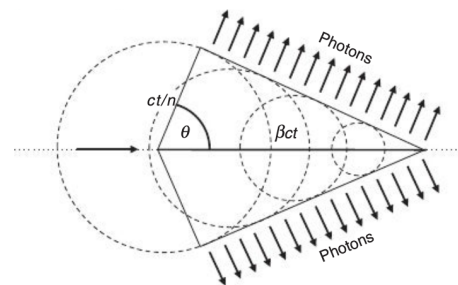


**Figure 3.1.** – Geometry of Cherenkov radiation [18].

## 3.2 The Detector Medium

The IceCube detector is located at the South Pole, and detect Cherenkov emission initiated by neutrinos interacting with the Antarctic ice. The Antarctic glacier is formed from snow compressed under its own weight for millions of years. In ice Cherenkov photons mostly scatter off air molecules. However, under pressure air bubbles in the ice get embedded in the ice molecules, and effectively disappear. Thus, the ice is very clear below a depth of 1400 m[22]. Photons can then propagate hundreds of meters, and less dense instrumentation is required to measure them[23]. Hence it is feasible to instrument a large, uniform volume, which is required to measure the rarely interacting neutrino.

The slow formation of the glacier results in extremely low levels of radioactivity – which is a source of background signal[24]. Another source of background is muons produced in cosmic ray interactions in the atmosphere. In order to take advantage of both of the clear ice and the shielding from the glacier above, IceCube is buried kilometers below the surface.

The trajectories of the Cherenkov photons are affected by scattering and absorption. Measurements of the optical properties of the ice within IceCube, indicate an anisotropy, caused by the alignment of ice molecules[23]. This empirical observation is taken into account when modeling the scattering properties of the ice. When the contribution from air molecules can be neglected, the rate of absorption is determined by the length transversed in ice and the presence of impurities in the ice – *dust*. Most notably there exists a *dust layer*, between 2000 and 2100 m below the surface. In this region, the absorption and scattering of photons are much higher. Beneath the dust layer, the ice is at its clearest.

When deploying instrumentation into the ice, the ice in the hole will re-freeze. The process results in a *bubble column* along the string. The *hole ice* with the bubble column is a significant systematic uncertainty in IceCube.

## 3.3 Digital Optical Module (DOM)

In IceCube the Cherenkov photons are detected using *digital optical modules* (DOM). The DOM is the fundamental detector unit in IceCube and converts light in the ice into an electronic signal. The main components of a DOM are a 25.4 cm downward-facing photomultiplier tube (PMT), a mainboard containing the necessary electronics to supply power and digitize the signal, an array of light-emitting diodes (LED), and a 33 cm glass sphere, which encloses all of the above (Figure 3.2). The LEDs are used for calibration purposes, like verifying the timing response of the DOMs, measuring the relative position of the DOMs, measuring the optical properties of the ice, and verifying the performance of reconstruction methods. The glass sphere hangs in a cable by a harness and is designed to withstand a pressure of 250 bar.

**Photomultiplier Tube** The detection of a photon starts when it crosses the glass sphere of the DOM, and enters a gel that is used to optically couple the sphere and the PMT. Once in the PMT, the photon can be absorbed by a photocathode, emitting an electron by the photoelectric effect. The efficiency of this process –

the quantum efficiency – is around 25%[24]. The electron is multiplied in a series of dynodes, yielding a total amplification of the signal of  $10^7$ . The signal is read out as a change in voltage of the PMT anode. The PMTs are sensitive to photons with a wavelength between 300 nm and 650 nm, coinciding with the wavelength range of Cherenkov radiation in ice.

**Digitization** If the voltage at the PMT anode exceeds a threshold of 25% of the voltage peak of a single electron, a «launch» is triggered. A time series of measured charge – the *waveform* – is digitized by three circuits running in parallel; two analogue transient waveform digitisers (ATWD) and one fast analogue-to-digital converter (fADC). There are two ATWDs in case the DOM is hit again while the first ATWD is still digitizing. The ATWDs have a high sampling resolution, 3.3 ns, and a recording duration of 427 ns. The high resolution is required for the event reconstruction algorithms to determine the position of the photons at low precision. The fADC has a lower rate, but a maximum recording duration of 6400 ns.

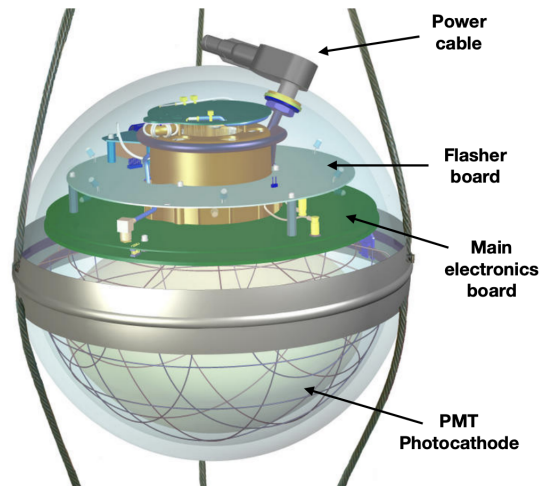


Figure 3.2. – Schematic of a DOM.

**Local Coincidence** If a DOM launches it communicates with the nearest and next-to-nearest neighbor to determine if any of these DOMs have also launched within  $\pm 1 \mu\text{s}$ . If two or more DOMs fulfill the criteria, they are in *hard local coincidence*, and a full waveform from both the ATWD and the fADC is compressed and included in the readout. If the DOM launches but does not fulfill the criteria of local coincidence the readout is done in a low-resolution mode only.

The detector observables are the charge  $Q$  deposited in the DOM during a time interval  $t + \Delta t$ . Reconstructing the energy and direction of an event entails piecing together the observables from several DOMs.

## 3.4 Detector Layout

The DOMs are arranged in strings, deployed on a triangular grid with 125 m horizontal spacing, making up a hexagonal footprint when seen from above (Figure 3.3).

**The in-ice array** The in-ice array is deployed between 1450 m and 2450 m below the surface of the ice[24]. It consists of 86 strings. Each string consists of 60 DOMs, with a vertical separation of 17 m. The in-ice array is designed for the detection of astrophysical neutrinos with energy between  $\mathcal{O}(1)$  TeV and  $\mathcal{O}(1)$  PeV and has an lower energy threshold of around  $E_\nu = 50\text{--}100$  GeV[24].

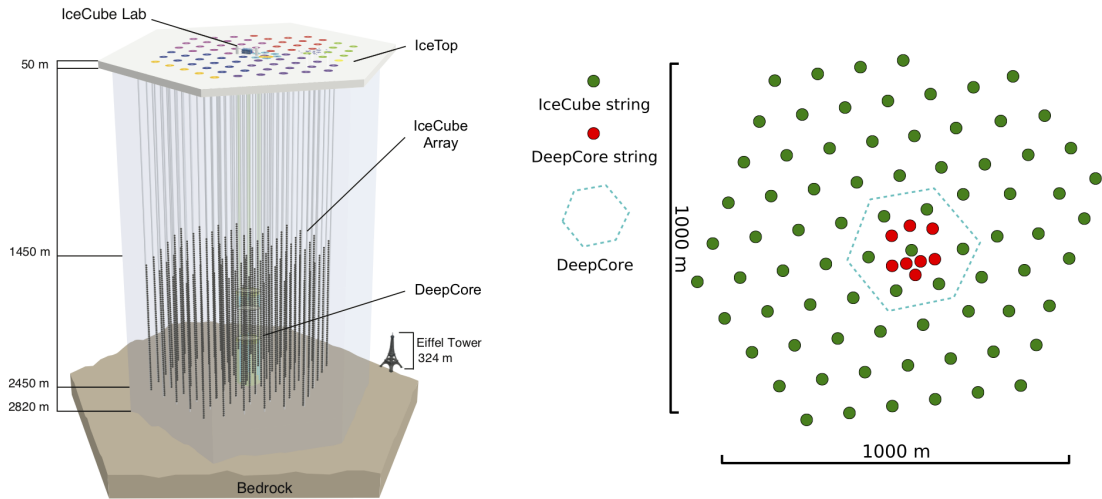


**Figure 3.3.** – Layout of the IceCube detector. From [25].

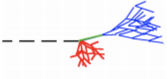
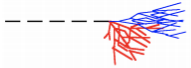
**DeepCore** A subset of the in-ice DOMs makes up the DeepCore sub-array. This subset is deployed below the dust-layer where the ice is at its clearest, approximately in the center of the in-ice array. DeepCore consists of 8 specialized strings of sensors and 7 of the central standard IceCube strings [26]. The strings are more densely spaced, separated by 41 m to 105 m. The DOMs of the 8 specialized strings have a 7 m vertical separation and a 35% higher quantum efficiency than the standard IceCube DOMs. DeepCore utilizes the rest of the IceCube detector to veto background muons from the atmosphere. The denser geometry and increased efficiency result in a lower energy threshold of  $E_\nu \sim 10$  GeV. With this lower energy threshold, DeepCore can be used for atmospheric neutrino oscillation studies.

**IceTop** IceTop is located on the surface of the ice and consists of 162 ice-filled tanks, arranged in 81 stations, using approximately the same grid on which the in-ice array is deployed. Each tank consists of two DOMs. IceTop serves as a veto for the detection of downward-going neutrinos in IceCube but is also used for cosmic ray studies.

### 3.5 Event Signatures in DeepCore

By using the information recorded by each DOM – the charge  $Q$  and time  $t$  – one can reconstruct the energy and direction of the neutrino that initiated the Cherenkov emission. However, in neutrino oscillation studies, one also needs to know the neutrino flavor. Unique identification of flavor in water Cherenkov detectors can be difficult, and sometimes impossible, but an indication can be found in the event signature. Figure 3.4 depicts the signatures that can be expected for different deep inelastic scattering neutrino interactions in DeepCore.

**Particle energy loss in matter** The particles produced in the deep inelastic scattering interactions of neutrinos and ice molecules, will lose energy as they propagate through the ice. Energy loss in matter is of relevance to later chapters, which

Interaction		Secondary particles	Detector signature
CC $\nu_\mu$		$\mu$ track and hadronic cascade	Track with cascade
CC $\nu_\tau$		$\tau$ decays into $\mu$ ( $\sim 17\%$ b.r.)	
		$\tau$ decays into $e$ / hadrons	
CC $\nu_e$		Hadronic and EM cascades	Cascade
NC $\nu_\alpha$		Hadronic cascade	

**Figure 3.4.** – Possible experimental signatures of neutrino interaction in DeepCore. Dashed lines represent neutrinos, orange lines are muons, red lines are particles originated in a hadronic cascade and blue lines are electrons and photons. From [27].

justifies the following brief overview. If the produced particle – the secondary – is charged and sufficiently energetic, it can interact electromagnetically with the atoms in the ice, causing the atom to lose an electron and thus ionize. The energy loss through ionization per unit length traversed,  $dE/dx$ , is modeled by the Bethe-Block formula, which shows that  $dE/dx \propto 1/v^2$ . Thus the energy loss through ionization is larger for low-velocity particles.

Above a critical energy, the charged secondary will lose energy through *bremstrahlung*, whereby it radiates a photon in the electrostatic field of a nucleus. If the produced photon is sufficiently energetic,  $E_\gamma > 10$  MeV, it will pair produce  $e^-e^+$  in the field of a nucleus. Thus a cascading process of *bremstrahlung* and pair production is initiated: an electromagnetic shower. The length of the shower is defined in terms of radiation lengths, i.e., the average distance over which the electron loses  $1/e$  energy due to *bremstrahlung*. When the average energy of the electrons, positrons, and photons in the shower falls below the critical energy, they will start to lose energy through ionization.

*Bremstrahlung* occurs for all charged particles but is inversely proportional to the square of the particle mass. This entails that lighter particles lose more energy through *bremstrahlung*. Hence the muon rate of energy loss by *bremstrahlung* is suppressed by  $(m_e/m_\mu)^2$  relative to that of electrons, and only become a significant at  $E_\mu > 100$  GeV.

Charged hadrons lose energy through ionization as they travel through matter, but they can additionally lose energy in strong interactions with nuclei of the ice, and produce particles. These particles will again interact strongly with nuclei

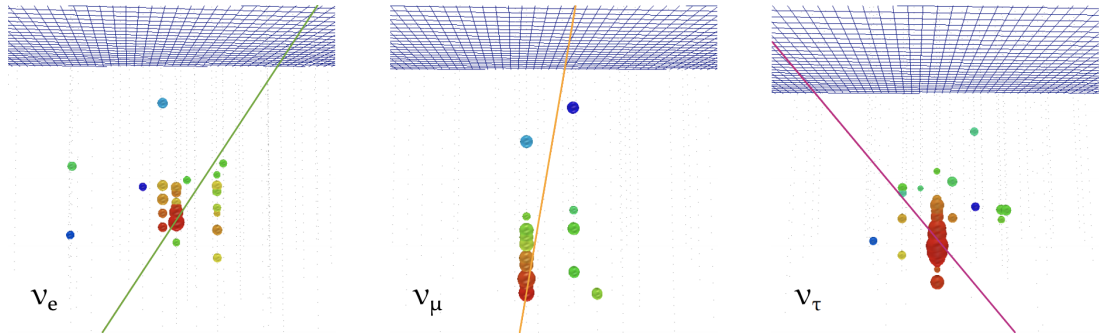


**Figure 3.5.** – Event view of  $\nu_e$ ,  $\nu_\mu$  and  $\nu_\tau$  for a typical DeepCore neutrino energy of 50 GeV. The color represent the time-stamp for the hit, red being earlier hits and green later. The size of the dot represents the deposited charge. Figure from [29].

downstream, giving rise to a cascade of particles: a hadronic shower. The mean distance between hadronic interactions is given by the nuclear interaction length,  $\lambda_{\text{int}}$ . The nuclear interaction length is longer than the radiation length, and the hadronic shower will thus be more extended than the electromagnetic shower.

**Cascade** Electromagnetic showers are produced in CC  $\nu_e$  and some CC  $\nu_\tau$  interactions (blue showers of Figure 3.4). Hadronic showers are produced in all deep inelastic neutrino interactions (red showers of Figure 3.4). As the electromagnetic shower, in general, is more contained than the hadronic shower, it can overlap with the hadronic cascade, making them indistinguishable. However, the distance between DOMs is large compared to both the hadronic and electromagnetic shower volume, and the light pattern spreads out almost spherically – resulting in a *cascade event*. Cascade events are often entirely contained within the detector, resulting in good energy resolution. For NC events the energy reconstruction is biased toward lower energies, as some energy is carried away by the undetectable neutrino.

The decay of leptons is mediated by the weak interaction exclusively. It can be shown that the mean lifetime,  $\tau_l$ , at low energy,  $m_l \ll m_W$ , is  $\tau_l \propto 1/(G_F^2 m_l^5)$ . Thus the relatively high mass tau lepton produced in CC tau neutrino interactions will decay quickly to produce a cascade event.

**Tracks** The muon does, (1) not lose energy quickly through bremsstrahlung, and (2) have a longer lifetime than the tau lepton due to the mass difference. Thus it will travel significant distances through the ice, resulting in a *track event*. This unique signature entails that the muon is the only particle from neutrino interactions that can be identified with some confidence in IceCube. Muons are produced in the CC interaction of  $\nu_\mu$ , and in some cases, the tau lepton from a CC  $\nu_\tau$  interaction decays to a muon ( $\sim 17\%$  BR) [28]. At DeepCore energies, the angular resolution of tracks is generally better than for cascades. The energy resolution is usually worse, particularly at high energy, since the muon track might not be contained within the detector volume.

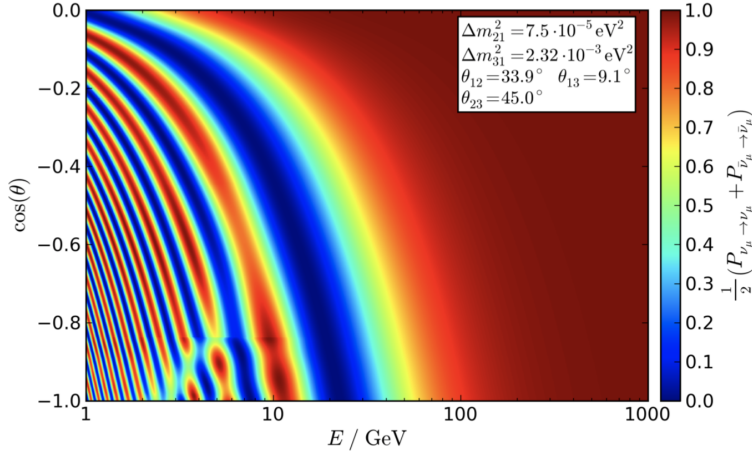


**Figure 3.6.** – The survival probability of muon neutrinos (averaged over  $\nu_\mu$  and  $\bar{\nu}_\mu$ ) as a function of zenith angle and energy. Figure from [31].

In general events at higher energy show much more well-defined topologies, resulting in clearer event signatures in the main IceCube array than in DeepCore. Even muon tracks can be so short at DeepCore energies that they are easily mistaken for cascade events. Figure 3.5 shows some typical event views of  $\nu_\mu$ ,  $\nu_e$ , and  $\nu_\tau$  events, for neutrino energy of around 50 GeV.

## 3.6 Neutrino Oscillation Studies in DeepCore

IceCube is designed as a neutrino observatory, meaning that its main science goal is the observation of astrophysical neutrinos. To shield for cosmic ray background, IceCube is designed to be more sensitive to upward-going neutrinos. The PMTs of the DOMs are facing downward and measure Cherenkov radiation initiated by neutrinos that have traveled through the Earth. The oscillation probability of equation (2.10) is dependent on the neutrino path lengths,  $L$ , and the neutrino energy,  $E_\nu$ . The neutrino path lengths in IceCube – the *baseline* of oscillation – range from 10 km to 12 700 km, depending on the zenith arrival angle,  $\theta_z$ , of the neutrino.

Given the range of baselines, one can in principle observe oscillations of neutrinos with  $1 \text{ GeV} \lesssim E_\nu \lesssim 25 \text{ GeV}$ . However, due to background rejection and reconstruction, DeepCore has an energy threshold. In recent IceCube analyses, the event sample extended down to 5.6 GeV [30]. Thus, there is a lower limit to the zenith arrival direction of neutrinos undergoing oscillations that can be observed with DeepCore.

There are two possible signatures of neutrino oscillations: *appearance*, i.e., observation of neutrino flavors not expected unless oscillation occurs, and *disappearance*, i.e., observation of fewer neutrinos of a particular flavor than expected, unless oscillation occurs.

**$\nu_\mu + \bar{\nu}_\mu$  disappearance** Because of the large mass splitting of  $\Delta m_{32}^2$ , the strongest flux modification that oscillations produce is muon neutrino disappearance. The

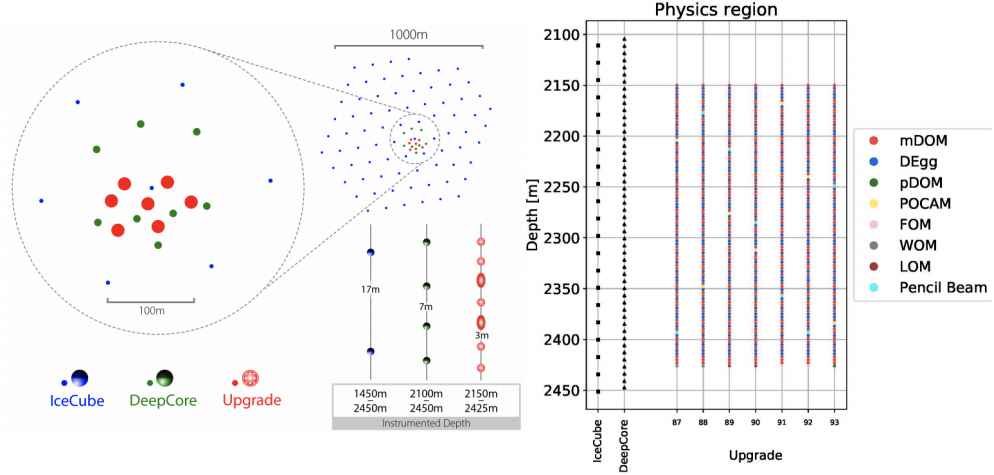


**Figure 3.7.** – The Upgrade array geometry. Red marks on the left panel shows the layout of the 7 IceCube Upgrade strings with the IceCube high-energy array (blue) and its sub-array DeepCore (green). The right panel shows the depth of sensors/devices for the IceCube Upgrade array. The different colors represent different optical modules and calibration devices. From [33].

survival probability of a muon neutrino as a function of path length through the Earth is shown in Figure 3.6. For the largest baseline,  $\cos \theta_z = -1$ , there is a maximum  $\nu_\mu$  disappearance at about 25 GeV. At lower energies, the maximum shifts towards a more horizontal direction.

Based on the muon neutrino disappearance observation, with three years of data of neutrinos with energy between 10 GeV and 100 GeV, IceCube has put limits to the mass splitting,  $\Delta m_{32}^2$ , and the mixing angle,  $\sin^2 \theta_{23}$  [30].

**$\nu_\tau$  appearance** Because of the smallness of  $\Delta m_{13}^2$  the wavelength of the oscillation probability of  $E_\nu \leq 10$  GeV is too large to be detectable over the baseline of the Earth, and  $\nu_\mu \rightarrow \nu_e$  is negligible. Thus, muon neutrinos that disappear appear as tau neutrinos in the detector, and the maximum  $\nu_\mu$  disappearance is matched by a maximum  $\nu_\tau$  appearance at 25 GeV. The latest measurement of tau neutrino appearance was published in 2019 and is the topic of Section 8.6 [30].

### 3.7 The IceCube Upgrade

Recently, the IceCube collaboration received funding for an upgrade, to be deployed in the 2022/2023 Antarctic summer season [32]. The Upgrade consists of seven new strings, embedded near the bottom center of the existing layout, between 2150 m and 2425 m below the surface (Figure 3.7) [33]. The instrumentation will be much more dense, with a horizontal spacing of 20 m and vertical spacing of 3 m [33]. The strings will consist of around 700 optical sensors, and new optical sensors will be deployed: Multi-PMT Digital Optical Module (mDOM) and Dual optical sensors in an Ellipsoid Glass for Gen2 (D-Egg) [33]. There are three science goals of the Upgrade:

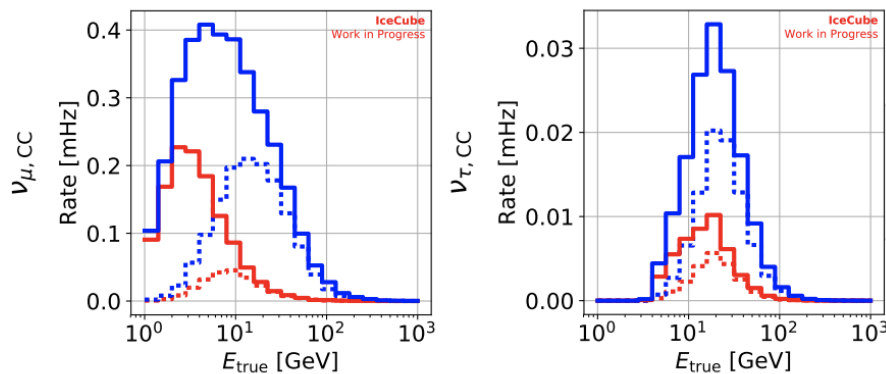


**Figure 3.8.** – Fully contained atmospheric  $\nu_\mu$  (left) and  $\nu_\tau$  (right) in the DeepCore (dashed lines) and Upgrade (full line) arrays, at analysis level event selection. Red is the inner fiducial area ( $r = 50$  m) and blue is the outer fiducial area ( $r = 145$  m). From [33].

**More Sensitive Oscillation Studies** The Upgrade entails denser and more efficient instrumentation. As a result, the DeepCore sensitivity at low energies will be improved, and one will be able to measure photons from interactions of neutrinos with energy  $\mathcal{O}(1)$  GeV [33]. Figure 3.8 shows a significant enhancement in the event rates below 30 GeV for muon neutrinos (left) in the Upgrade array (full lines) compared to the present day DeepCore (dashed lines). As the enhancement is in energy regions relevant for oscillation studies, DeepCore will have an overall improved sensitivity to oscillation effects.

The right plot of Figure 3.8 shows that a considerably larger rate of  $\nu_\tau$  will be detected after the Upgrade, as the discrimination between tracks and cascades will be improved compared to DeepCore. Both due to a larger sample and improved reconstruction, the sensitivity to  $\nu_\tau$  appearance will increase. The Upgrade strings will surpass the precision of the world’s most accurate measurement of  $\nu_\tau$  appearance by a significant amount [33].

**Improved Calibration** The understanding of the ice properties, how the DOMs function *in situ*, and how the hole around each string re-freezes is limited – since the DOMs cannot be investigated once they are installed. This is a significant source of systematic uncertainty in studies of astrophysical neutrinos.

One goal of the Upgrade is to improve calibration. Each optical module of the Upgrade strings encloses several calibration devices, such as LEDs and cameras. In between the modules, stand-alone emitters are also planned to be deployed. With the new calibration, ten years of data can be re-analyzed with a smaller systematic uncertainty. Combined with a better angular resolution, this will result in improved sensitivity in searches for astrophysical point sources.

**R&D for IceCube Gen-2** The upgrade is also a development platform for the future. There are plans to expand IceCube to IceCube Gen-2, an 8 km<sup>3</sup> neutrino detector, to improve the sensitivity in astrophysical point source searches[34]. The plan is to use smaller sensors, to reduce costs, and these can be tested in the Upgrade.

Within the energy range that DeepCore is sensitive to, naturally occurring neutrinos are of atmospheric origin. In the following chapter, I will present the properties of the atmospheric neutrino flux, and provide an outline of how these properties can be derived.

Atmospheric neutrinos are produced when cosmic rays (Section 4.1) collide with particles in the atmosphere and initiate air showers (Section 4.2). The production modes of atmospheric neutrinos result in a characteristic flavor composition of the flux (Section 4.4). The flux also exhibits an azimuthal dependency due to the geomagnetic field (Section 4.5), and a zenith and seasonal dependence due to the atmosphere of the Earth (Section 4.6).

## 4.1 Cosmic Rays

Cosmic rays consist of about 90% protons, 9% helium nuclei, and the rest being heavier nuclei. The nuclei are accelerated up to extremely high energies in astrophysical sources, the nature of which is still unknown, and is the topic of intense research.

The observed cosmic ray flux covers an energy range from below  $10^9$  eV up to several  $10^{20}$  eV. To perform measurements over 11 orders of magnitude in energy, a variety of different detection methods must be utilized. Below  $\sim 100$  TeV, cosmic rays are measured directly in air-borne or satellite experiments, such as AMS[35], PAMELA[36], ATIC-2[37], CREAM[38] and TRACER[39]. At higher energies, cosmic rays are measured indirectly, through air shower experiments like the Pierre Auger Observatory[40] and KASCADE-Grande[41].

In Figure 4.1, the all-particle cosmic ray flux, as measured by air-borne, satellite, and air shower experiments is plotted. The spectrum exhibits some features, and cannot be described by a single power law. At lower energies, it is observed that a power law of  $E^{-\gamma}$ ,  $\gamma \approx 2.7$ , can describe the cosmic ray spectra. At around 3 PeV – the so-called «knee» – there is a steepening of the spectrum caused by the spectral index changing to  $\gamma \approx 3.1$ . At about 3 EeV there is a softening of the spectrum, called the «ankle», with  $\gamma \approx 2.7$ .

The most popular theory is that transitions from different sources of acceleration cause the broken power laws of the cosmic ray spectrum. As first pointed out by B. Peters[43], there is a maximal energy to which particles can be accelerated, which depends on the rigidity  $R = Pc/(Ze)$ , where  $P$  is the total momentum of the nucleus and  $Ze$  is its electrical charge. A cut-off will first be observed in the proton flux. Following this, a cut-off is expected on the helium, carbon, and so on, flux at energies equal to the electric charge of the nuclei times the maximum energy of an accelerated proton.

Most attempts to parametrize the cosmic ray spectrum are based on the theory by B. Peters. Several models are assembled series of «Peter cycles»: broken power-laws with rigidity dependent cut-offs. Examples of these are the H3a[44], the GST-3/GST-4[45] and the Gaisser-Honda[46] model, further described in

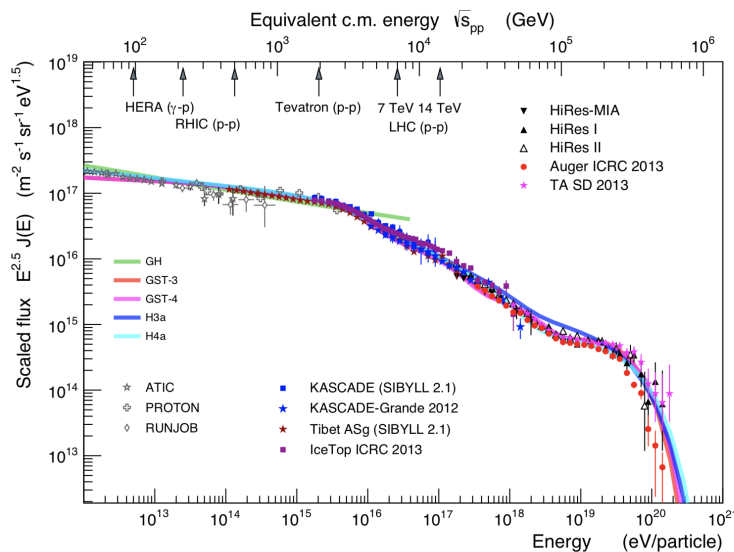


**Figure 4.1.** – All-particle cosmic ray spectrum. Experimental results plotted as dots. The lines are obtained from parametrizations. Figure from [42] by R. Engel.

Appendix B. The resulting all-particle spectrum predicted by the various models is superimposed on air shower data in Figure 4.1.

In contrast to the mentioned models, the *Global Spline Fit* does not build on any theoretical assumptions[65]. Rather than being based on power-laws and rigidity dependent cut-offs, the approach of splining between data from measurements is taken. Thus the only assumption is a smoothly varying flux.

## 4.2 Air Showers

The energy of the cosmic ray particles far exceeds the binding energy of the air molecules in the atmosphere. As a cosmic ray collides with an atom in the atmosphere, the atom will break up in a deep inelastic scattering interaction, resulting in a hadronic and an electromagnetic cascade. The height at which the cosmic ray-air collision occurs will vary with the density of the atmosphere but is often  $\mathcal{O}(10-20)$  km above the surface of the Earth.

**Electromagnetic cascade** The most abundant particles in the cascade are the lightest mesons: pions and kaons. When the pions re-interact there is a 30% probability of producing a neutral pion, which almost exclusively decays to photons and electrons. Thus, the hadronic cascade also feeds an electromagnetic component of the shower. Since most hadrons re-interact, most of the energy of the cosmic ray eventually finds its way into the electromagnetic component. Hence, most of the energy of the air shower is dissipated by ionization losses of electrons and positrons. However, for the scope of this work, the electromagnetic component is of little interest: it rarely converts energy back to neutrinos. As the electromagnetic component of the air shower gives a negligible contribution to the neutrino flux, it will henceforth be ignored.

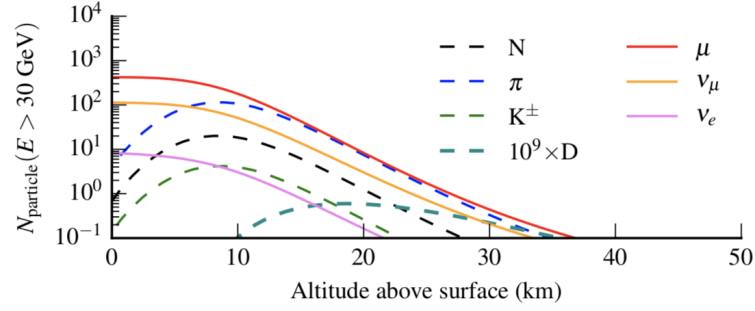


**Figure 4.2.** – The curves represent the average particle number per cascade, counting all particles with an energy above 30 GeV for an incoming proton at  $45^\circ$  zenith angle and 10 PeV energy. Figure from unpublished work by A. Fedynitch and R. Engel [47].

**Hadronic cascade** As for the hadronic component, hadrons can re-interact to create sub-cascades or decay. The number of particles in the shower will reach a maximum, after which the shower attenuates as fewer and fewer particles in the shower have enough energy to produce secondaries. In Figure 4.2, one can see that the number of mesons in a shower initiated at around 35 km above the surface is drastically reduced at altitudes smaller than 10 km above the ground. However, muons, due to their long lifetime, and neutrinos, due to their small cross section, will reach the ground. Figure 4.2 demonstrates this effect by the monotonic increase of the muon and neutrino particle density.

### 4.3 The Cascade Equation

As the oscillation probability depends on the energy of the neutrino, we are interested in the energy spectrum of neutrinos and define the flux as a differential expression

$$\Phi_h = \frac{d\phi_h}{dE} = \frac{dN_h}{dEdAd\Omega dt}, \quad (4.1)$$

where  $A$  is a differential area and  $\Omega$  is a differential angle. The number of particle species  $h$ ,  $h = \pi^+, \pi^-, K^+, \dots$ , is  $N_h$ .

Now, imagine that you choose a small volume of the atmosphere, and count the number of particles at a certain time interval as an air shower transverses the imagined volume. The change of number of particles of type  $h$  over the time interval is described by the Boltzmann equation:  $dN_h = f(\mathbf{r}, \mathbf{p}, t)d^3\mathbf{r}d^3\mathbf{p}$ , where  $f$  is a probability density function and  $d^3\mathbf{r}d^3\mathbf{p}$  is the volume of atmosphere and momentum space. The number of particles of type  $h$  can either increase or decrease over the time interval. The number would decrease as particles of type  $h$  decay into particles of type  $k$ , or as particles of type  $h$  interact with air molecules and produce particles of type  $k$ . When counting over a momentum space, the number can also decrease as particles of type  $h$  lose energy. However, the number of particles of type  $h$  can also increase: particles of type  $k$  can enter

the imagined volume and decay into particles of type  $h$ , or as they enter, interact with air molecules and produce particles of type  $h$ .

Rather than describing the development of the shower in terms of time, we can differentiate with respect to the *slant depth*. The slant depth is the amount of material penetrated by the shower and is calculated by integrating the density of the air from the height at which the air shower is initiated to the altitude in question,  $h_0$ .

$$X(h_0) = \int_0^{h_0} dl \rho_{\text{air}}(l), \quad (4.2)$$

where  $l$  is the path length and  $\rho$  is the air density. For a homogeneous medium, the slant depth is simply the density multiplied with the path length,  $X = l\rho$ . However, the density of the atmosphere varies. How this affects the integral is further discussed in Section 4.6.

To sum up, three processes can cause the number of particles of type  $h$  to decrease, and two processes can lead to an increase. This five-term linear Boltzmann transport equation in terms of slant depth is termed *the cascade equation*.

$$\frac{d\Phi_h(E, X)}{dX} = - \frac{\Phi_h(E, X)}{\lambda_{\text{int},h}(E)} \quad (4.3a)$$

$$- \frac{\Phi_h(E, X)}{\lambda_{\text{dec},h}(E, X)} \quad (4.3b)$$

$$- \partial_E(\mu(E)\Phi_h(E, X)) \quad (4.3c)$$

$$+ \sum_k \int_E^\infty dE_k \frac{dN_{k(E_k) \rightarrow h(E)}}{dE} \frac{\Phi_k(E_k, X)}{\lambda_{\text{int},k}(E_k)} \quad (4.3d)$$

$$+ \sum_k \int_E^\infty dE_k \frac{dN_{k(E_k) \rightarrow h(E)}^{\text{dec}}}{dE} \frac{\Phi_k(E_k, X)}{\lambda_{\text{dec},k}(E_k, X)}. \quad (4.3e)$$

In the following, I will go through each term of the cascade equation, explaining all variables.

**The first sink term (4.3a)** model the loss of particles of type  $h$  due to interactions with air nuclei. The rate of particle interaction is expressed as the flux of particle  $h$  divided by the average distance traveled by a particle between two successive collisions, i.e., *the interaction length*

$$\lambda_{\text{int},h}(E) = \frac{\langle m_{\text{air}} \rangle}{\sigma_{\text{p-air}}^{\text{inel}}(E)}. \quad (4.4)$$

The air-molecule is approximated as an average reflecting the atmospheric composition of oxygen and nitrogen nuclei, meaning that  $\langle m_{\text{air}} \rangle = 14.5 m_p$ , where  $m_p$  is the proton mass. As seen in Figure 4.3a, the inelastic cross section for baryons and mesons grows with energy. As the cross section increases with energy, the interaction length will decrease with energy (dashed line of Figure 4.3b).

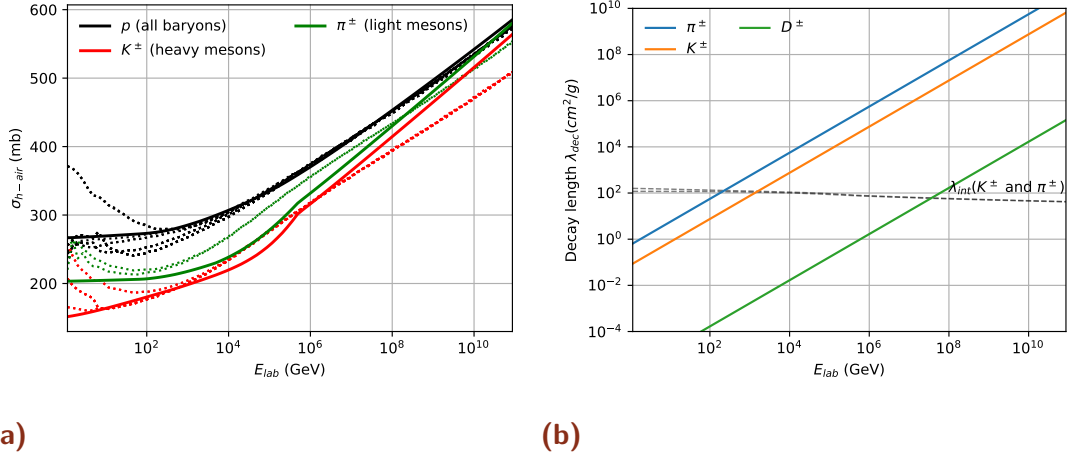


**Figure 4.3.** – (a) Hadron-air cross section as calculated with the DPMJET-III (dashed lines) and SIBYLL2.3c interaction models (see Section 5.2). The black curves represent all baryons, green curves all light mesons and red curves all heavy mesons. The collision energy in the rest frame of the air molecule is  $E_{lab}$ . (b) Decay lengths for a selection of hadrons. Superimposed is the interaction length  $\lambda_{int}$  of  $K^\pm$  and  $\pi^\pm$ .

**The second sink term (4.3b)** models the loss of particles of type  $h$  due to decay into particles of type  $k$ . The average distance a particle travels before decay is expressed in the decay length

$$\lambda_{dec}^h(E, X) = \frac{c\tau_h E \rho_{air}(X)}{m_h}, \quad (4.5)$$

where  $\tau_h$  and  $m_h$  is the lifetime and mass of particle  $h$  respectively.

In Figure 4.3b I have plotted the decay length  $\lambda_{dec}^h \approx (c\tau_h E)/m_h$ . Since the lifetime is dilated for ultra-relativistic particles, a proportionality to  $E$  is introduced, visible as a near-linear dependence of  $\lambda_{dec}^h$  on  $E$ . The  $D^\pm$  meson has a lifetime five orders of magnitude smaller than that for charged pions.

The intersection in Fig. 4.3b, where  $\lambda_{dec} = \lambda_{int}$ , is the critical energy,  $\epsilon$ .

$$\epsilon_h(\rho_{air}) = \frac{m_h c^2 \rho_{air}}{c\tau_h}. \quad (4.6)$$

As an example, charged pions have a critical energy of  $\epsilon \approx 115$  GeV. Below 115 GeV the decay length is smaller than the interaction length, and charged pions tend to decay. Charged pions with an energy higher than 115 GeV are more likely to interact with air nuclei and initiate sub-cascades than to decay. This means that in the energy range relevant for this work,  $E_\nu \gtrsim 100$  GeV, decay is the dominant production mode of atmospheric neutrinos.

**The energy loss term (4.3c)** is due to energy loss through bremsstrahlung and ionization. As the electromagnetic cascade is ignored, the energy loss does mainly affect the muons of the hadronic shower, that lose energy through ionization. The Bethe-Block formula gives the stopping power  $\mu(E)$ .

**The gain terms (4.3d) and (4.3e)** In the case of zero particle coupling and negligible energy loss, equation (4.3) is a homogeneous linear first-order differential equation where the solution has a simple exponential form. The couplings, either due to inelastic hadronic interactions with air or due to decay, link the evolution of different species  $h$  and thus increase the complexity of the system. The interaction couplings are the differential cross section of particle production, normalized to the total cross section of particle-air interaction.

$$\frac{dN_{k \rightarrow h}(E_k)}{dE} = \frac{1}{\sigma_{inel,k-air}(E_k)} \frac{d\sigma_{k \rightarrow h}(E_k)}{dE}. \quad (4.7)$$

Decays are expressed in a similar way

$$\frac{dN_{k \rightarrow h}^{dec}(E_k)}{dE} = \sum_i \text{BR}_{i,k \rightarrow h} \frac{dN_{i,h}}{dE}, \quad (4.8)$$

$\text{BR}_i$  denotes the branching ratio for a decay channel  $i$ .

Integrating equation (4.3) with respect to the slant depth will yield the energy-dependent flux, and is one method of estimating the flux of particles at the surface of the Earth. In the next section, relevant properties of the atmospheric neutrino flux are presented.

## 4.4 Overview of Neutrino Flux Calculations

**Spectral index of the neutrino flux** The energy dependence of the neutrino flux is determined by the competition between decay and interaction of the parent mesons, as well as the spectrum of cosmic rays. For instance, when  $E_{\nu_\mu} \ll \epsilon_{\pi^+}$ , the muon neutrinos are dominantly produced in the two-body decay of pions and the spectral index of the muon neutrino flux will be that of the pion and hence of the cosmic ray spectrum. This means that at low energies,  $E_\nu \lesssim 100$  GeV, we expect the neutrino flux from meson decay to follow an  $E^{-2.7}$  power law. For  $E_\nu \gg \epsilon_h$ , the neutrinos are primarily a product of particle  $h$  interacting. As the cross section of interaction depends on  $E$ , the neutrino spectrum will be one power steeper, i.e., follow an  $E^{-3.7}$  power law. This is shown in the overall neutrino flux plot in Figure 4.4.

**Pion decay** At low energies, the atmospheric neutrinos come primarily from the two-body decay of charged pions and kaons and the subsequent muon decays. The pion is the lightest meson, consisting of  $u\bar{d}(\pi^+)$ ,  $d\bar{u}(\pi^-)$ , or  $(u\bar{u} - d\bar{d})/\sqrt{2}$  ( $\pi^0$ ), and thus cannot decay through the strong interaction. Hence charged pions must decay weakly to charged leptons. Specifically, the pion decays by  $\pi^\pm \rightarrow \mu^\pm \nu_\mu(\bar{\nu}_\mu)$  with a branching ration of  $\sim 99.98\%$ . This is a manifestation of the chiral structure of the weak interaction: only left-chiral particles and right-chiral antiparticles couple to the weak force.

In a  $\pi^-$  decay, the produced antineutrino must be right-chiral. Since it is effectively massless,  $m_\nu \ll E_\nu$ , the chiral state is equivalent to the helicity state. As the pion has spin 0, the lepton and neutrino in a pion decay must be produced with oppositely directed spins. As the antineutrino is right-handed, conservation

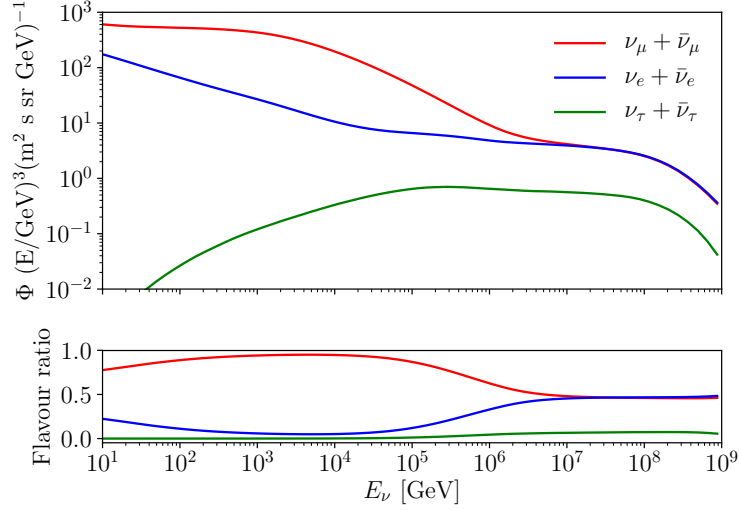
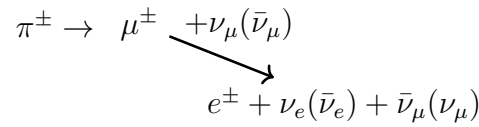


**Figure 4.4.** – The total flux (upper) of electron (blue), muon (red) and tau neutrinos (green) and the flavor ratio (lower) averaged over zenith arrival angles at the surface of the Earth.

of angular momentum implies that the charged lepton is also produced in a right-handed helicity state. Since the weak force does not couple to right-hand particles, the lepton is produced with the «wrong helicity» for weak interaction. The reason why pion decay occurs at all is that helicity is *not* the same as chirality. Because leptons have mass, the weak decay of right-handed *helicity* states can occur. The higher the mass, the more likely will the helicity and chirality differ. Thus the pion decay into the lightest lepton, the electron, is suppressed by a factor of  $10^{-4}$ .

Because of the conservation of lepton numbers, muon decay exclusively to electrons and neutrinos. Thus the pion decay chain is given as



A similar argument can be done for kaons, as charged kaons have a branching ratio of  $\sim 63\%$  into muons and muon neutrinos. The other dominant decay channels consist of charged and neutral pions.

**2:1 flavor ratio** If we assume that all neutrinos are created in pion decay, we should, looking at the decay chain, expect a 2:1 ratio of  $\nu_\mu : \nu_e$ . As can be seen in the lower plot of Figure 4.4, this is indeed the case in the lower energy limit of the relevant energy range,  $E_\nu \lesssim 100$  GeV. However, at higher energy, the atmospheric neutrino flux becomes almost entirely dominated by muon neutrinos.

In its own reference frame, the muon has a mean lifetime of  $\tau_\mu \sim 2.2 \mu\text{s}$ , which corresponds to a path length  $\mathcal{O}(600)$  m. However, the muons created in

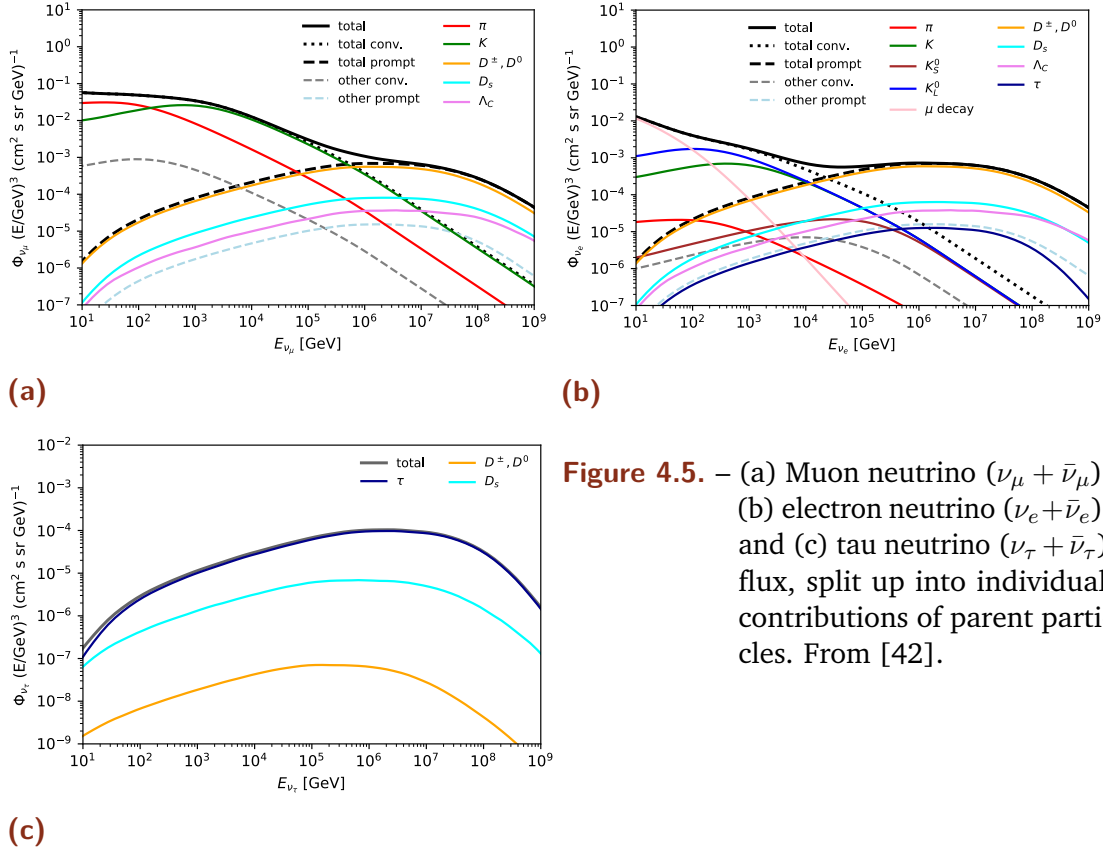


**Figure 4.5.** – (a) Muon neutrino ( $\nu_\mu + \bar{\nu}_\mu$ ), (b) electron neutrino ( $\nu_e + \bar{\nu}_e$ ), and (c) tau neutrino ( $\nu_\tau + \bar{\nu}_\tau$ ) flux, split up into individual contributions of parent particles. From [42].

the atmosphere are highly relativistic, and due to time dilation, they will typically propagate tens of kilometers through the atmosphere before decaying. As the path length depends on the muon energy, high energy muons will be more likely to hit the ground before they have time to decay. A muon hitting the ground will lose energy rapidly and produce only very low energy neutrinos that can be neglected because they are below the threshold of IceCube or any future extensions. As a result, the  $\nu_e$  component of the neutrino flux from muon decay will decrease rapidly with energy.

Based on the pion decay chain, it seems like a feasible approach to estimate the neutrino flux based on the muon flux, which is much easier to measure. However, this is only the case in the energy range where the muons are energetic enough to reach the ground before decay, but before the energy is so high that the kaon contribution to the neutrino flux becomes significant.

**Kaon production dominates at higher energy** Above  $E_\nu \gtrsim 100$  GeV, there will be a small  $\nu_e$  flux of  $< 5\%$  of the total atmospheric neutrino flux. The electron neutrinos are dominantly produced via kaon decay. In general, the ratio of neutrinos produced in kaon decay will increase with energy. This is due to  $\epsilon_K > \epsilon_\pi$ , as seen in Figure 4.3b. Thus the contribution from pion decay will drop off at lower energy than that of kaon decay. The contribution from kaon decay increases with energy and become dominant at  $E_\nu \gtrsim 100$  GeV. This means that in the energy range relevant for this work,  $E_\nu \gtrsim 100$  GeV,  $\nu_\mu$  are dominantly produced in pion decays and  $\nu_e$  are dominantly produced in muon decay.

**Prompt atmospheric flux** The neutrino flux can be divided into a conventional and a prompt component. Prompt atmospheric neutrinos are produced in decays of particles with a critical energy larger than the critical energy of the  $D^\pm$  meson, which is the most long-lived charmed particle. Since  $\epsilon(D^\pm) \sim 5 \times 10^7$  GeV, the prompt decay becomes dominant only at very high energies. Neutrinos from charmed decay follow the spectral index of the cosmic ray flux,  $\sim E^{-2.7}$ .

The notions presented above is summarized in Figure 4.5, showing the production modes of muon neutrinos (4.5a), electron neutrinos (4.5b), and tau neutrinos (4.5c) as a function of neutrino energy. It illustrates how the prompt flux becomes dominant at higher energy, due to the smaller spectral index.

**Atmospheric tau neutrinos** A tau neutrino is produced in association with the heavy tau lepton ( $m_\tau \sim 1.7$  GeV). As the mass of the tau lepton exceeds that of the pion and kaon, tau neutrinos cannot be created by light mesons. The first available production mode is the decay of charmed mesons. This entails that the  $\nu_\tau$  flux only has a prompt component. As seen in Figure 4.5c and Figure 4.4, the contribution of tau neutrinos is negligible below 100 GeV. For this reason, the tau neutrino component of the neutrino flux is ignored throughout this thesis, and most results are shown only for the muon and electron neutrino component of the atmospheric neutrino flux.

## 4.5 The Geomagnetic Field and the Azimuth Dependence of the Neutrino Flux

The geomagnetic field affects both particles inside and outside the atmosphere. Cosmic rays are subject to a rigidity cut-off, i.e. the geomagnetic field is filtering out cosmic rays of low energy per unit charge. Since the geomagnetic field is more complex than a simple, symmetric dipole, the rigidity cut-off is strongly dependent on geographical location and direction, and must generally be calculated with backtracing techniques [46]. This affects mostly cosmic ray particles up to about 20 GeV.

The rigidity cut-off causes an asymmetry in the azimuthal arrival direction of cosmic rays. Cosmic rays, being mostly protons, are generally positively charged, and are thus deflected by the vertical component of the geomagnetic field. If the cosmic ray is arriving from the North or South, its directionality is parallel with the field lines of the geomagnetic field, and no deflection occurs. However, if the cosmic ray is arriving from the East, its trajectory will be bent upwards, away from any potential surface detectors. Correspondingly, the flux of cosmic rays from the West will be enhanced, as a higher portion of the primaries is bent towards the surface of the Earth.

The geomagnetic field also causes an asymmetry by muon bending. The field will affect positively charged muons in the same manner as cosmic rays, causing a reduced  $\bar{\nu}_\mu$  and  $\nu_e$ , the decay products of  $\mu^+$ , flux from the East. Negatively charged muons will bend in the opposite direction resulting in an enhanced  $\bar{\nu}_e$  and  $\nu_\mu$  from the East, and suppression from the West. However, the effect of enhancing the  $\mu^-$  flux from the East, is working in the opposite direction as that

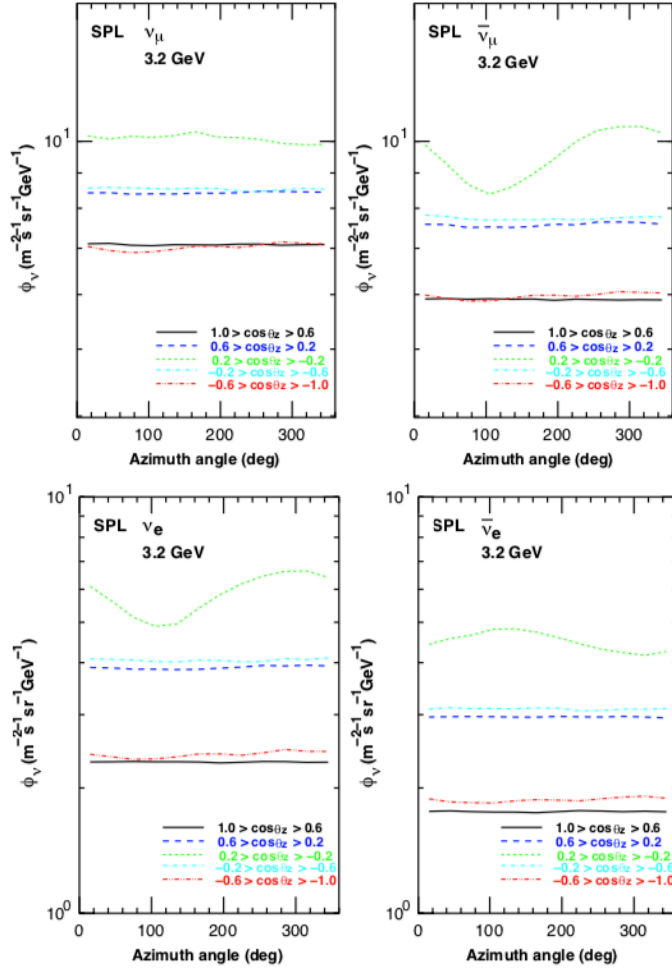


**Figure 4.6.** – Azimuth dependence of the flux of neutrinos with  $E_\nu = 3.2$  GeV in 5 zenith angle bins at the South Pole. The angle is measured counter clockwise from the meridian degree of  $180^\circ$  longitude. From [48].

of the rigidity cut-off, so the azimuthal dependency will assume a much more complicated form (upper left and lower right plot of Figure 4.6) than when the muon bending and rigidity cut-off is working in the same direction (upper right and lower left plot of Figure 4.6), as it is with  $\bar{\nu}_\mu$  and  $\nu_e$ .

The azimuthal asymmetry at the South Pole is small, as the geomagnetic field is almost vertical, with only a small horizontal component that increases at small zenith angles. Thus muon bending and rigidity cut-off will only affect particles coming from the horizon. As seen in Figure 4.6, there is only an azimuthal dependency on events from the horizon, i.e. with a zenith angle  $0.2 < \cos(\theta_z) < -0.2$  (green curves). Honda et al. found that the effect of the geomagnetic field is negligible for  $E_\nu \gtrsim 10$  GeV. Thus the azimuthal dependency of Figure 4.6, which is plotted for the flux of neutrinos with  $E_\nu = 3.2$  GeV, is exaggerated compared to the relevant energies of DeepCore.

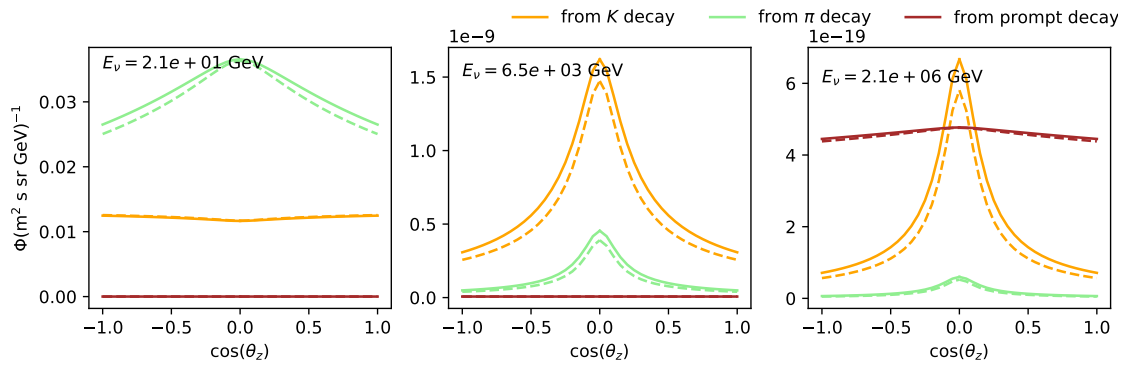


**Figure 4.7.** – The zenith dependence of the muon neutrino flux at three different neutrino energies. The full line is the summer flux, and the dashed line the winter flux. Plot generated using MCEq [1].

## 4.6 The Atmospheric Density and Zenith Dependence of the Neutrino Flux

The path length of a muon from the horizon is much larger (up to 500 km) than when coming from above (about 20 km). Thus a larger fraction of muons from above will hit the surface before decaying, resulting in a lower neutrino flux from above. This zenith dependence is energy-dependent. Figure 4.7 is showing the flux of muon neutrinos at three energies, as a function of zenith angle. In the energy range where kaons and pions decaying to muons are the primary production mode of atmospheric muon neutrinos, the flux is enhanced from the horizon,  $\cos \theta_z = 0$ .

The flux of atmospheric neutrinos created in particle interaction will also be enhanced from the horizon. This is because the particles of the shower will have more potential targets when coming from the horizon than from above. The prompt component of the flux is almost independent of the zenith angle (right plot Figure 4.7), as charmed mesons have negligible decay lengths.

Both the decay length of equation (4.5) and the integrand of the cascade equation – the slant depth of equation (4.2) – depend on the density of the atmosphere,  $\rho_{\text{air}}$ . The most simplistic model of the atmospheric density is the *isothermal* model, which assumes the pressure to decrease exponentially with height and the temperature to be constant. However, the atmosphere contains layers and is subject to daily and seasonal variations. An often-used approach, first proposed by Linsey [49], is to model the atmosphere as five piecewise exponential functions to account for the layers. An even higher degree of complexity can be achieved with tabulated atmospheric data or numerical models, like NRLMSISE-00[50].

The atmospheric conditions also cause a seasonal variation in the flux. In the summer, the density of the atmosphere will be increased at higher altitudes, meaning that the air showers on average will be initiated at higher altitudes. Thus the flux of atmospheric neutrinos will be increased during the summer. In Figure 4.8 (upper), a 10% increase in the neutrino flux in the summer (December-

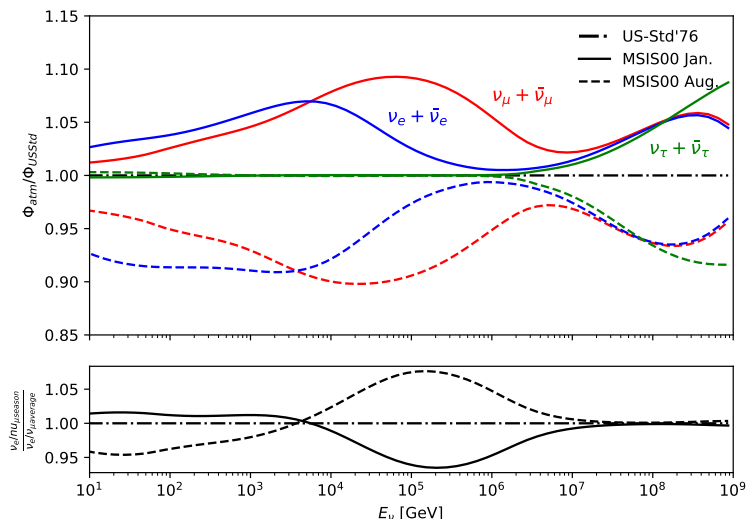


**Figure 4.8.** – Seasonal variations of the atmospheric neutrino flux, generated using MCEq [1]. The upper plot is showing an increase in summer (Jan. at the South Pole) of the flux in all flavours, as compared to a yearly average. The flavour ratio also varies seasonally. Lower plot is showing  $\frac{\nu_e + \bar{\nu}_e}{\nu_\mu + \bar{\nu}_\mu}$  of summer (full line) and winter (dashed line) as compared to a yearly average.

February at the South Pole), when compared to an averaged yearly flux, is shown. In regions where most atmospheric neutrinos are produced through particle interaction, there is no seasonal variation, as the interaction length is independent of the atmospheric density. The decay length of charmed mesons is dependent on the density of the atmosphere, resulting in an increased prompt flux at higher energies in the summer, compared to the winter.

As seen in Figure 4.8 (upper), the air density affects the electron neutrinos at lower energies than the muon neutrino. This causes a seasonal variation in the flavor ratio of the atmospheric flux, plotted in Figure 4.8 (lower). Compared to a yearly average, the flux of low energy  $\nu_e/\bar{\nu}_e$  is lower in winter. This is because the muon is produced lower in the atmosphere during winter, and more often hits the ground before it has time to decay to  $\nu_e/\bar{\nu}_e$ .

An open-source program solving the cascade equation, equation (4.3), is *MCEq*<sup>1</sup> [1]. The solver of *MCEq* integrates over the slant depth to yield the inclusive atmospheric lepton flux. This chapter intends to present an overview of the functionality of *MCEq*, as it is used extensively for the remainder of this work.

## 5.1 Inclusive and Exclusive Neutrino Flux Estimates

Over the last decades, the standard atmospheric neutrino flux estimates have been based on Monte Carlo (MC) techniques. In these schemes, a realistic final state is modeled on a single initial state, by tracking each particle of the air shower. Thus the exclusive lepton flux, meaning the flux per shower, is estimated. This is very much in contrast to analytical solutions, like *MCEq*, that predicts the inclusive lepton flux, meaning the flux generated by an average of air showers.

In general, MC techniques are computationally demanding as they require generation of initial state particles in all directions at all point on Earth. Speed up tricks can be utilized, but the MC methods are still slower to run than analytical methods.

As MC methods propagate each particle of the air shower, the lateral spreading of the shower, both from transverse momentum acquired in the interactions and from bending of charged particles in the geomagnetic field, is generally taken into account. The cascade equation assumes that the direction of the products is adjusted to lie along the trajectory of the primary cosmic ray at the point of the first collision. This allows the calculations to consider only trajectories that point directly at the detector, considerably reducing the computation time. In other words, *MCEq* is a 1D approximation of the problem, whereas MC predictions are generally made in 3D. This entails that the inclusive neutrino flux will have no azimuth dependence. The geomagnetic field is ignored in calculations of inclusive fluxes with the cascade equation. However, the effect of the geomagnetic field is small at the South Pole and for neutrinos with energy  $E_\nu \geq 10$  GeV. Thus this loss of complexity will not affect the current DeepCore oscillation studies [48].

## 5.2 Hadronic Interaction Models

Both inclusive and exclusive calculations of the atmospheric neutrino flux rely on information about the probability of particle interaction, i.e., the cross section between particles of the air shower and the air nuclei. This information has to be generated using Monte Carlo methods.

*Event generators*, also called *hadronic interaction models*, have been developed to describe the final state resulting from a high-energy collision. Among the event generators that are commonly used to simulate air showers, four are updated

<sup>1</sup><https://github.com/afedynitch/MCEq/>

with LHC data at 7 TeV: QGSJETII-03 [51], EPOS LHC [52], SIBYLL2.3c [53], and DPMJETIII 17-1 [54].

MCEq uses SIBYLL2.3c as a default model as it is the latest model that includes all relevant physics for air shower calculations. In particular, the 2.3c version contains a model for the production of charmed hadrons and is therefore capable of predicting the prompt flux. The hadronic interaction models included in the current version of MCEq are listed in Appendix B.

Most event generators are focused on high-energy collisions. At high energy the QCD coupling constant is small, and perturbation theory can be used to calculate the cross sections. In the hadron collisions of an air shower, it is the particles that are emitted in the forward direction, i.e., approximately parallel to the collision axis, that is most relevant for the neutrino flux. The forward collisions are characterized by a small momentum transfer,  $Q$ , between the colliding hadrons. At these low energy scales, the QCD coupling constant is large,  $\alpha_s \sim \mathcal{O}(1)$ , and thus the collision cannot be described with perturbation theory<sup>2</sup>. Thus, there is a lower limit in collision energy,  $\sqrt{s}$ , on the usage of event generators based on perturbative QCD.

Some event generators, like SIBYLL2.3c, have a higher low energy limit than others. To account for this MCEq allows for linear interpolation between a low energy and a high energy interaction model. The user sets the threshold. The initial version of MCEq supports only DPMJET-III as a low energy model. DPMJET-III have a lower limit at  $\sqrt{s} = 10\text{-}20$  GeV [54], which causes an overall limit to the reliability of MCEq predictions.

## 5.3 Limits of MCEq

The developer has put a lower limit on the operation of MCEq at  $E_\nu \sim 10$  GeV. This is because MCEq (1) does not take the geomagnetic field, which becomes relevant below  $E_\nu \sim 10$  GeV, into account, (2) utilize a set of hadronic interaction models that have a lower energy limit above  $\sqrt{s} \sim 10$  GeV.

As the geomagnetic field is not taken into account, there is no difference except for the seasonal variation in atmospheric density between the up- and downgoing neutrino flux. Thus, within MCEq atmospheric neutrinos can be generated with a zenith arrival direction of  $0 < \cos \theta_z < 1$ .

---

<sup>2</sup>In the language of Feynman: An infinite number of Feynman diagrams can result in the same final state. In higher-order-diagrams, more propagators are added, each introducing a vertex that depends on the coupling constant. If the value of the coupling constant is small, the contribution to the cross-section is negligible, and the reaction can be approximated as only the lower-order-diagram(s). At low energies, the coupling constant is large, and an infinite number of diagrams contribute to the matrix element – thus it cannot be calculated analytically.

## 5.4 The Matrix Cascade Equation

The computing scheme of MCEq involves rewriting the cascade equation of (4.3) into matrix form. This entails that the final solution of the matrix cascade equation is a vector of the form

$$\vec{\Phi} = [\vec{\Phi}^p \ \vec{\Phi}^n \ \vec{\Phi}^{\pi^x} \ \dots \ \vec{\Phi}^{\nu_{\bar{\mu}}} \ \dots]^T, \quad (5.1)$$

where each of the inserted vectors contains the scalar fluxes for each energy bin. For instance

$$\vec{\Phi}^p = [\vec{\Phi}_{E_0}^p \ \vec{\Phi}_{E_1}^p \ \dots \ \vec{\Phi}_{E_N}^p]^T. \quad (5.2)$$

The energy bin is defined on a logarithmic grid,  $E_i = E_0 \cdot 10^{di}$ , where  $E_0 = 1$  GeV and  $d$  is chosen accordingly for  $\sim 8$  bins per decade of energy [1]. Thus, the flux vector has dimension  $d_{\Phi} = (\text{number of energy bins}) \times (\text{number of particle species}) \approx 8000$  [1]. When neglecting the energy loss term, and making the transition  $dE \rightarrow \Delta E$ , the cascade equation for one energy bin,  $E_i$ , and one particle species  $h$  becomes

$$\frac{d\Phi_{E_i}^h}{dX} = - \frac{\Phi_{E_i}^h}{\lambda_{int,E_i}^h} \quad (5.3a)$$

$$- \frac{\Phi_{E_i}^h}{\lambda_{dec,E_i}^h(X)} \quad (5.3b)$$

$$+ \sum_{E_k \geq E_i}^{E_N} \sum_k \frac{c_{k(E_k) \rightarrow h(E_i)}}{\lambda_{int,E_k}^k} \Phi_{E_k}^k \quad (5.3c)$$

$$+ \sum_{E_k \geq E_i}^{E_N} \sum_k \frac{d_{k(E_k) \rightarrow h(E_i)}}{\lambda_{dec,E_k}^k(X)} \Phi_{E_k}^k. \quad (5.3d)$$

By comparing equation (4.3) and equation (5.3) we find that the interaction coefficients  $c$  are defined as

$$c_{k(E_k) \rightarrow h(E_h)} = \Delta E_k \frac{dN_{k \rightarrow h}(E_k)}{dE_h} = \Delta E_k \frac{1}{\sigma_{inel,k-air}(E_k)} \frac{d\sigma_{k \rightarrow h}(E_k)}{dE_h}. \quad (5.4)$$

The decay coefficients  $d$  are defined as

$$d_{k(E_k) \rightarrow h(E_h)} = \Delta E_k \frac{dN_{k \rightarrow h}^{dec}(E_k)}{dE_h}(E_h) = \Delta E_k \sum_i \text{BR}_{i,k \rightarrow h} \frac{dN_{i,h}}{dE_h}, \quad (5.5)$$

where  $\text{BR}_i$  denotes the branching ratio of a decay channel  $i$ .

We want to express the terms of the cascade equation as matrices. The numerator of the first and third term of equation (5.3),  $\lambda_{int}$ , can be arranged in a diagonal matrix sorted with the same order of particle species as the flux matrix (5.1).

$$\Lambda_{int} = diag\left(\frac{1}{\lambda_{int,E_0}^p}, \dots, \frac{1}{\lambda_{int,E_N}^p}, \right. \quad (5.6)$$

$$\left. \frac{1}{\lambda_{int,E_0}^n}, \dots, \frac{1}{\lambda_{int,E_N}^n}, \dots\right). \quad (5.7)$$

The decay length is dependent on the slant depth, as well as the energy. If the  $X$  dependence is factorized out,  $\lambda_{dec} = \rho(X)\tilde{\lambda}_{dec}$ , the energy dependence of the decay length can be expressed as a matrix

$$\Lambda_{dec} = diag\left(\frac{1}{\tilde{\lambda}_{dec,E_0}^p}, \dots, \frac{1}{\tilde{\lambda}_{dec,E_N}^p}, \right. \quad (5.8)$$

$$\left. \frac{1}{\tilde{\lambda}_{dec,E_0}^n}, \dots, \frac{1}{\tilde{\lambda}_{dec,E_N}^n}, \dots\right). \quad (5.9)$$

The production of particles of species  $h$  that come from interactions of particles  $k$  can be written as a matrix of interaction coefficients

$$\mathbf{C}_{k \rightarrow h} = \begin{bmatrix} C_{k(E_0) \rightarrow h(E_0)} & \cdots & C_{k(E_N) \rightarrow h(E_0)} \\ & & C_{k(E_N) \rightarrow h(E_1)} \\ & \ddots & \vdots \\ 0 & & C_{k(E_N) \rightarrow h(E_N)} \end{bmatrix}, \quad (5.10)$$

and equivalently in case of decays

$$\mathbf{D}_{k \rightarrow h} = \begin{bmatrix} d_{k(E_0) \rightarrow h(E_0)} & \cdots & d_{k(E_N) \rightarrow h(E_0)} \\ & & d_{k(E_N) \rightarrow h(E_1)} \\ & \ddots & \vdots \\ 0 & & d_{k(E_N) \rightarrow h(E_N)} \end{bmatrix}, \quad (5.11)$$

The full interaction (decay) coupling are assembled in matrix  $\mathbf{C}$  ( $\mathbf{D}$ )

$$\mathbf{C} = \begin{bmatrix} \mathbf{C}_{p \rightarrow p} & \mathbf{C}_{n \rightarrow p} & \mathbf{C}_{\pi^+ \rightarrow p} & \mathbf{C}_{\pi^- \rightarrow p} & \mathbf{C}_{\bar{n} \rightarrow p} & \mathbf{C}_{K^+ \rightarrow p} & \cdots \\ \mathbf{C}_{p \rightarrow n} & \mathbf{C}_{n \rightarrow n} & \mathbf{C}_{\pi^+ \rightarrow n} & \mathbf{C}_{\pi^- \rightarrow n} & \mathbf{C}_{\bar{n} \rightarrow n} & \mathbf{C}_{K^+ \rightarrow n} & \cdots \\ \mathbf{C}_{p \rightarrow \pi^+} & \mathbf{C}_{n \rightarrow \pi^+} & \mathbf{C}_{\pi^+ \rightarrow \pi^+} & \mathbf{C}_{\pi^- \rightarrow \pi^+} & \mathbf{C}_{\bar{n} \rightarrow \pi^+} & \mathbf{C}_{K^+ \rightarrow \pi^+} & \cdots \\ \vdots & \vdots & \vdots & \vdots & \vdots & \vdots & \ddots \end{bmatrix}. \quad (5.12)$$

With this new notation the cascade equation (4.3) becomes the matrix cascade equation

$$\frac{d}{dX} \vec{\Phi} = \left[ (-\mathbf{1} + \mathbf{C})\Lambda_{int} + \frac{1}{\rho(X)}(-\mathbf{1} + \mathbf{D})\Lambda_{dec} \right] \vec{\Phi}. \quad (5.13)$$

## 5.5 The Inputs of MCEq

MCEq requires several numerical tables as inputs: hadron-air cross sections, decay tables, and particle production tables. All tables are generated on the same  $88 \times 88$  energy grid, and one benefit is that new tables/data files can be updated independently of the main MCEq code. The purpose of the next few sections is to go through one-by-one each term of the matrix cascade equation (5.13), each of them corresponding to an input matrix.

MCEq supports  $\sim 60$  hadron species. A *compact* mode is recommended, where only a few species most relevant to the air shower development are retained as explicit species. Other particles are included implicitly so that they do not appear in the output but are accounted for in the solution. Rather than transporting the species, for instance, the  $\Sigma^-$  baryon, only the decay products, like  $n + \pi^-$ , are propagated.

### 5.5.1 Hadron-air cross section

The first and second term of the discretized cascade equation (5.3), depends on the interaction length  $\lambda_{int}$ , contained within  $\Lambda_{int}$ . The interaction length is dependent on the hadron-air cross section, by equation (4.4).

In Figure 4.3a, I have plotted the hadron-air cross section as calculated by two hadronic interaction models: DPMJET-III (dashed) and SIBYLL2.3c (full). In SIBYLL2.3c, particles with unknown inelastic cross sections are approximated by the proton-air cross section, for light mesons by the  $\pi^+$ -air cross section, and for heavier mesons by the  $K^+$ -air cross section, so all baryons follow the same three curves at higher energies. DPMJET-III can calculate the cross section between air and several additional hadrons relevant at collision energies below 1 TeV, without the approximations into baryons, light, and heavy mesons. This illustrates why interpolation is needed between a low energy and a high energy regime when using SIBYLL2.3c.

### 5.5.2 Decay Length

The elements of  $\Lambda_{dec}$  are calculated using equation (4.5). The properties  $\tau_h$  and  $m_h$  for each species  $h$  is included in the ParticleDataTool package<sup>3</sup>. Using these properties, I have plotted the decay lengths as a function of energy in Figure 4.3b.

### 5.5.3 Reinterctions in the Air Shower

The  $\mathbf{C}$ -matrix of the matrix cascade equation (5.13), has dimension  $d_{\mathbf{C}} = (\text{number of particle species}) \times (\text{number of particle species}) \approx 60 \times 60$ . Each element of the  $\mathbf{C}$ -matrix is itself a matrix with dimension  $d_{\mathbf{C}_{k \rightarrow h}} = (\text{energy grid}) \times (\text{energy grid}) = 88 \times 88$ . The elements of the  $\mathbf{C}_{k \rightarrow h}$ -matrix are interaction coefficients, that correspond to the production of particles of type  $h$  with energy  $E_h$ .

The differential cross sections are generated with a hadronic interaction model. Figure 5.1a shows a  $\mathbf{C}_{k \rightarrow h}$ -matrix generated with SIBYLL2.3c, where

<sup>3</sup><https://github.com/afedynitch/ParticleDataTool>

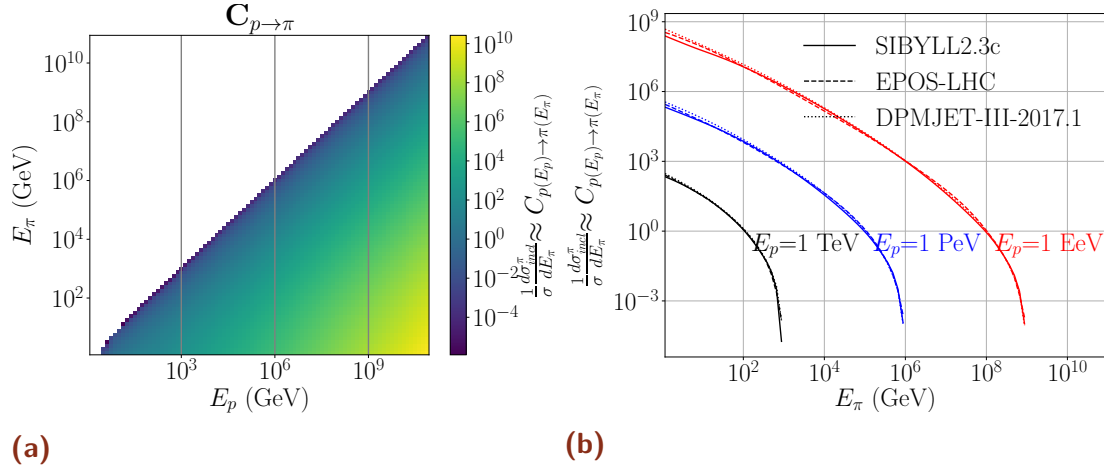


**Figure 5.1.** – (a) Particle production table for  $p \rightarrow \pi^+$  generated in SIBYLL2.3c. The grey lines indicate the energies plotted in Figure 5.1b. (b) Inclusive  $\pi^+$  cross sections for different projectile proton energies  $E_p$ . Apart from the bin factor  $\Delta E$  this is the direct illustration for the content of matrix  $C_{k \rightarrow h}$  for slices of  $E_k$ .

$h = p$  and  $k = \pi^+$ . The distribution is inclusive, integrated over final states, meaning that all states where a  $p(E_p)$  collision produces a  $\pi(E_\pi)$  is included in one element. The x- and y-axis show the common energy grid, the z-axis is the interaction coefficient. This is one of the  $\sim 3600$  matrices filling up the  $\mathbf{C}$ -matrix. As SIBYLL2.3c is the hadronic interaction model that includes the most species, the  $\mathbf{C}$ -matrix generated with SIBYLL2.3c will have the most non-zero sub-matrices. The  $\mathbf{C}$ - and  $\mathbf{D}$ -matrix rarely have more than 3% non-zero elements [1]. The matrix of Figure 5.1a is triangular because of energy conservation:  $E_{\text{projectile}} > E_{\text{secondary}}$ .

Taking three the specific energies marked with gray on Figure 5.1a, the particle production estimated by two more models are compared in Figure 5.1b.

Similar distributions are generated for decay using PYTHIA. The energy distributions of «daughter» particles are generated on the same common energy grid, but instead of varying the energy of the parent particle, the final state is boosted into different frames[1]. PYTHIA is chosen because it contains a database for most of the known branching ratios down to  $10^{-8}$ , whereas other event generators include less decay channels[1].

### 5.5.4 Energy Loss

In the matrix form of the cascade equation (5.13) the energy loss was neglected. The energy loss affects the fraction of neutrinos of  $E_\nu \lesssim 100$  GeV which originates from muon decay. In MCEq the energy loss is included during integration. After one integration step  $\Delta X$  each particle has lost a fraction of its energy  $\hat{E}_i = E_i - \Delta X \langle \frac{dE}{dX}(E_i) \rangle$ , where  $\frac{dE}{dX}$  is defined by the Bethe-Block formula. One can thus obtain a distribution after energy loss,  $\Phi_\mu(E_i, X + \Delta X)$ . It is found that it is sufficient to calculate the energy losses every  $5 \text{ g/cm}^2$ . This is further described in [1].

## 5.6 The Physical Models of MCEq

In addition to the models of decay and hadronic interaction already discussed, cosmic ray models and the model of atmospheric density are also implemented in MCEq. MCEq allows for the use of arbitrary combinations of current state-of-the-art models.

**Density profile of the atmosphere** As discussed in Section 4.6, the atmosphere is most easily modelled by an isothermal model. More complex models like CORSIKA [49] and NRLMSISE-00 [50] are also implemented in MCEq. These models contain information on seasonal variations. The models currently implemented in MCEq are listed in Appendix B.

**Cosmic ray flux** The flux of cosmic rays at the top of the atmosphere is the initial value for the inclusive flux calculations. Except for the GSF model, cosmic ray models are generally parameterizations of the measured cosmic ray spectrum. This is further reviewed in Appendix B.

**Prompt Production** Prompt production, where a charmed meson promptly decays to a neutrino, occurs above the TeV-range and is thus not relevant for this work. However, it should be briefly mentioned that SIBYLL2.3c can simulate the prompt neutrino flux [55]. In MCEq it is also possible to inject custom models of charmed hadron production, by implementing a custom class.

# PYTHIA/Angantyr as an Interaction Model in Atmospheric Flux Calculations

PYTHIA is a much-used event generator among LHC experimentalists and is well tested for proton-proton (pp) collisions. PYTHIA assumes perturbative QCD, and this assumption is only valid at center-of-mass energies larger than  $\sqrt{s} \gtrsim 10$  GeV. PYTHIA developers have set an upper limit at  $\sqrt{s} \lesssim 100$  TeV [56].

Unlike the many pp collisions generated at the LHC, collisions of cosmic ray initiated air showers are not pp, but rather collisions between protons and air molecules (pA). In recent years, work has been done on extending PYTHIA to describe heavy ion (pA and AA) collisions: the Angantyr model [57]. This event generator could thus be a convenient choice of hadronic interaction model for atmospheric neutrino flux calculations.

In order to use PYTHIA/Angantyr in air shower calculations, the following must be added:

1. PYTHIA/Angantyr does not include kaon projectiles. As kaons are an abundant particle species in an air shower, the kaon-proton cross section must be added to the model.
2. Oxygen and nitrogen targets must be included.

In the following chapter, kaons and pions are assumed to be charged.

## 6.1 Deriving the Cross Section

Consider a  $pO \rightarrow \kappa$  collision,  $\kappa$  being the production yield of a particle of a specific type. As the proton collides with the oxygen atom, it can interact with one or more of the  $\sim 16$  nucleons of the nucleus. A simplification would be to model each of these nucleon-nucleon collisions as a pp collision and add the production yield from each sub-collision together to find a final production yield,  $\kappa$ , from the  $pO$  collision. With this approach, PYTHIA can be used to model each pp collision, a process further described in [56]. The problem that then needs to be solved is: how many nucleon-nucleon sub-collisions can we expect? The participants of nucleon-nucleon sub-collisions that contribute to the final particle production yield are called «wounded» nucleons. The question will be answered in the following steps <sup>1</sup>:

1. Find the position of each nucleon within the nucleus
2. Find the nucleon-nucleon cross section

<sup>1</sup>This presentation of the Angantyr model follows closely that of Bierlich, Gustafson, Lönnblad, and Shah [57].

3. Find the number of wounded nucleons
4. Show how we can determine the number of wounded nucleons by providing a kaon-proton cross section

**Nucleon positions** The potential of the nucleus is assumed to follow a Woods-Saxon potential as a function of the nucleus radius. Using Monte Carlo techniques, one can sample randomly from the distribution, yielding nucleon positions within the nucleus.

**Cross sections** The probability amplitude of nucleon-nucleon sub-collisions is  $A$ , where  $A_{\text{el}}$  and  $A_{\text{abs}}$  are the probability amplitude of elastic and inelastic scattering respectively. In general, it is more convenient to express scattering in *impact parameter (b) space*. Given that the total probability of nucleon-nucleon scattering is  $P_{\text{tot}} = P_{\text{el}} + P_{\text{abs}}$ , where  $P_{\text{el}} = |A_{\text{el}}(\mathbf{b})|^2$  and the sum of the amplitude of all inelastic channels  $j$  is  $\sum_j |A_j(\mathbf{b})|^2 = P_{\text{abs}}$ , the normalized optical theorem will give

$$\text{Im } A_{\text{el}}(\mathbf{b}) = \frac{1}{2} \left( |A_{\text{el}}(\mathbf{b})|^2 + \sum_j |A_j(\mathbf{b})|^2 \right). \quad (6.1)$$

In high energy collisions the real part of the elastic amplitude is small, and can be neglected so  $A_{\text{el}}(\mathbf{b}) \sim \text{Im } A_{\text{el}}(\mathbf{b})$ . Substituting this into equation (6.1) we find

$$A_{\text{el}}(\mathbf{b}) = i \left( 1 - \sqrt{1 - P_{\text{abs}}(\mathbf{b})} \right). \quad (6.2)$$

We assume that the projectile nucleon(s) in the projectile nucleus travel on a straight line through the target, as the nucleon(s) carry enough energy to be essentially undeflected by the target nucleons. This approximation entails that the probability of the projectile being absorbed in the nucleus at a fixed  $\mathbf{b}$ , is the sum of the probability of absorption with each individual nucleon:  $P_{\text{abs}} = f_1 + f_2 + \dots + f_n$  (double counting). The double counting terms are inserted to avoid counting the same probability twice. In the case of three nucleons, i.e., a baryon nucleus, we get:

$$P_{\text{abs}} = f_1 + f_2 + f_3 - f_1 f_2 - f_2 f_3 - f_1 f_3 + f_1 f_2 f_3 = 1 - (1 - f_1)(1 - f_2)(1 - f_3). \quad (6.3)$$

If  $f_i$  is small, this approximates to:

$$P_{\text{abs}} \approx 1 - \prod_i \exp(-f_i) = 1 - \exp\left(-\sum_i f_i\right) = 1 - \exp(-2F(\mathbf{b})), \quad (6.4)$$

where  $F(\mathbf{b})$  is introduced as a shorthand. Substituting this into equation (6.2) results in  $A_{\text{el}}(\mathbf{b}) = i(1 - e^{-F(\mathbf{b})})$ .

$$P_{\text{el}} = |A_{\text{el}}(\mathbf{b})|^2 = (1 - e^{-F(\mathbf{b})})^2, \quad (6.5)$$

$$P_{\text{tot}} = P_{\text{el}} + P_{\text{abs}} = (1 - e^{-F(\mathbf{b})})^2 + (1 - e^{-2F(\mathbf{b})}) = 2(1 - e^{-F(\mathbf{b})}). \quad (6.6)$$

We can then define the  $T$ -matrix:  $T(\mathbf{b}) \equiv \text{Im}(A_{\text{el}}(\mathbf{b})) = 1 - e^{-F(\mathbf{b})}$  yielding

$$d\sigma_{\text{el}}/d^2b = T(\mathbf{b})^2 \text{ and } d\sigma_{\text{tot}}/d^2b = 2T(\mathbf{b}). \quad (6.7)$$

$$(6.8)$$

**Diffractive excitation** When deriving the cross sections above, we made the implicit assumption that all inelastic processes are absorptive, i.e., that  $P_{\text{abs}}$  was the sum of the amplitude of all inelastic channels  $j$ ,  $\sum_j |A_j(\mathbf{b})|^2$ . This is not the case. Absorption means that color exchange between the nucleons results in the fragmentation of both. However, the interaction can also result in one of the nucleons being excited to a higher mass state with the same quantum numbers. The excited nucleon will hadronize, while the other remains intact. This process is called *singe diffractive*. If both nucleons are excited to a higher mass state, the interaction is *double diffractive*. These interactions give a significant contribution to the total and elastic cross section and must be accounted for in modeling of nucleon-nucleon collisions [58]. We have:

$$\sigma_{\text{tot}} = \sigma_{\text{el}} + \sigma_{\text{inel}} = \sigma_{\text{el}} + \sigma_{\text{abs}} + \sigma_{DD} + \sigma_{pD} + \sigma_{Dt} \quad (6.9)$$

where subscripts  $Dt$ ,  $pD$  and  $DD$  stand for single diffractive excitation of the target, the projectile, and both.

The diffractive excitations can be accounted for by introducing fluctuations in the nucleon, i.e., that the mass eigenstate of the nucleon  $\Psi_i$  differs from the elastic scattering eigenstate  $\Phi_l$ . In Appendix C it is shown that this assumption results in the following cross sections relevant for nucleon-nucleon collisions

$$d\sigma_{\text{tot}}/d^2b = \langle 2T(\mathbf{b}) \rangle_{proj,t}, \quad (6.10)$$

$$d\sigma_{\text{abs}}/d^2b = \langle 2T(\mathbf{b}) - T^2(\mathbf{b}) \rangle_{proj,t}, \quad (6.11)$$

$$d\sigma_{\text{el}}/d^2b = \langle T(\mathbf{b}) \rangle_{proj,t}^2, \quad (6.12)$$

$$d\sigma_{Dt}/d^2b = \langle \langle T(\mathbf{b}) \rangle_{proj}^2 \rangle_t - \langle T(\mathbf{b}) \rangle_{proj,t}^2, \quad (6.13)$$

$$d\sigma_{pD}/d^2b = \langle \langle T(\mathbf{b}) \rangle_t^2 \rangle_{proj} - \langle T(\mathbf{b}) \rangle_{proj,t}^2, \quad (6.14)$$

$$d\sigma_{DD}/d^2b = \langle T^2(\mathbf{b}) \rangle_{proj,t} - \langle \langle T(\mathbf{b}) \rangle_{proj}^2 \rangle_t - \langle \langle T(\mathbf{b}) \rangle_t^2 \rangle_{proj} + \langle T(\mathbf{b}) \rangle_{proj,t}^2, \quad (6.15)$$

where  $proj$  and  $t$  denotes averages over the projectile and target state, respectively.

**Wounded Nucleons** Though derived in the context of nucleon-nucleon collisions, the results are general and equations (6.10–6.15) might just as well describe a pA or AA collision. As the projectile collides with nucleons in the target, we can assume that the wave function collapses after the first interaction and remains «frozen» in a state  $k$ . This corresponds to averaging over target states. If so

$$\frac{d\sigma_{\text{tot}}}{d^2b} = \langle 2T(\mathbf{b}) \rangle_{proj}. \quad (6.16)$$

However, one is normally not interested in the total number of nucleons interacting in the collision, but rather those that interact in a way that contributes to particle production. We are therefore interested in the  $\sigma_{\text{inel}}$ , rather than  $\sigma_{\text{tot}}$ . When assuming a «frozen» projectile and averaging over target states, the inelastic cross section is modified. The average over targets must be done *before* the squaring of the second term.

$$\frac{d\sigma_w}{d^2b} = \langle 2T(\mathbf{b}) \rangle_{proj,t} - \langle \langle T(\mathbf{b}) \rangle_t^2 \rangle_{proj} \quad (6.17)$$

We then have an expression for the probability of wounding a nucleon in a pA or AA collision, and thus an expression for the number of nucleons contributing to the particle production.

In [57] it is shown that  $T(\mathbf{b})$  can be assumed to follow a certain distribution (Appendix C). By providing values for  $\sigma_{\text{tot}}$ ,  $\sigma_{\text{el}}$ ,  $\sigma_{Dt}$ ,  $\sigma_{pD}$  and  $\sigma_{DD}$  a fit is preformed to  $T(\mathbf{b})$  of equation (6.10–6.15) which determines all variables of describing the nucleon. By determining  $T(\mathbf{b})$  we can also fix the number of nucleons, by equation (6.17), that interact in such a way that they produce particles. After determining the number of sub-collisions, each sub-collision can be modeled as a pp collision. The particle production yield from each sub-collision is then added up to give a final production yield from the pA or AA collision.

## 6.2 Introducing Kaon Projectiles

From the discussion above, it can be concluded that all parameters of the collision are determined if the cross sections of equation (6.10–6.15) are supplied to PYTHIA/Angantyr. Of the collision types relevant for air showers, the pion-proton and proton-proton cross sections are already implemented in PYTHIA/Angantyr, using a model by Schuler and Sjöstrand [59]. The PYTHIA-calculated cross-section for  $\bar{p}(p)p$  (red full line) and  $\pi^-(\pi^+)p$  (blue full line) is shown in Figure 6.1, as a function of center-of-mass energy. The dashed lines in Figure 6.1 are parameterizations of accelerator data by the COMPAS group [60]. Accelerator data sparsely cover the phase space used by the COMPAS fit. For pion-proton collisions there is no data beyond  $\sqrt{s} \sim 30$  GeV, and for proton-proton collisions the accelerator data extends to  $\sqrt{s} \sim 6$  TeV. In the regions of phase space where data exists, the PYTHIA estimated cross section is reproduced by the COMPAS fit. In regions of no data, a disagreement between PYTHIA and COMPAS predictions can be observed.

A projectile relevant for air showers, but not previously included in PYTHIA, is the kaon. It is feasible that the kaon-proton and pion-proton cross section will have similarities, as pions and kaons are mesons with similar structures. On a reductive level, the only difference between them is the increased mass due to the presence of the more massive strange quark in the kaon. As the cross section depends on the inverse of the rest mass, this should result in a lower kaon-proton cross section, than a pion-proton cross section. Indeed the COMPAS fit in Figure 6.1 shows that the parameterizations of the kaon-proton (green) and pion-proton cross section (blue) are similar in shape, but with a relative difference

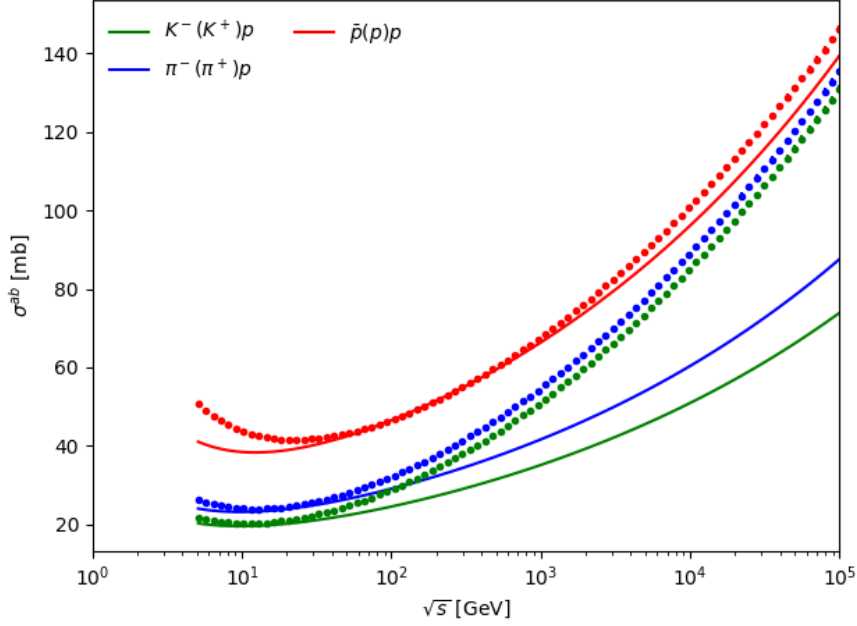


**Figure 6.1.** – Comparison between the COMPAS fit [60] (points) and the PYTHIA hadronic cross sections (full line).

in magnitude. Based on these features, a pragmatic approach can be adopted: The total kaon-proton cross section is equal to that of the total pion-proton cross section, but scaled down with a constant factor,  $a$ .

$$\sigma^{K^\mp p} = a \cdot \sigma^{\pi^\mp p} \quad (6.18)$$

The value of  $a$  is found by comparing to accelerator data from COMPAS made available by the Particle Data Group<sup>2</sup>. The available data is on  $\sigma_{\text{tot}}$  and  $\sigma_{\text{el}}$  up to  $\sqrt{s} \sim 17$  GeV. The data for total (black) and elastic (red)  $K^+p$  cross section is plotted in Figure 6.2. Based on data comparison, the kaon-proton cross section was estimated to 90% of the pion cross section,  $a = 0.9$ . The PYTHIA calculated total (black) and elastic (red)  $K^+p$  cross section are plotted by scaling down the pion-proton cross section with 90%. As PYTHIA is a high energy event generator, the cross sections are plotted for  $\sqrt{s} \geq 5$  GeV. The total and elastic  $K^+p$  cross sections seem to agree reasonably well with data at low energies.

The Schuler and Sjöstrand model includes the diffractive cross sections. These are plotted in Figure 6.2. As shown in Section 6.1, the diffractive cross sections are derived by introducing fluctuations. As the structure of the pion and kaon are similar, there are no apparent reasons why the range of fluctuations should differ. Thus it seems feasible that the diffractive cross sections of kaon-proton are equal to those of pion-proton.

The pragmatic approach of estimating the kaon-proton cross section based on the pion-proton cross section breaks down at higher energies. In higher energy collisions, the sea quarks and gluons of the meson are probed, and thus the

<sup>2</sup>from <http://pdg.lbl.gov/2014/hadronic-xsections/>

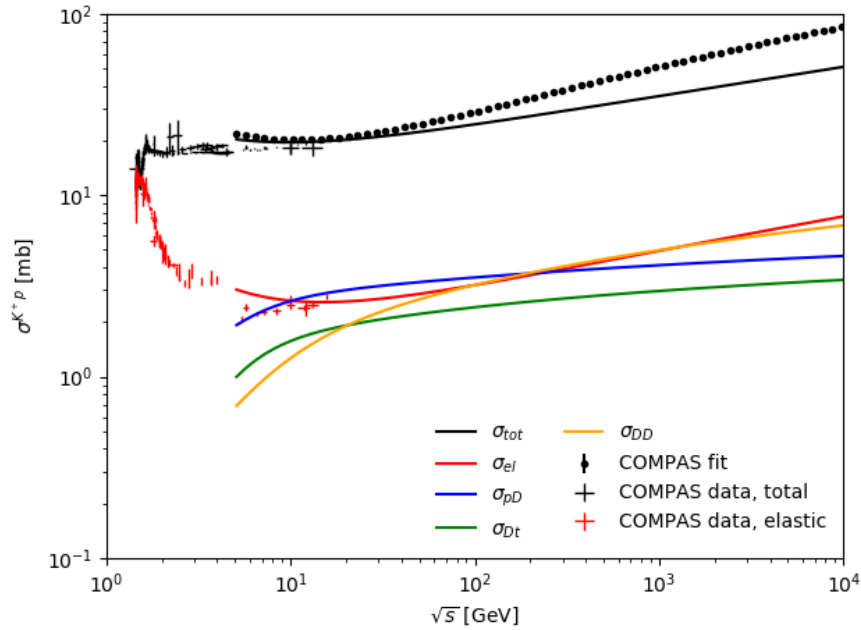


**Figure 6.2.** – Data from the COMPAS Group, made available by the Particle Data Group, of the  $K^+p$  total and elastic cross section, compared to the  $K^+p$  cross section calculated by PYTHIA.

valence quark collisions are sub-dominant. In this case, the mass difference of the valence quarks between the pion and kaon should cease to be of significance, and the cross sections should approach each other. By scaling the kaon-proton cross section to the pion-proton cross section, they will, by design, never approach each other. This expected behavior is not reproduced by the COMPAS fit either.

We could, in principle, have chosen the COMPAS fit to model the kaon-proton total and elastic cross section. However, COMPAS does not fit to data for the single diffractive and double diffractive cross section, which must be included in order to reproduce data. Based on data, it is not possible to establish which, if either, of COMPAS and PYTHIA, are more correct. It thus seems reasonable to choose the model that describes all five cross sections, rather than estimating two with COMPAS and three with PYTHIA.

### 6.3 Comparing the Kaon-proton Cross Section to Data

After supplying PYTHIA with an estimated kaon-proton cross section, PYTHIA generates possible final states in a Monte Carlo process. In this section, I will investigate whether the predicted final states agree with data from the NA22 experiment. A 1988 NA22 paper [61] presents data for the inclusive reactions

$$\pi^+ + p \rightarrow C^+ + \kappa, \quad (6.19)$$

$$\pi^+ + p \rightarrow \pi^- + \kappa, \quad (6.20)$$

$$K^+ + p \rightarrow C^+ + \kappa, \quad (6.21)$$

$$K^+ + p \rightarrow \pi^- + \kappa, \quad (6.22)$$

$$p + p \rightarrow C^+ + \kappa, \quad (6.23)$$

$$p + p \rightarrow \pi^- + \kappa, \quad (6.24)$$

at an incident beam of 250 GeV. Charged particles are denoted as  $C^+$ , and  $p$  denotes a proton. NA22 was a fixed target experiment at the CERN SPS with a bubble chamber as a vertex detector, meaning it had full coverage of the transverse momenta  $p_T$ . More on the experimental set-up can be found in [61].

In order to compare to data, PYTHIA was set up in the same manner as the experiment: A 250 GeV beam of projectiles ( $p$ ,  $\pi^+$ , or  $K^+$ ) onto a fixed target ( $p$ ). Like in the NA22 analysis, all stable, positively charged hadrons are taken into account. A cut on  $p_T < 1.2$  GeV aims to reduce the amount of protons in the  $C^+$  and  $\pi^-$  sample.

In a fixed-target experiment, all quantities are measured in the laboratory frame, *lab*. The data presented in [61] is however in the centre-of-mass frame, *C.M.* Thus it is necessary to transform the distributions in PYTHIA from the laboratory to the center-of-mass frame. The particles from the collision are Lorentz boosted, meaning that the momentum and energy transform as:  $p'_z = \gamma(p_z - \beta E)$  and  $E' = \gamma(E - \beta p_z)$ . In a relativistic system, velocities are not an additive quantity when transforming between frames. However, we can define the *rapidity*

$$y = \frac{1}{2} \ln \left( \frac{E + p_z}{E - p_z} \right), \quad (6.25)$$

where  $E$  is the measured energy and  $p_z$  the z-component of the momentum. Rapidity differences are invariant under boosts along the beam direction because

$$y' = \frac{1}{2} \ln \left( \frac{E' + p'_z}{E' - p'_z} \right) = \frac{1}{2} \ln \left( \frac{\gamma(E - \beta p_z) + \gamma(p_z - \beta E)}{\gamma(E - \beta p_z) - \gamma(p_z - \beta E)} \right) \quad (6.26)$$

$$= \frac{1}{2} \ln \left( \frac{(1 - \beta)(E + p_z)}{(1 + \beta)(E - p_z)} \right) = y + \frac{1}{2} \ln \left( \frac{1 - \beta}{1 + \beta} \right) = y + y_b, \quad (6.27)$$

where  $y_b$  is a constant.

The velocity of the particle is  $\beta = p/E$ , and in the laboratory frame where every component of the momentum is zero, except the z-component of the projectile particle,  $p = p_z$  and  $E = E_{\text{projectile}} + E_{\text{target}} = E_k + E_p = E_k + m_p$ , yielding

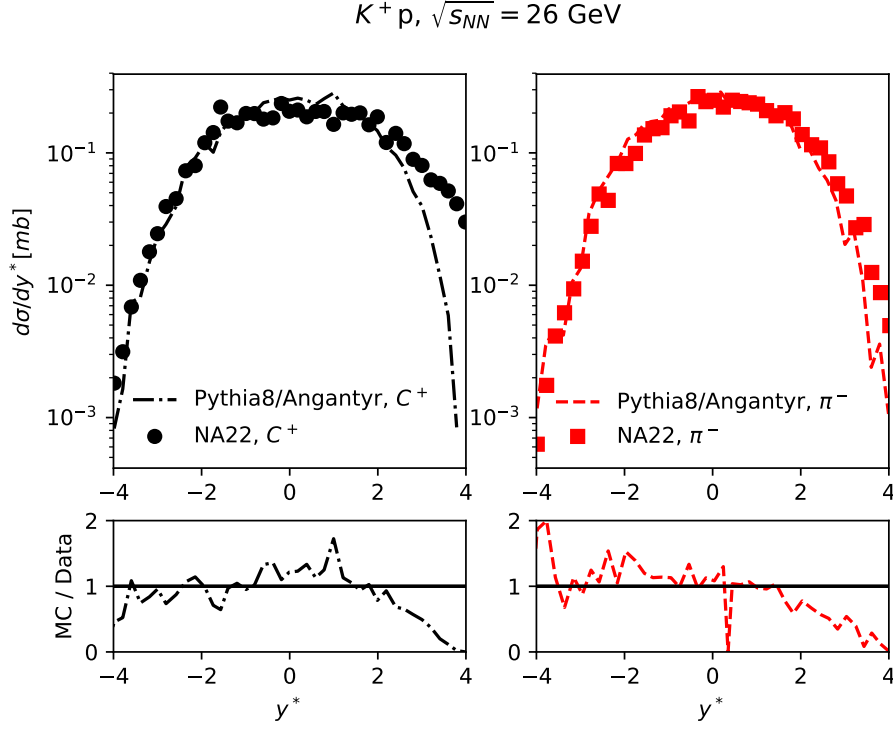


**Figure 6.3.** – Inclusive distributions  $d\sigma/dy^*$ ,  $y^*$  being the rapidity in the centre-of-mass frame, for  $K^+ + p \rightarrow C^+ + X$  (left) and  $K^+ + p \rightarrow \pi^- + X$  (right), compared to distributions obtained in PYTHIA/Agantyr.

$$\beta = \frac{p_z}{E_k + m_p}, \quad (6.28)$$

$$y_b = \frac{1}{2} \ln \left( \frac{E_k + m_p + p_z}{E_k + m_p - p_z} \right). \quad (6.29)$$

where  $E_k = \sqrt{m_k^2 + p_z^2}$  and  $p_z = 250 \text{ GeV}$ . This yields a constant factor of  $y_b \sim 3.13$ . We then have the transformation  $y_{C.M.} = y_{lab} + y_b$ . In Figure 6.3 data for inclusive distributions  $d\sigma/dy^*$ ,  $y^*$  being the rapidity in the centre-of-mass frame, is plotted for  $K^+ + p \rightarrow C^+ + \kappa$  (left) and  $K^+ + p \rightarrow \pi^- + \kappa$  (right). The dashed lines are the corresponding distributions obtained in PYTHIA. The disagreement at high rapidity is most likely caused by the fact that some beam remnants are present in the NA22 data sample, while not modelled in PYTHIA. NA22 present their results normalized to a production cross section that is not quoted in the paper. The results of Figure 6.3 is thus normalized to one.

In order to compare data to additional data from NA22, the rapidity is transformed to the pseudorapidity  $\eta$  by formula

$$\eta = \frac{1}{2} \ln \left( \frac{\sqrt{m_T^2 \cosh^2 y - m^2} + m_T \sinh y}{\sqrt{m_T^2 \cosh^2 y - m^2} - m_T \sinh y} \right), \quad (6.30)$$

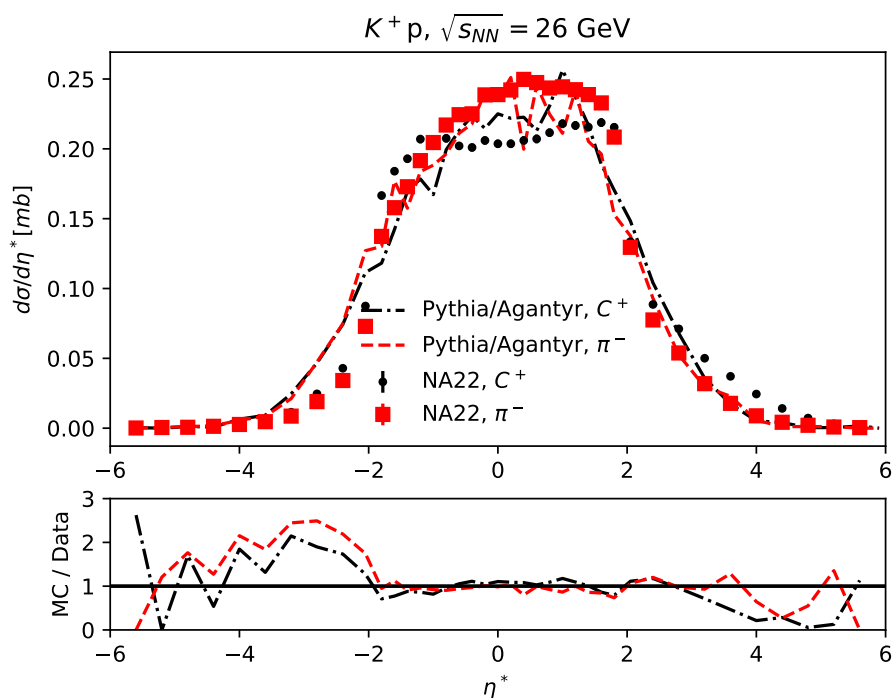


**Figure 6.4.** – The pseudo-rapidity distributions,  $d\sigma/d\eta^*$ , for  $K^+ + p \rightarrow C^+ + X$  (black) and  $K^+ + p \rightarrow \pi^- + X$  (red) compared to distributions from PYTHIA

where the transverse mass  $m_T = m^2 + p_x^2 + p_y^2$ . Thus the fixed target results from PYTHIA are transformed from  $y_{\text{lab}} \rightarrow y_{\text{C.M.}} \rightarrow \eta_{\text{C.M.}}$ . In Figure 6.4 the inclusive distribution of pseudo-rapidity in the centre-of-mass frame is plotted, and data (dots) and PYTHIA generated distributions (lines) compared. Again the distributions are normalized to one.

## 6.4 Kaon-nucleus Collisions

The Angantyr model assumes that a  $K^\pm A$  collision can be modeled as the sum of the final states of all  $K^\pm p$  collisions, provided we have estimated the correct number of wounded nucleons.

Simulating the kaon-nucleus collision requires the following steps: (1) determine the nucleon position within the nucleus by Monte Carlo sampling a distribution, (2) calculate the number of wounded nucleons by the method described in Section 6.1, (3) generate  $K^\pm p$  sub-collision final states (tested on data in Section 6.3), and (4) sum the final states of all  $K^\pm p$  collisions independently. The latter step is tested in this section by comparing to data.

Within the Angantyr model, any ion can be introduced, by defining spin, charge, color, and mass in a decay table. Particular types of ions will differ by the width of the sampling distribution and range of fluctuations. However, the method of determining the number of wounded nucleons is entirely independent of target type, meaning that if the model is capable of determining the number of nucleon-

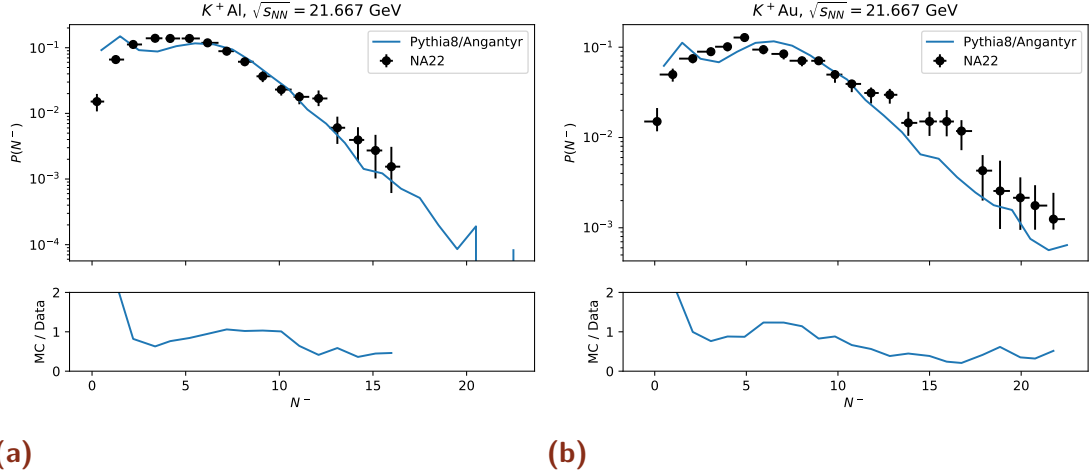


**Figure 6.5.** – (a) Multiplicity of negatively charged hadrons  $N^-$  produced in kaon-aluminum collisions. Data from [62]. (b) Multiplicity of negatively charged hadrons  $N^-$  produced in kaon-gold collisions. Data from [62].

nucleon sub-collisions for one target element, the results should generalize to all elements. Thus we can test our kaon-atom model on any target type.

This is convenient as there is no available data on kaon-oxygen or kaon-nitrogen collisions, which are more relevant for air shower simulations. There exists data for  $K^+$  on gold (Au) and aluminum (Al) nuclei at 250 GeV [62]. PYTHIA was initialized in a setup similar to that of [62], introducing gold and aluminum targets. The resulting multiplicity for stable negatively charged particles were obtained, and the distributions compared to data in Figure 6.5a and Figure 6.5b.

## 6.5 Implementation in MCEq and Outlook

Within the Angantyr model  $p(N/O) \rightarrow \kappa$  collisions,  $\kappa$  being the particle production yield and  $N/O$  being a nitrogen or oxygen atom, were implemented prior to work presented in this chapter. In Figure 6.6a the production yield of  $\kappa = \pi^+$  is plotted and compared to the SIBYLL2.3c model predictions, for projectile protons of energy 1 TeV (black), 100 TeV (blue), and 1 PeV (red). As part of this work, the possibility of kaon projectiles was implemented, meaning the addition of  $K^\pm(N/O) \rightarrow \kappa$  collisions to PYTHIA/Angantyr. In Figure 6.6b this extension is shown for projectile kaons of energy 1 TeV (black), 100 TeV (blue), and 1 PeV (red).

In order to use the developed framework within MCEq, production yield tables (C-matrices) must be generated using PYTHIA. This entails repeating the exercise indicated in Figure 6.6a and 6.6b for projectile energies on a logarithmic grid, defined as  $E_i = E_0 \cdot 10^{di}$ , where  $E_0 = 1$  GeV and  $d$  is chosen accordingly for  $\sim 8$  bins per decade of energy. A continuation of the work presented in the chapter would be to generate these tables and compare the neutrino flux predictions using PYTHIA as a hadronic interaction model to other, already MCEq-implemented hadronic interaction models.

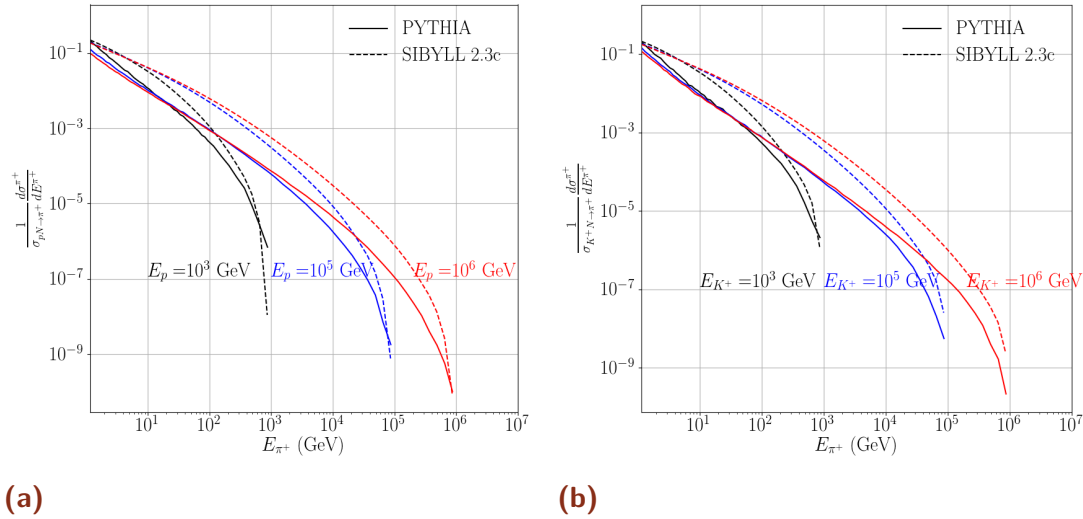


**Figure 6.6.** – (a) Inclusive cross section of  $pN \rightarrow \pi^+$ , (b) Inclusive cross section of  $K^+N \rightarrow \pi^+$ , plotted for different projectile energies: 1 TeV (black), 100 TeV (blue), and 1 PeV (red). The distributions are normalized to the production cross section.

Though physically motivated, scaling the  $\pi^\pm p$  cross section to estimate the  $K^\pm p$  cross section is a somewhat crude approach. An improvement would be to use a kaon-proton cross section calculated using designated software. Besides this, further development of the suggested scheme will require more experimental data, such as measurements of the cross section at higher center-of-mass energy, measurement of the diffractive cross sections and measurements of the kaon parton distribution function (PDF).

All models that are used as an input in MCEq have an associated uncertainty. In *Uncertainties in Atmospheric Neutrino Fluxes*, G.D. Barr, S. Robbins, T.K. Gaisser and T. Stanev[63] review the sources of uncertainty in atmospheric neutrino flux estimates. They find that the dominant source of uncertainty stems from hadronic interaction, and following this, the flux of cosmic rays. Thus the uncertainty on the atmospheric density profile, the muon energy loss, and the model of the geomagnetic field is sub-dominant for the atmospheric neutrino flux uncertainty in the relevant energy range for IceCube/DeepCore.

In previous chapters, methods of estimating the absolute atmospheric neutrino flux have been presented. The topic of this chapter is the uncertainty on that estimate. Following the conclusions of Barr et al., the focus will be on uncertainties stemming from hadronic interactions and the flux of cosmic rays.

## 7.1 Uncertainties on the Particle Production

In the atmosphere, most neutrinos with energy below 100 GeV are produced from the decay of mesons, themselves being products of  $pA \rightarrow (\pi/K)^\pm \kappa$  interactions. The projectile is labeled  $p$ , the target nucleus  $A$ , and the meson of interest  $(\pi/K)^\pm$ . The rest of the interaction products are represented as  $\kappa$ . As seen in chapter 6, a  $pA$  collision is a complex system, and there can be multiple parton collisions, either absorptive, diffractive, or elastic. The uncertainty on the cross section of  $pA \rightarrow (\pi/K)^\pm \kappa$  is therefore substantial, though difficult to estimate.

An uncertainty on the cross section corresponds to an uncertainty on the particle production yield. The effect on the absolute neutrino flux is reasonably straightforward: underestimating the production of hadrons that contribute to the neutrino production by 10% results in a 10% underestimation of the atmospheric neutrino flux [63].

As different physical effects are relevant at different collision energies, the uncertainty on particle production will, in general, be energy-dependent. Because the neutrinos produced in meson decay are of lower energy than the meson itself, the uncertainty on meson production will affect a different region of the neutrino phase space than the meson phase space. This is demonstrated in Figure 7.1, showing the absolute flux of muon and electron neutrinos. In the left plot, a 30% increase in the number of produced  $K^+$  with energy larger than 3 GeV has been introduced. This results in an increase of the neutrino fluxes (dashed lines) – but also for neutrinos with energy less than 3 GeV.

### 7.1.1 Comparing Hadronic Interaction Models

A naive way of assigning an uncertainty on the particle production is by comparing the predictions of different hadronic interaction models. In general, there are several reasons why estimating an uncertainty based on the spread of physical models is problematic: (1) the divergence between the mean of the model predictions does not necessarily yield any information on the variance

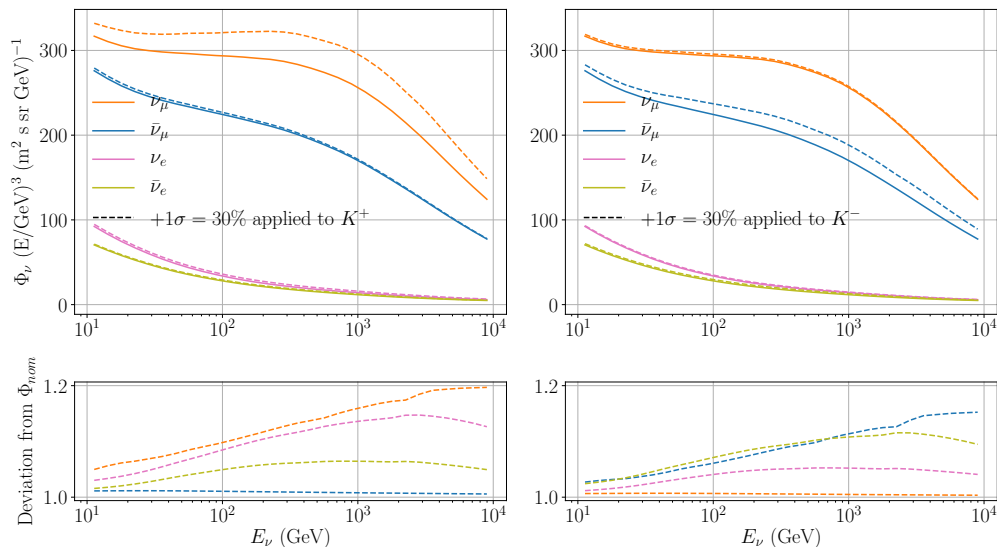


**Figure 7.1.** – Nominal fluxes of muon (anti)neutrinos (blue and orange respectively) and electron (anti)neutrinos (green and pink respectively) calculated with MCEq and averaged over zenith angles. A 30% uncertainty in the particle production yield of  $K^+$  ( $K^-$ ) with  $E_K > 3$  GeV is introduced, and the effect on the neutrino flux is plotted with dashed lines on the left (right) plot.

on each model prediction, and (2) models might be tuned to the same data or each other at an early stage, meaning that the model predictions are correlated. For these reasons, it is more methodically sound to estimate the uncertainty based on data, rather than model comparison. In the following section, a method proposed by Barr et al. of estimating the uncertainty on particle production based on accelerator data is presented.

### 7.1.2 The Barr Scheme

The atmospheric neutrino flux spans a large region of parameter space, sparsely populated by measurements from accelerators. Figure 7.2 summarizes the measurements as of 2006 in a region of phase space relevant for DeepCore[63]. The energy of the projectile,  $E_i$ , ranges between 1 GeV and 1 TeV, whereas the produced meson can assume energies,  $E_s$ , in the range between 0.1 GeV and 1 TeV. The bands for each experiment represent the range in which data exist for at least one value of transverse momentum,  $p_T$ .

In regions of phase space where data exist, the uncertainty on the particle production can be assumed to be equivalent to that reported by the experiment. If more than one measurement exists, the uncertainty must be combined to reflect agreement or disagreement between measurements. In regions with little or no data, extrapolation in  $p_T$ ,  $x_{\text{lab}} = E_s/E_i$ , or  $E_i$  is required –  $E_i$  being the energy of the projectile and  $E_s$  being the energy of the produced meson. The uncertainty on the particle production should then reflect the amount of extrapolation needed.

Based on these considerations, Barr et al. divide the phase space into a given number of regions and assign discrete uncertainties on the particle production

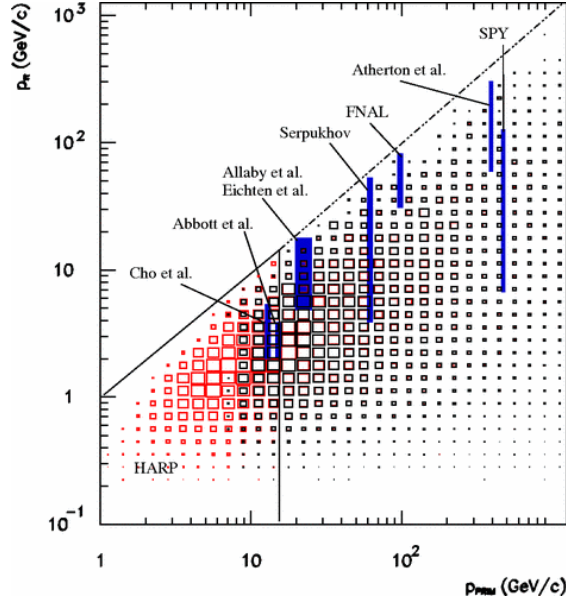


**Figure 7.2.** – The available data of particle production yield as a function of primary and secondary energy. The bands for each experiment represent the range of primary and secondary particle energies where measurements exist for at least one value of  $p_T$ . The boxes indicate the contribution of contained underground neutrino events as computed by simulation. The red and black boxes are the extremes of geomagnetic field effects for high and low geomagnetic latitude, respectively. From [63].

yield in each region (see Figure 7.3). The phase space in question is defined as  $E_i$  versus  $x_{\text{lab}} = E_s/E_i$ .

**Spelling out the Barr scheme** To illustrate the Barr scheme, consider a  $\sim 20$  GeV primary. Looking at Figure 7.2, considerable measurements on the production yield of pions with energy between 5 and 20 GeV have been performed. Thus the production rate can be determined without significant extrapolation. Indeed, Barr et al. assign an uncertainty of 5% for  $0.2 < x_{\text{lab}} < 0.6$  (Region  $E$  of the left diagram of Figure 7.3). This is somewhat below the errors quoted by a single experiment, to account for good agreement between measurements. At  $x_{\text{lab}} > 0.6$  the coverage of data decreases and extrapolation is required, resulting in a 10% uncertainty on pion production (Region  $F$  of the left diagram of Figure 7.3). At  $0.1 < x_{\text{lab}} < 0.2$  there is only one measurement, resulting in a 10% uncertainty (Region  $D_3$  of the left diagram of Figure 7.3). At  $x_{\text{lab}} < 0.1$  there are no measurements at all, leading to a 30% uncertainty (Region  $D_2$  of the left diagram of Figure 7.3).

As of 2006, no data for  $pA \rightarrow (\pi/K)^\pm \kappa$  existed for projectiles with energy larger than 500 GeV. To account for the extrapolation, an energy dependent uncertainty is introduced by Barr et al. [63]

$$u(E_i) = 12.2\% \times \log_{10} \left( \frac{E_i}{500\text{GeV}} \right). \quad (7.1)$$

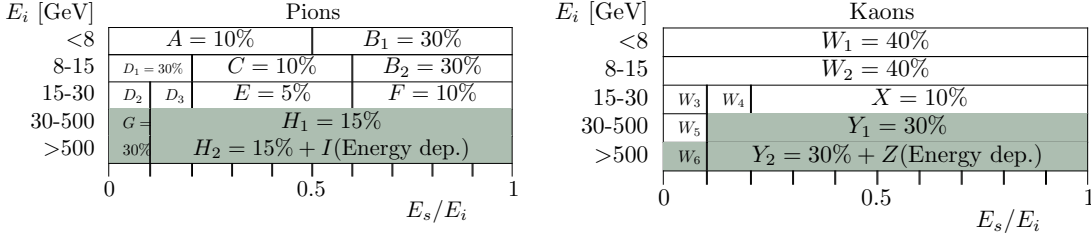


**Figure 7.3.** – Uncertainties assigned by Barr et al. to the production rates of pions (left) and kaons (right) as a function of  $x_{\text{lab}} = E_s/E_i$ ,  $E_i$  being the energy of the projectile and  $E_s$  being the energy of the produced meson. The regions of meson phase space that are of significance for the production of neutrinos in the DeepCore energy range are marked in green. Modified from [63].

The function  $u$  is then the definition of region  $I$  and  $Z$  in the diagrams of Figure 7.3. Thus the uncertainty in these regions increases with projectile energy so that the energy-dependent uncertainty on the production of pions with 10 TeV and 100 TeV energy is 16% and 28% respectively. Pions produced from projectiles with energy larger than 6 PeV is assigned a flat 50% uncertainty [63].

Using this method, uncertainties are assigned to the whole phase space. Though many of the experiments in Figure 7.2 have measured both pion and kaon yield, there are few measurements for the production of kaons from projectiles of energy less than 15 GeV. Thus, a large uncertainty of 40% is assigned. The uncertainty on kaon production is shown in the right diagram of Figure 7.3.

**The pion ratio** The Barr scheme applies to both meson and antimeson production. Figure 7.1 shows a 15% increase in the  $K^+$  (left) and the  $K^-$  (right) production. The effect on the neutrino flux is quite different. Positively charged kaons dominantly decay to  $\nu_\mu$  and  $\nu_e$ , so any modification to the  $K^+$  production will predominantly affect the  $\nu_\mu$  and  $\nu_e$  flux (and vice versa for the  $K^-$  production). However, as pions of some kaon decay channels will contribute to the neutrino flux, the modifications to the  $K^+$  production will also affect the  $\bar{\nu}_\mu$  and  $\bar{\nu}_e$  flux (and vice versa for the  $K^-$  production).

As the effect is distinct, the uncertainty on the meson and antimeson production should be introduced independently. Thus, the uncertainty on the neutrino flux is determined by 26 parameters in the Barr scheme (9 from  $\pi^+$ , 9 from  $\pi^-$ , 4 from  $K^+$ , and 4 from  $K^-$  production). However, we can reduce the number of parameters by considering that the uncertainty on the antimeson production is determined by the uncertainty on the meson–antimeson production ratio. The rate of neutrinos produced by  $(\pi/K)^\pm$  is given by:

$$R^\pm = \Phi^\pm(1 + \Delta^\pm), \quad (7.2)$$

where  $\Phi^+$  is the absolute neutrino flux and  $\Phi^-$  is the absolute antineutrino flux. The uncertainty on the flux,  $\Delta$ , is taken to be positive. We can thus define the ratio of neutrinos produced from  $(\pi/K)^+ / (\pi/K)^-$

$$\frac{R^+}{R^-} = \frac{\Phi^+(1 + \Delta^+)}{\Phi^-(1 + \Delta^-)} = \frac{\Phi^+}{\Phi^-} \alpha, \quad (7.3)$$

giving

$$\alpha = \frac{1 + \Delta^+}{1 + \Delta^-}, \quad (7.4)$$

$$\Delta^- = \frac{1 + \Delta^+}{\alpha} - 1, \quad (7.5)$$

$$\Delta R = \frac{1 + \Delta^+}{1 + \Delta^-} - 1 = \alpha - 1. \quad (7.6)$$

We thus have that

$$\Delta^- = \frac{1 + \Delta^+}{1 + \Delta R} - 1. \quad (7.7)$$

The uncertainty on the antimeson production is then expressed as a function of the uncertainty on the meson production and meson–antimeson production ratio.

The  $\pi^+/\pi^-$  ratio is determined to a precision of  $\Delta R = \pm 5\%$ . Using this, a 15% uncertainty on the  $\pi^+$  production, as an example, will result in a 10% uncertainty on the  $\pi^-$  production. The same simplification cannot be assumed in the kaon sector. The  $K^+/K^-$  ratio is poorly measured, and cannot be used to restrict the  $K^-$  production uncertainty. Thus the uncertainty on  $K^+$  and  $K^-$  must be kept independent. However, we have still reduced the number of parameters describing the  $\pi^\pm$  production uncertainty. The number of uncertainty sources is 18 in total (9 from  $\pi^\pm$ , 4 in  $K^+$ , 4 in  $K^-$ , and 1 for the  $\pi^+/\pi^-$  ratio).

**The reliability of the Barr scheme** The strict boundaries between regions are not realistic. It implies uncorrelated uncertainties, meaning that a shift in the production yield of one region of phase space will not affect the yield in other, neighboring regions of phase space. In their paper, Barr et al. investigate whether the regions are indeed correlated. This is done by drastically increasing the number of regions in  $x_{\text{lab}}$ . They repeat the exercise, this time increasing the number of regions in  $E_i$ . Both attempts show that increasing the number of regions has little effect on the neutrino flux. Though the method suggested by Barr and collaborators is subjective, it seems stable to changes in the number of regions and modifications of the definition of the region boundaries.

### 7.1.3 The Barr Scheme in MCEq

The information on particle production yield is contained within the C-matrix in MCEq. Each element of the C-matrix is itself a matrix,  $C_{k \rightarrow h}$ , of discretized

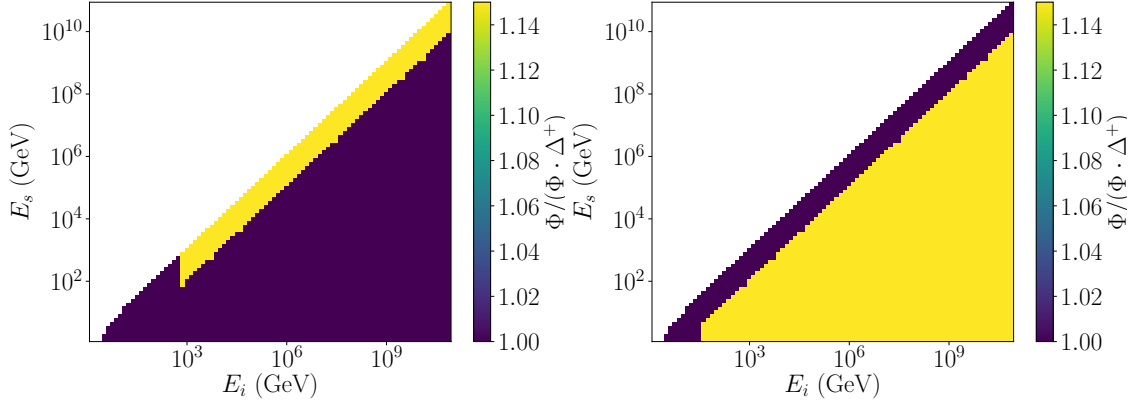


**Figure 7.4.** – Applying a Barr variable means to modify the particle production yield matrices of MCEq. The left modification matrix shows a 15% increase in pion production from projectiles with energy larger than 500 GeV and  $x_{\text{lab}} < 0.1$  (Barr variable  $H_2$ ). The right modification matrix shows a 15% increase in pion production for  $x_{\text{lab}} > 0.1$  (Barr variable  $G$ ).

differential cross sections (this is further explained in Section 5.5.3). As the Barr scheme applies to kaon and pion production, it is specifically the  $C_{p \rightarrow \pi^\pm}$  and  $C_{p \rightarrow K^\pm}$  matrices that will be modified under the Barr scheme.

«Applying» a Barr modification in MCEq refers to generating a modification matrix that has a percentage value in a region of phase space, as assigned by Barr et al. In Figure 7.4 the modification matrices of Barr variable  $H_2$  (left) and  $G$  (right) are shown, illustrating a 15% increase in a phase space defined by  $E_i$  and  $x_{\text{lab}} = E_s/E_i$ . This modification matrix is then multiplied by the  $C_{p \rightarrow (\pi/K)^\pm}$ , to yield an overall increase in the differential cross section in the given region.

The modified particle production yield matrix is then used when calculating the neutrino flux by the matrix cascade equation of equation (5.13). The result is an overall modification of the neutrino flux. As an example, Figure 7.1 (left) shows the effect of modifying the  $C_{p \rightarrow K^+}$  matrix with  $W = +30\%$  on the overall neutrino flux. The right plot of Figure 7.1 shows the effect of modifying the  $C_{p \rightarrow K^-}$  matrix with the same amount.

The Barr scheme only dictates the uncertainty on pion and kaon production. This entails that only four of approximately  $60 \times 60$   $C_{k \rightarrow h}$  matrices are subject to change under the Barr scheme. In practice, this means that uncertainty is introduced at a singular point along the path of neutrino production. With this approach, two aspects are neglected. (1) The meson can re-interact and produce a string of hadrons, before decaying to a meson. In this case, the introduced uncertainty will be that of the meson first produced. (2) Cosmic ray baryons might produce a string of baryons – each interaction introducing an uncertainty – before a kaon or pion is produced. This is particularly problematic because there are significant uncertainties associated with low energy proton production and neutron production.

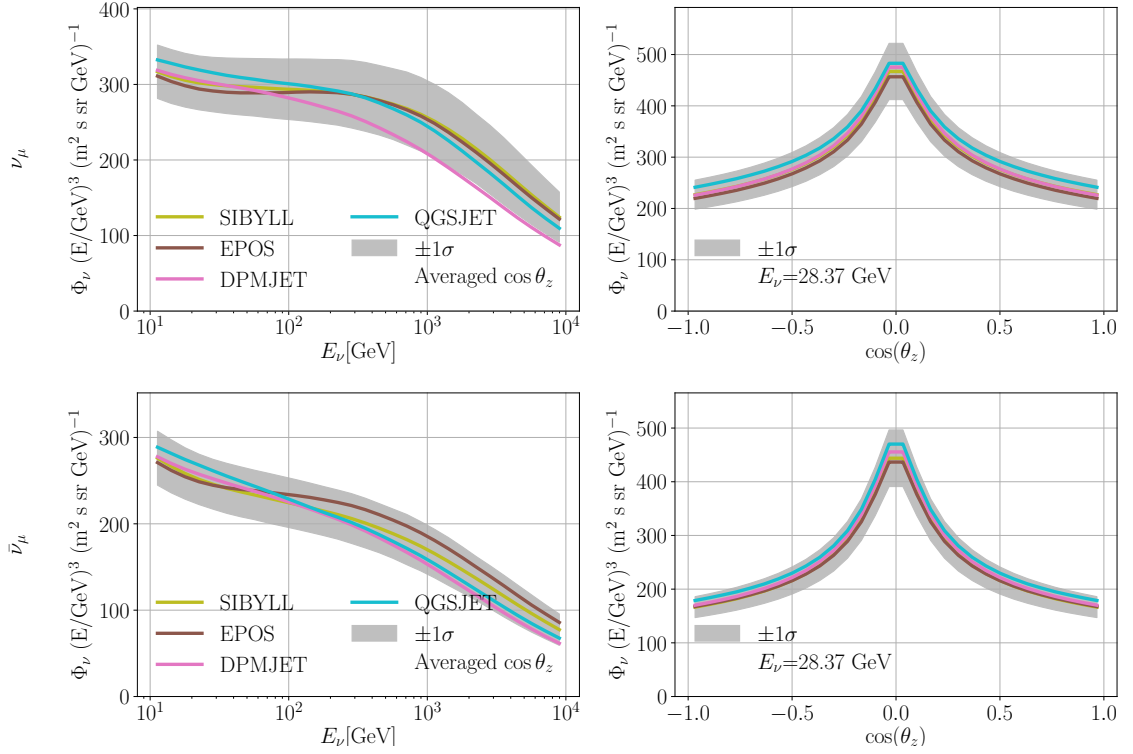


**Figure 7.5.** – The nominal  $\nu_\mu$  (upper) and  $\bar{\nu}_\mu$  (lower) flux as calculated with four different hadronic interaction models. The gray band indicate all uncertainties on particle production, i.e., all Barr variables, shifted by  $\pm 1\sigma$  as compared to the SIBYLL2.3c flux and added in quadrature.

#### 7.1.4 Spread in Interaction Model is Sub-dominant

Applying a Barr uncertainty modifies the  $C_{k \rightarrow h}$  matrix, yielding a flux estimate that deviates from the nominal neutrino flux. Several Barr uncertainties can be applied by adding the deviation in quadrature, under the assumption that Barr uncertainties are uncorrelated. In Figure 7.5 the nominal  $\nu_\mu$  (upper) and  $\bar{\nu}_\mu$  (lower) flux is taken to be that calculated with the SIBYLL2.3c interaction model. Deviations from the nominal caused by taking each uncertainty on  $(\pi/K)^\pm$  production into account, are added in quadrature to form a  $1\sigma$  uncertainty band (gray) around the nominal flux. Atmospheric neutrino flux estimates calculated using three other hadronic interaction models are plotted for comparison<sup>1</sup>. All estimates are within  $\sim 1\sigma$  of the nominal flux. This means that if the uncertainty on particle production is determined through model comparison, the estimated uncertainty will be less than the data-driven uncertainties of the Barr scheme. It indicates that the choice of hadronic interaction model has a sub-leading effect on the atmospheric neutrino flux estimate.

Figure 7.5 is reproduced for the  $\nu_e$  and  $\bar{\nu}_e$  flux in Appendix D.

<sup>1</sup>I would like to give credit to A. Fedynitch and J.P. Yáñez for advising me on which models to compare: SIBYLL2.3c[53], QGSJETII-04[51], EPOS LHC[52], and DPMJET-III 2017[64]

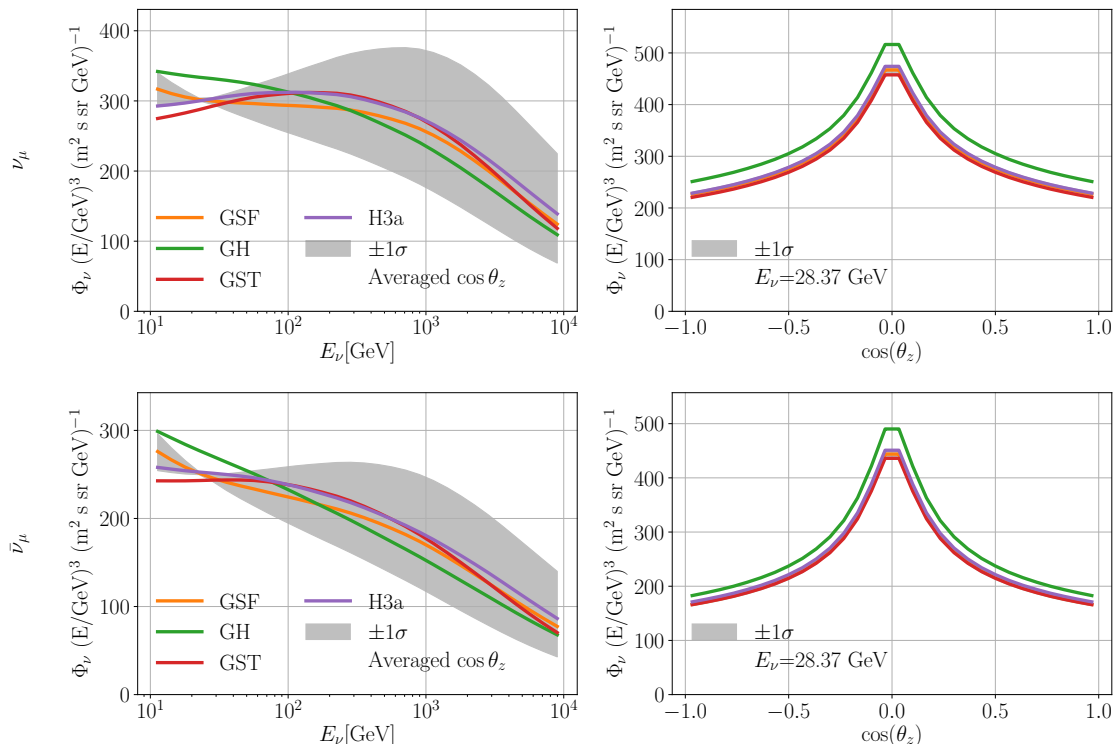


**Figure 7.6.** – The nominal  $\nu_\mu$  (upper) and  $\bar{\nu}_\mu$  (lower) flux as calculated with four different cosmic ray models. The gray band indicates the result of shifting the spectral index with  $\pm 1\sigma = 0.1$ , assuming that the nominal flux is that calculated with GSF.

## 7.2 Uncertainties on the Cosmic Ray Flux

In the DeepCore energy range ( $10 \text{ GeV} \lesssim E_\nu \lesssim 100 \text{ GeV}$ ), the atmospheric neutrinos are primarily produced by cosmic ray particles with energy less than 3 PeV. In this region, below the «knee», the cosmic ray spectrum can be described by a single power law  $E^{-\gamma}$ ,  $\gamma$  being the spectral index. As neutrinos in this energy range are mainly produced in decay, the spectral index of the neutrino flux will approximately follow that of the primaries. Under this assumption, the uncertainty stemming from the cosmic ray flux can be assigned a single parameter  $\Delta\gamma$ . This approach has been adopted in previous IceCube analyses and is carried on in the work presented here.

In previous IceCube analyses, the uncertainty on the cosmic ray spectrum has been estimated to  $\Delta\gamma = \pm 0.1$ . Modifying the spectrum by  $E^{\Delta\gamma}$  corresponds to tilting the energy dependency of the flux around a pivot point. In previous IceCube analyses, the pivot point has been  $E_\nu \approx 24 \text{ GeV}$ . In Figure 7.6, the nominal  $\nu_\mu$  (upper) and  $\bar{\nu}_\mu$  (lower) flux is taken to be that calculated using the *Global Spline Fit* model (GSF) [65]. The  $1\sigma$  uncertainty is then estimated, under the same assumptions as prior IceCube analyses (gray band). The flux estimates

calculated using the GH[46], H3a[44], and GST[45] cosmic ray models are plotted for comparison in Figure 7.6<sup>2</sup>.

**The value of the pivot point and shift in spectral index** A problem with the approach presented above is that the values of the  $\Delta\gamma$  and the pivot point are subjective. For instance, if the objective of the approach is to describe the spread in model predictions, Figure 7.6 shows that the pivot point should be set to a higher energy and  $\Delta\gamma$  can be fixed at a lower value than  $\pm 0.1$ . However, as previously discussed, there are apparent drawbacks with basing uncertainty estimates on model comparisons.

A measure of the uncertainty on cosmic ray data is contained within the GSF model. The GSF model is determined by splining available data and yields a covariance matrix that represents the experimental uncertainty of the input data[65]. The value of  $\Delta\gamma$  and the pivot point can be determined by comparing to the data-driven GSF uncertainties, under the assumption that the spectral index of the cosmic ray flux and atmospheric neutrino flux is the same.

**The problematic pivot point** Another more fundamental problem with estimating the uncertainty by shifting the spectrum around a pivot point is that it implies that the uncertainty approaches zero at the pivot point. This is clear from the zenith distributions of Figure 7.6 (right column), where the flux of neutrinos with energy  $E_\nu \approx 28$  GeV is plotted. Being close to the pivot point, the  $1\sigma$  uncertainty is negligible. This is unrealistic. A potential solution can be to find a different model, for instance scaling the flux by a constant, based on a comparison to GSF uncertainties.

To sum up, incorporating the uncertainty stemming from the cosmic ray spectrum as a shift in the neutrino spectral index has several shortcomings. However, it is still the chosen approach in this work. This is due to (1) consistency, as previous IceCube analyses have used the same approach, (2) conservatism, as no better model is evident, (3) and practicalities, as I did not have access to the GSF uncertainties during the course of this work. In the following, the uncertainty stemming from the cosmic ray spectrum is thus estimated as a shift in the spectral index of the neutrino flux. Figure 7.6 is reproduced for the  $\nu_e$  and  $\bar{\nu}_e$  flux in Appendix D.

### 7.3 Overall Uncertainty on the Atmospheric Neutrino Flux

In this chapter it has been suggested to estimate the uncertainty on the atmospheric neutrino flux by estimating the uncertainty on each model input of the neutrino flux calculation, ignoring the muon energy loss and atmospheric density model uncertainty. The individual uncertainties are then propagated through in MCEq to yield an overall uncertainty on the neutrino flux.

The total uncertainty on the  $\nu_\mu$  (left) and  $\bar{\nu}_\mu$  (right) flux is plotted in Figure 7.7. In the DeepCore energy range, an overall, energy-dependent uncertainty

<sup>2</sup>The choice of relevant models is made based on advice from A. Fedynitch and J.P. Yáñez.

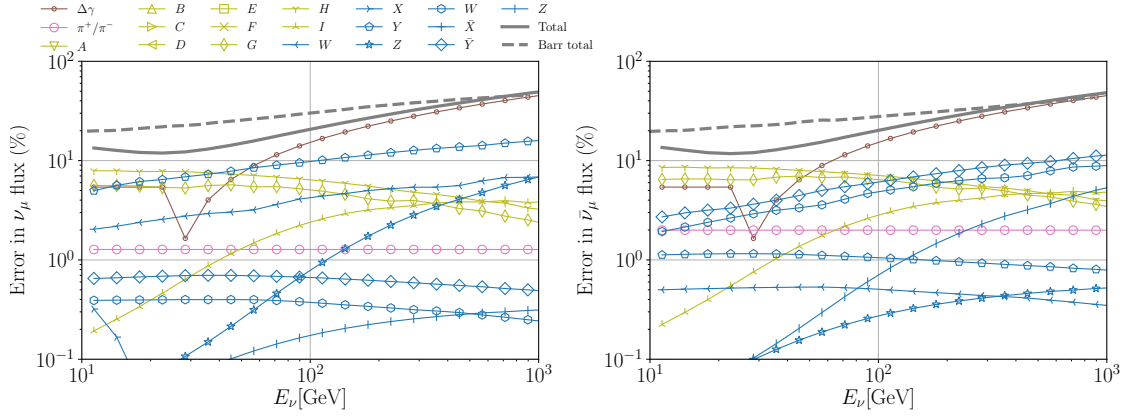


**Figure 7.7.** – Breakdown of the uncertainties (averaged over zenith angles) on the  $\nu_\mu$  (left) and  $\bar{\nu}_\mu$  (right) flux, with different regions of meson production as a function of neutrino energy. The capital letters correspond to the Barr variables of Figure 7.3. Green curves are uncertainties stemming from pion production, blue from kaon production. The uncertainty on the pion ratio is represented by  $\pi^+/\pi^-$  (pink). The brown curve represents the uncertainty arising from the spectral index of the cosmic ray spectrum. The topmost, gray line is the total uncertainty on the flux. The estimate by Barr et al. is plotted in gray, dashed line for comparison [63].

of 10%-50% is found. This is comparable to results found by Barr et al. (gray, dashed line in Figure 7.7). No single hadronic source of uncertainty dominates. At higher energies, the flux of neutrinos produced in pion decay decreases, so the uncertainty on pion production becomes less dominant at higher energies (green curves). The contribution from kaon production uncertainty increases with energy (blue curves), as the flux of neutrinos produced in kaon decays increases. At higher energies, the uncertainty arising from the cosmic ray spectrum (brown curve) is dominating the overall uncertainty on the neutrino flux.

It is unlikely that primaries of energy  $E_i < 30$  GeV give a significant contribution to the neutrino flux at DeepCore energies. Indeed, applying all Barr variables of Figure 7.3 shows that only six Barr variables affect the flux of neutrinos within the DeepCore energy range:  $G$ ,  $H$ , and  $I$  on the pion production, and  $W$ ,  $Y$ , and  $Z$  on the kaon production (marked in green in Figure 7.3). Figure 7.7 is reproduced for the  $\nu_e$  and  $\bar{\nu}_e$  flux in Appendix D.

## 7.4 Uncertainties of Neutrino Ratios

Up until this point, all calculations have been done using absolute atmospheric neutrino fluxes. In this section, it is demonstrated that there is an advantage of computing the ratio of atmospheric neutrino fluxes. The objective of this section is to reproduce results by Barr et al., thereby verifying that the implementation in MCEq is true to the approach suggested by Barr et al.

**Cancellation of uncertainties in ratios** At low energies each muon produced in the atmosphere is associated with one neutrino and one anti-neutrino, and any

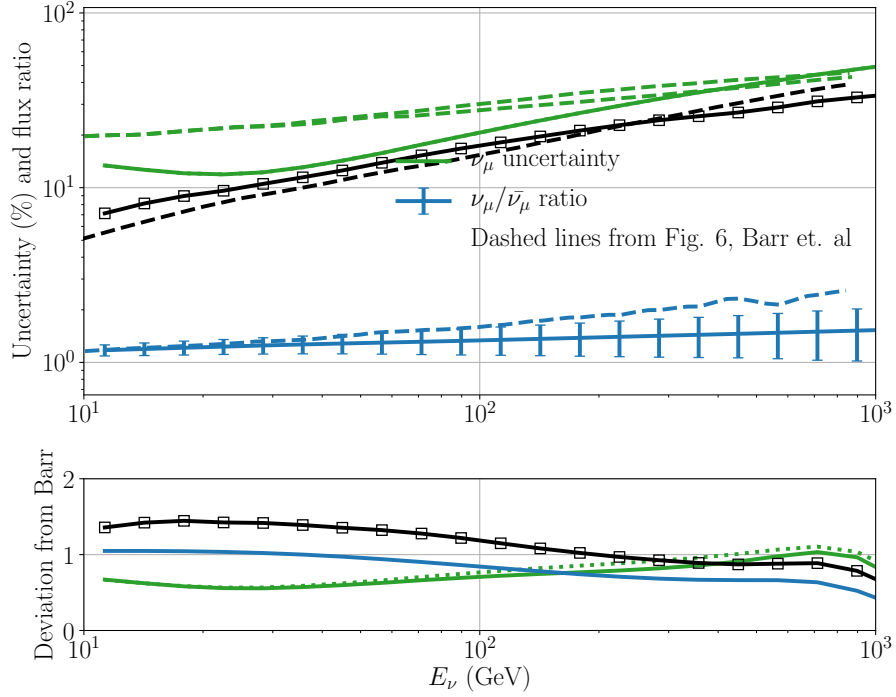
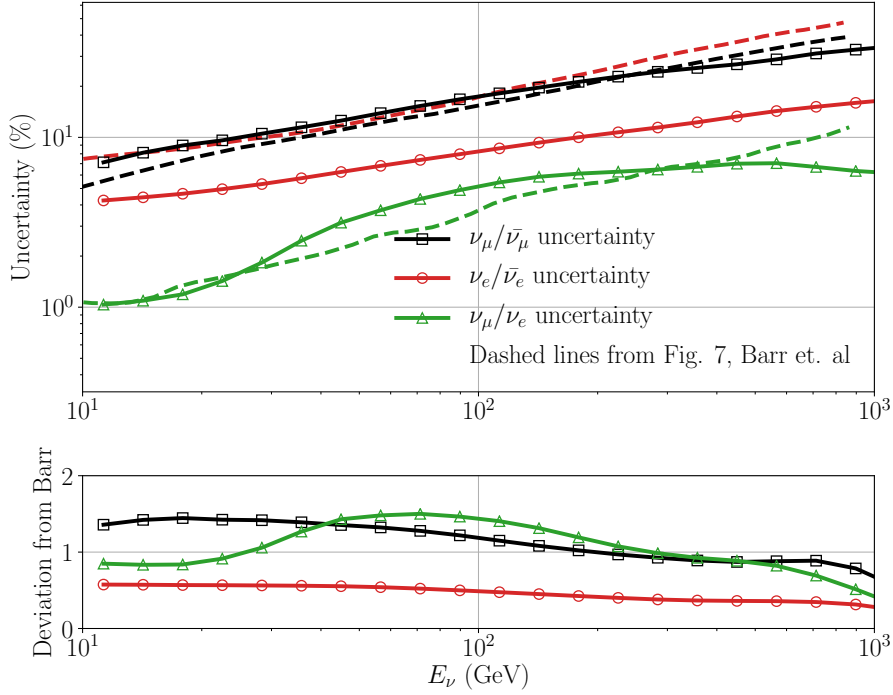


**Figure 7.8.** – Dashed lines are digitally interpolated from Figure 6 of [63], full lines are the same results derived with MCEq. The uncertainty in % on the  $\nu_\mu$  and  $\bar{\nu}_\mu$  flux is plotted in green. The  $\nu_\mu/\bar{\nu}_\mu$  flux is estimated (blue), and the uncertainty on the ratio in % is plotted in black.

overestimation of pions (and thus muons) will result in a similar overestimation on the neutrino and antineutrino flux. Thus the numerator and denominator will have similar uncertainties in a  $\nu_\mu/\bar{\nu}_\mu$  ratio and will cancel. The cancellation is most powerful at low energies where most muons decay in the atmosphere. At higher energies, where an increasing number of muons hit the ground before decay, and only one neutrino is produced per pion decay, the cancellation ceases to have an effect. At  $E_\nu \gtrsim 100$  GeV there is hardly any cancellation at all. The cancellation is demonstrated in Figure 7.8, where the individual  $\nu_\mu$  and  $\bar{\nu}_\mu$  uncertainties (green) are larger than the uncertainty on the  $\nu_\mu/\bar{\nu}_\mu$  ratio (black). The effect of cancellation decreases with increasing energy.

**MCEq and Barr comparison** The MCEq estimate for the uncertainty on the absolute muon neutrino flux deviates from that predicted by Barr (green curves of Figure 7.8). This is due to a «dip» in the uncertainty around the spectral index pivot point at  $E_\nu \approx 24$  GeV, which is demonstrated with the brown curve of Figure 7.7. Thus, the MCEq estimate is 50% compared to that of Barr et al. around the pivot point, and converges at higher energies.

**Flux flavor ratios** Figure 7.9 presents the uncertainty on three neutrino flux ratios:  $\nu_\mu/\bar{\nu}_\mu$  (black, also shown in Figure 7.8),  $\nu_e/\bar{\nu}_e$  (red), and  $(\nu_\mu + \bar{\nu}_\mu)/(\nu_e + \bar{\nu}_e)$  (green) digitized from Figure 7 of [63] (dashed lines) and computed with MCEq (full lines). A breakdown of the individual sources of uncertainty is shown in Figure 7.10.



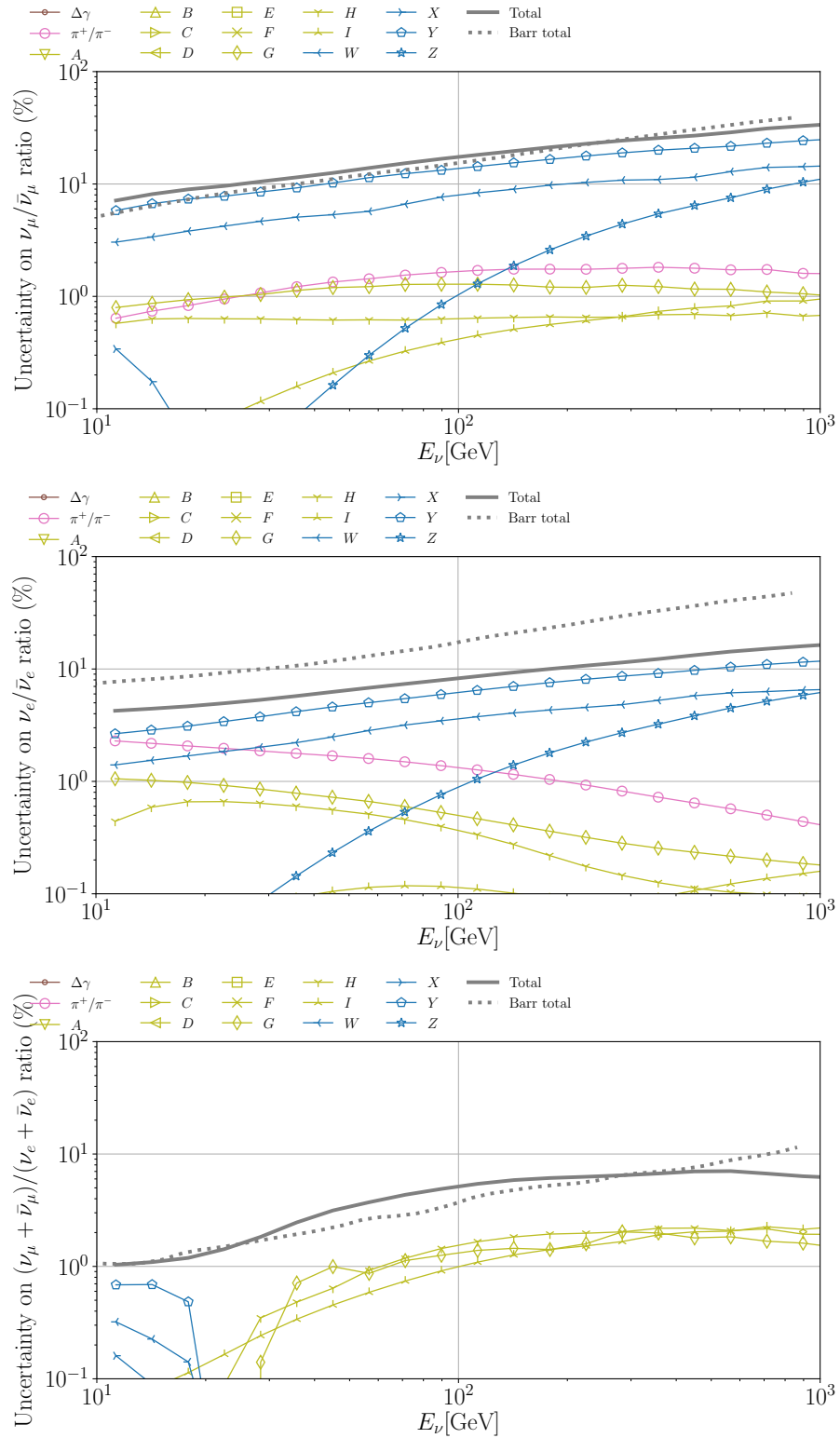
**Figure 7.9.** – The uncertainty in % on the  $\nu_\mu/\bar{\nu}_\mu$  flux (black),  $\nu_e/\bar{\nu}_e$  flux (red) and  $(\nu_\mu + \bar{\nu}_\mu)/(\nu_e + \bar{\nu}_e)$  flux (green). Dashed lines are digitally interpolated from Figure 7 of [63], full lines are the same results derived with MCEq.

Figure 7.10 shows that the uncertainty on the spectral index completely cancels out when taking the flavor ratio of neutrino fluxes. Thus the same «dip» as observed in the absolute neutrino uncertainty is not seen in the  $\nu_\mu/\bar{\nu}_\mu$  ratio. The disagreement between MCEq and Barr estimated  $\nu_e/\bar{\nu}_e$  uncertainty is due to a difference in the kaon contribution to the electron neutrino production.

IceCube is not sensitive to the charge of the lepton produced in a neutrino interaction, and can therefore not take advantage of the cancellation of uncertainties in the  $\nu_\mu/\bar{\nu}_\mu$  and  $\nu_e/\bar{\nu}_e$  flux ratios. The  $(\nu_\mu + \bar{\nu}_\mu)/(\nu_e + \bar{\nu}_e)$  ratio will however appear experimentally as a ratio between cascade and track events, and the cancellation of uncertainty can be utilized in IceCube analyses.

**Directional ratios** Cancellations of uncertainties also occur in ratios of neutrinos from different directions. At  $E_\nu \gtrsim 10$  GeV there is a complete cancellation of the uncertainty in the up/down neutrino ratio. This is because the cosmic ray particles and air showers are not affected by the geomagnetic field at high energies, and there will in principle be no difference between the neutrino flux at any two locations at Earth.

At low energies, a similar ratio of neutrinos from above and from the horizon is from muon decay. Down is defined as  $\cos \theta_z > 0.6$ , horizontal as  $|\cos \theta_z| < 0.3$ . Thus, the uncertainty cancellation in the down/horizontal ratio will be more pronounced at low energies. This is observed for both the electron and muon neutrino flux in Figure 7.11. As the energy increases fewer muons from above will decay to neutrinos before hitting the ground. Thus, the effect of the cancellation decreases with energy and the uncertainty on the down/horizontal ratio increases.



**Figure 7.10.** – Breakdown of uncertainties in flavor ratios with different regions of hadron production, shown as a function of neutrino energy. (top)  $\nu_\mu/\bar{\nu}_\mu$  (middle)  $\nu_e/\bar{\nu}_e$  (bottom)  $(\nu_\mu + \bar{\nu}_\mu)/(\nu_e + \bar{\nu}_e)$

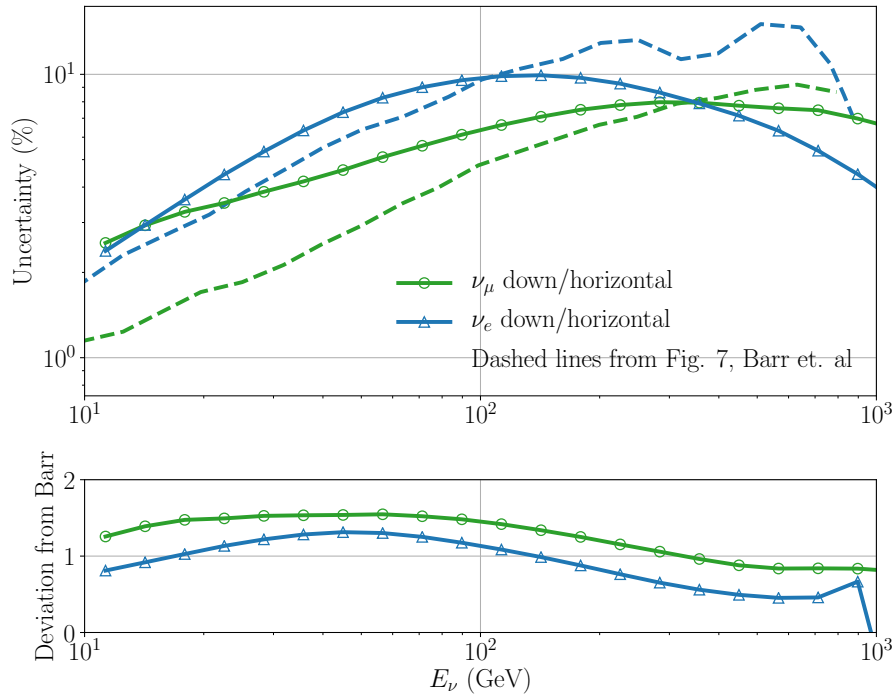


**Figure 7.11.** – Uncertainties in directional ratios as a function of neutrino energy, for  $\nu_\mu + \bar{\nu}_\mu$  (green) and  $\nu_e + \bar{\nu}_e$  (blue). Dashed lines are digitally interpolated from Figure 9 of [63], full lines are the same results derived with MCEq.

At energies  $\mathcal{O}(1)$  TeV, the decay of muons produced in pion decay ceases to be a dominant mode of neutrino production, and the contribution from the pion production uncertainty to the overall uncertainty drops. This is shown in the breakdown of the individual sources of uncertainty on the down/horizontal ratio in Appendix E.

Doing analyses in IceCube on directional neutrino ratios has the potential of limiting the systematic uncertainty from the neutrino flux estimate. Further studies should aim to quantify the potential gain.

All aspects of the atmospheric neutrino flux discussed in previous chapters are tied together in a new analysis method in PISA, which is the analysis tool of low energy IceCube analyses. The topic of this chapter is the development and testing of this model.

In the following sections, all results are shown for the muon neutrino and antineutrino flux. Corresponding results on the electron neutrino and antineutrino flux can be found in Appendix D.

## 8.1 The PISA Framework

The key experimental quantities in IceCube are the length of neutrino propagation – which is proportional to the zenith arrival direction  $\cos \theta_z$  – and neutrino energy  $E_\nu$ . As such analyses in IceCube are conducted using data that is binned in a  $(\cos \theta_z, E_\nu)$ -grid.

**Likelihood Analysis** The objective of a physics analysis is to investigate to what degree a theoretical model can describe data. For instance, given a model of neutrino oscillations where all parameters are known, except the number of tau neutrinos to expect, how well is the observed 2D distribution described? The unknown parameter – in this example the number of tau neutrinos – is called the *physics parameter*. To answer the question, data must be generated within the relevant theoretical model, which often requires Monte Carlo (MC) methods. The simulated data is binned on the same 2D grid to form a «template».

The likelihood of data  $x_i$  and physics parameter  $\omega$  is

$$\mathcal{L}(x_1, x_2, \dots, x_n | \omega) = \prod_i P(x_i | \omega), \quad (8.1)$$

where  $P(x_i | \omega)$  is the probability to observe the data  $x_i$  assuming  $\omega$ . Thus the likelihood for multiple values of the physics parameter  $\omega$  can be derived. By choosing the value of  $\omega$  that yields the maximum likelihood value, the best physics parameter to describe the data is found  $\hat{\omega}$ .

Above it is assumed that all parameters in the theoretical model are fixed, except the physics parameter. This is rarely the case. For example, all neutrino oscillation parameters have an associated uncertainty. The systematic uncertainties in an experiment are sometimes called *nuisance parameters*. In this work, the relevant nuisance parameters are the 19 sources of flux uncertainty introduced in the previous chapter. For every value of the physics parameters  $\omega$  several templates with different combinations of nuisance parameter values must be generated. As multiple values of  $\omega$  are taken into account when maximizing the likelihood, the MC simulation of templates requires a quickly increasing amount of computational time.

**Weighting** To avoid repeated simulation of events every time the value of a nuisance parameter is changed, the data of the templates can be «weighted» to account for the change in parameters. This can be done because the nuisance

parameters of the physics processes are independent, e.g., changing the value of  $\Delta m_{32}^2$  does not affect the value of the spectral index of the atmospheric neutrino flux.

Each simulated neutrino of a given flavor  $\beta$  is assigned an individual weight  $w_\beta$ . The weight corresponds to the sum over the atmospheric flux  $\Phi_\alpha$  over all initial flavors  $\alpha$ , and the probability of oscillating into  $\beta$ ,  $P_{\alpha \rightarrow \beta}^{\text{osc}}$  [66]

$$w_\beta \propto \sum_{\alpha} \Phi_{\alpha}(\omega_{\text{flux}}) \times P_{\alpha \rightarrow \beta}^{\text{osc}}(\omega_{\text{osc}}). \quad (8.2)$$

Thus taking the nuisance parameters of the oscillation model or flux model into account requires only a single generated template. The parameters associated with detector response cannot be assumed to be uncorrelated with the other nuisance parameters, and thus a full MC simulation must be performed for each template.

**Staged approach** In PISA the physical processes are broken up into *stages*. The simulated data enters a *pipeline*, in which each physical process is applied as a stage. Stages that are built on the weighting scheme calculate a transformation matrix that is applied to the data coming from the previous stage in the pipeline. One of the first stages to be applied in the pipeline is generally the flux stage. As an illustration, if the spectral index nuisance parameter is defined as a large positive value, the flux stage will find a transformation matrix that yields small weights to high-energy events and large weights to low-energy events. The MC distribution is thus altered before entering the next stage of the pipeline.

Since the production of  $\nu_\tau$  is negligible in the atmosphere, the flux stage only takes into account  $\nu_e$  and  $\nu_\mu$ .

The staged approach in one dimension is illustrated in Figure 8.1. In step (1) the flux stage is applied. In step (2) the oscillation stage is applied. The dotted green line illustrates the alteration when changing one parameter in the oscillation stage. Step (3) is the effective area of the detector. The three transformation matrices are multiplied to yield an expected event distribution (lower left). Taking detector response into account (4), the final expected observable distribution is shown in the lower right. This template can then be compared to data using a likelihood analysis to find the value of the physics parameters that best describes the data.

In the following, I will describe the current flux stage and the new flux stage implemented in PISA. For further information on the other stages of PISA refer to [66].

## 8.2 The Honda Flux Stage

The current flux stage in PISA is based on Monte Carlo generated tables<sup>1</sup>. The calculations – hereafter referred to as the «Honda flux» – are performed by M. Honda and collaborators and were last updated February 2015 [48].

<sup>1</sup><http://www.icrr.u-tokyo.ac.jp/~mhonda/nflx2014/index.html>

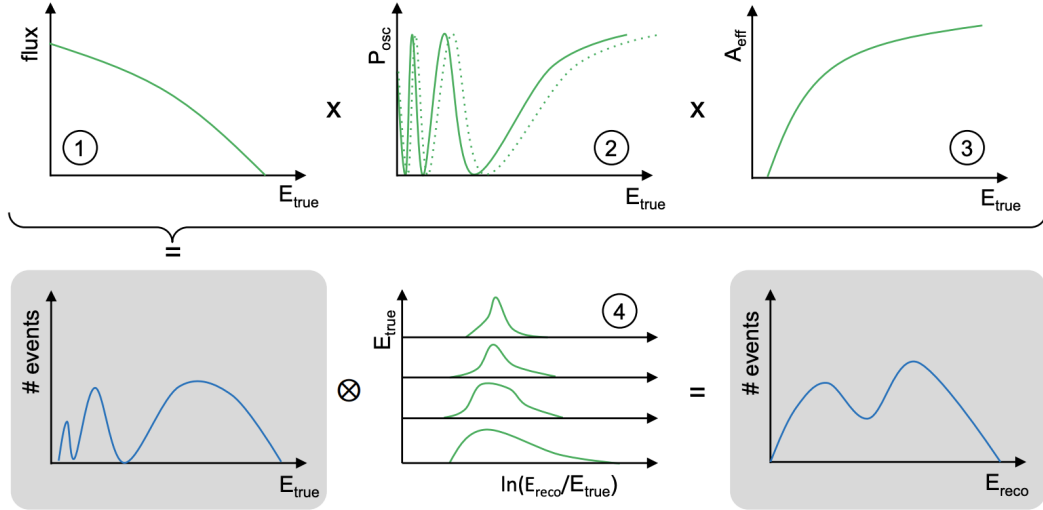


**Figure 8.1.** – Illustration of the staged approach shown in one dimension (energy). The first stages (step 1-3) are applied for the energy of the event  $E_{\text{true}}$ . The product of these yields the expected event distribution (lower left). The expected spectrum is then smeared out with energy-dependent energy resolution functions (step 4). The reconstructed event rate spectrum is shown in the lower right plot. The effect of changing a nuisance parameter in the oscillation stage is illustrated in the dotted green line in step 2. From [66].

**The Honda Flux Estimates** The Honda prediction is a full 3D exclusive flux calculation. This means that the path of each air shower particle is traced, resulting in a lateral spread of the air shower. The Honda flux thus has a zenith, azimuth, and energy dependence. The azimuthal dependence, which is found to be small at the South Pole at the energies relevant for IceCube, is currently averaged out in the PISA implementation.

Additionally, the predictions from Honda et al. take variations in solar activity and season into account and are generated at the maximum and minimum of the solar cycle, and for summer and winter seasons.

The Honda flux is estimated using a particular choice of models for hadronic interactions, the atmospheric density profile, the geomagnetic field, and the cosmic ray spectrum. For hadronic interactions, the calculation relies on the DPMJET-III [54] model at high energies,  $E_\nu \geq 32$  GeV, though modified to reproduce the muon spectra observed by the BESS group [48]. Below 32 GeV the JAM interaction model is used [67]. The group has compared the DPMJET-III–JAM combination to other model combinations and found a better agreement to measurements at balloon altitudes [68]. The latest Honda fluxes are calculated using the NRLMSISE-00 [50] atmospheric model and the IGRF [69] geomagnetic model. As for the cosmic ray model, they use a model based on AMS and BESS data, with a spectral index of  $\gamma = -2.71$  above 100 GeV [48]. The model is described in [46], which is the same reference as for the GaisserHonda-model within the CRFluxModel-module of MCEq[70]. As the same selection of models is

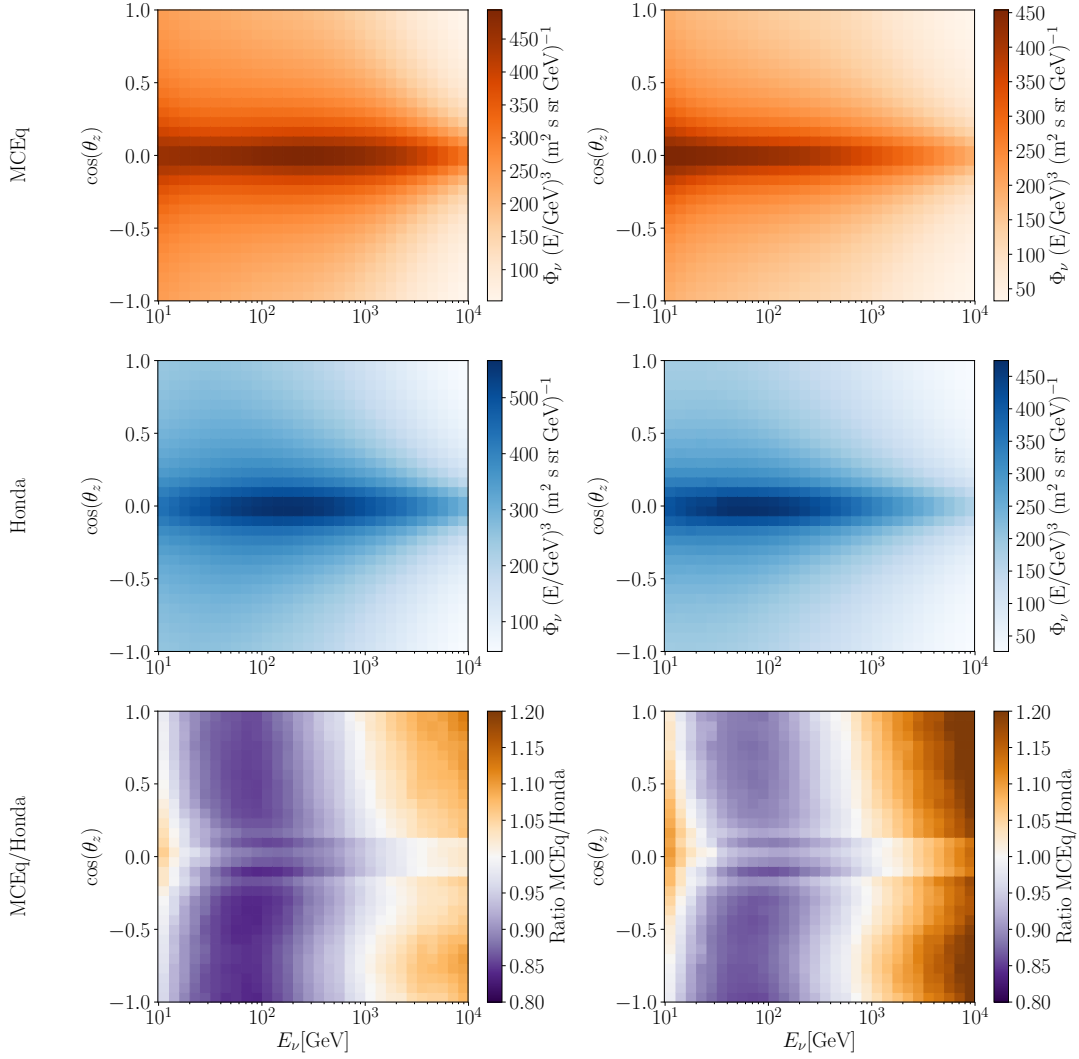


**Figure 8.2.** – The nominal  $\nu_\mu$  (left column) and  $\bar{\nu}_\mu$  (right column) flux as calculated with the MCEq PISA stage (topmost, orange row) and the Honda stage (middle, blue row). The ratio of the two is shown in lower row.

not available in MCEq, a direct comparison between the effect of the different calculation methods of MCEq and Honda is not possible.

The nominal  $\nu_\mu$  (left) and  $\bar{\nu}_\mu$  (right) flux estimated by Honda et al. and implemented as a stage in PISA are shown in the middle row of Figure 8.2.

### 8.3 A New Flux Stage in PISA

In the developed MCEq stage the nominal flux is found by running MCEq. As MCEq is not subject to statistical fluctuations, it will yield the same result every time the calculations are run. Thus, the muon and electron neutrino flux is calculated, splined, and stored in an external file.

As the basis for the PISA staged approach is to reweight the same template, the underlying MC data is unaltered when the template is regenerated. Thus, the precomputed splines only have to be evaluated once, which saves considerable computational time. The nominal  $\nu_\mu$  (left) and  $\bar{\nu}_\mu$  (right) flux, calculated with

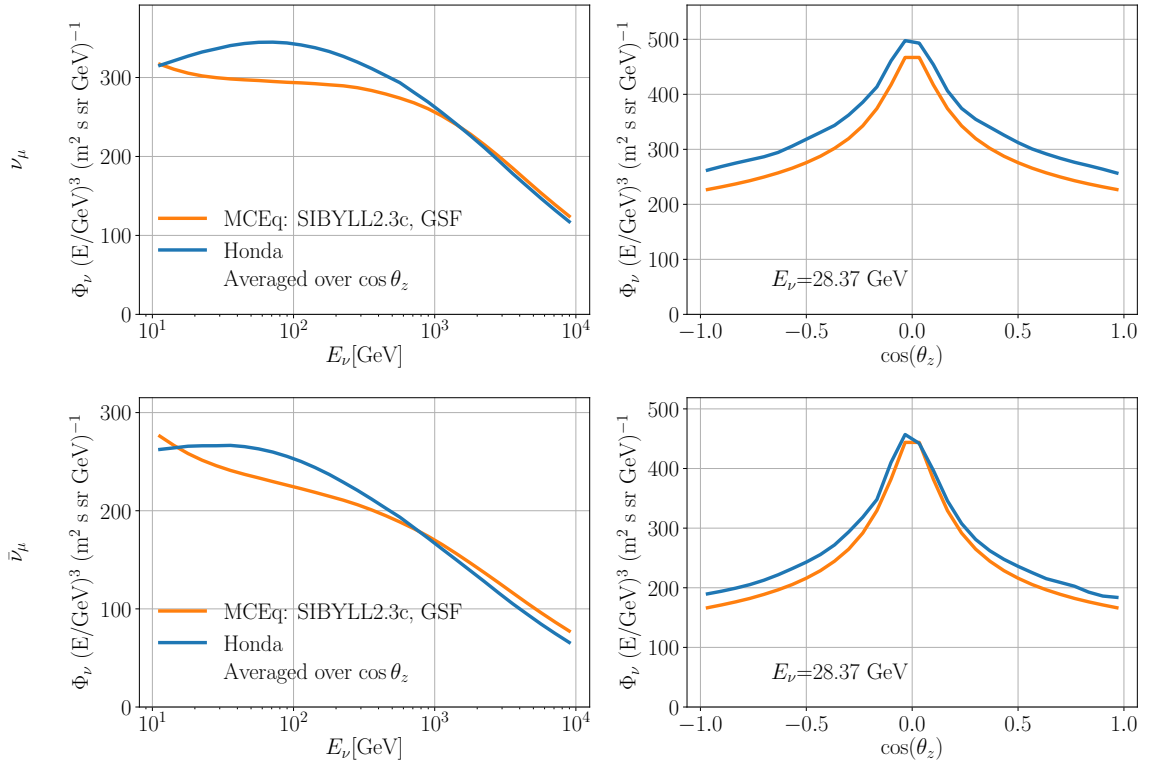


**Figure 8.3.** – The nominal  $\nu_\mu$  (upper) and  $\bar{\nu}_\mu$  flux as calculated with the MCEq PISA stage (orange) and the Honda PISA stage (blue)

SIBYLL2.3c and GSF, as evaluated on the same grid as the Honda stage is shown in the topmost row of Figure 8.2.

The lowermost row of Figure 8.2 shows the ratio between the nominal  $\nu_\mu$  (left) and  $\bar{\nu}_\mu$  (right) flux calculated with MCEq and that of Honda. Compared to Honda, MCEq predicts a lower flux at low energies and a higher flux at high energies. This is more easily seen when plotting in one dimension (see Figure 8.3). The disagreement is discussed in Section 8.5.

## 8.4 Flux Nuisance Parameters

Up until this point, the nominal fluxes as calculated with the Honda and MCEq PISA stages have been compared. In this section, the uncertainty on that estimate is taken into account.

**Evaluating uncertainties on the flux in the Honda stage** The uncertainty on the Honda flux is partly based on parameterizations of the neutrino flux ratio uncertainties presented in Barr et. al [63] and reproduced in Section 7.4. The uncertainty on the  $\nu_e/\bar{\nu}_e$ ,  $\nu_\mu/\bar{\nu}_\mu$ ,  $(\nu_\mu + \bar{\nu}_\mu)/(\nu_e + \bar{\nu}_e)$ , and the  $\nu$  down/horizontal ratios are parameterized, and define the uncertainty on the flux. An uncertainty on the spectral index,  $\Delta\gamma$ , is also implemented.

For each physics parameter value, the template is reweighted for multiple values of nuisance parameters. The variation in the nuisance parameters are constrained by Gaussian priors, based on the work in Barr et al. For instance, assuming that the only flux nuisance parameter is the spectral index, generating

**Table 8.1.** – Nuisance Parameters of the Honda (left) and MCEq (right) PISA stage

Parameter	Honda stage		Parameter	MCEq stage	
	Variance	Range		Variance	Range
$\Delta\gamma$	$1\sigma = 0.1$	$\pm 5\sigma$	$\Delta\gamma$	$1\sigma = 0.1$	$\pm 5\sigma$
$\nu/\bar{\nu}$	$1\sigma = 1.0$	$\pm 3\sigma$	$\pi^+/\pi^-$	$1\sigma = 0.3$	$\pm 5\sigma$
$\nu_\mu/\nu_e$	$1\sigma = 0.05$	$\pm 5\sigma$	$A$	$1\sigma = 0.1$	$\pm 5\sigma$
$\nu$ down/horizontal	$1\sigma = 1.0$	$\pm 3\sigma$	$B$	$1\sigma = 0.3$	$\pm 5\sigma$
			$C$	$1\sigma = 0.1$	$\pm 5\sigma$
			$D$	$1\sigma = 0.3$	$\pm 5\sigma$
			$E$	$1\sigma = 0.05$	$\pm 5\sigma$
			$F$	$1\sigma = 0.1$	$\pm 5\sigma$
			$G$	$1\sigma = 0.3$	$\pm 5\sigma$
			$H$	$1\sigma = 0.15$	$\pm 5\sigma$
			$I$	$1\sigma = 0.122$	$\pm 5\sigma$
			$W$	$1\sigma = 0.4$	$\pm 5\sigma$
			$X$	$1\sigma = 0.1$	$\pm 5\sigma$
			$Y$	$1\sigma = 0.3$	$\pm 5\sigma$
			$Z$	$1\sigma = 0.122$	$\pm 5\sigma$
			$\bar{W}$	$1\sigma = 0.4$	$\pm 5\sigma$
			$\bar{X}$	$1\sigma = 0.1$	$\pm 5\sigma$
			$\bar{Y}$	$1\sigma = 0.3$	$\pm 5\sigma$
			$\bar{Z}$	$1\sigma = 0.122$	$\pm 5\sigma$

$\Delta\gamma = 0$  will correspond to the nominal flux. The  $1\sigma$  variance of this parameter is 0.1, so the reweighting matrices are more likely to be generated with an uncertainty on the spectral index of less than 0.1. The priors on the flux nuisance parameters are listed in Table 8.1. In Figure 8.4 all flux nuisance parameters in the Honda stage are set to  $+1\sigma$ , and the resulting changes in predicted flux added in quadrature (blue, middle row).

**Evaluating uncertainties on the flux in the MCEq stage** Rather than relying on plot parameterizations like the Honda stage, the implementation of hadronic uncertainty in the MCEq stage is based on splines of the altered flux with each Barr variable applied.

In Chapter 7, we studied the effect of applying one or more Barr variables at  $1\sigma$ . We saw that applying  $+1\sigma$  uncertainty on meson production resulted in an increased neutrino flux, i.e., the modified flux  $\phi_+$ . However, within the PISA stage, the nuisance parameters must be allowed to assume a range of values between  $\pm 5\sigma$ . Thus, rather than splining the  $1\sigma$  modification, we spline the derivative with respect to each Barr variable. A positive uncertainty on meson production results in the modified flux of  $\phi_+$ . We then find the modified flux assuming a negative uncertainty,  $\phi_-$ . The derivative for a small step-size  $\delta$  is then

$$\frac{d\phi}{dB} = \frac{\phi_+ - \phi_-}{2\delta}, \quad (8.3)$$

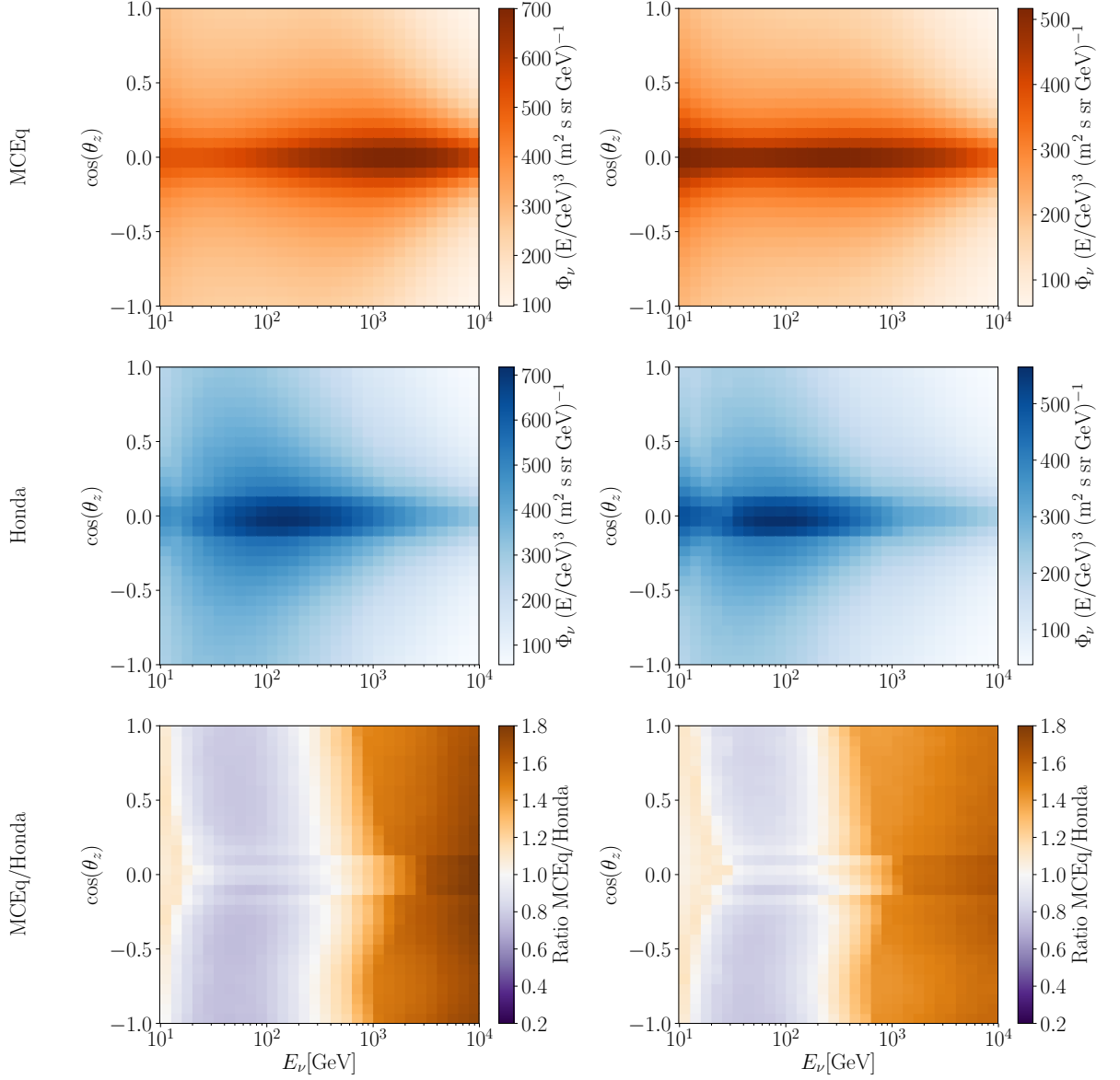


**Figure 8.4.** – All flux nuisance parameters shifted by  $+1\sigma$  and added in quadrature as calculated in the MCEq stage (topmost, orange) and in the Honda stage (middle, blue) for the  $\nu_\mu$  (left column) and  $\bar{\nu}_\mu$  (right column) flux. The ratio between the systematic fluxes are plotted in the lowermost row.

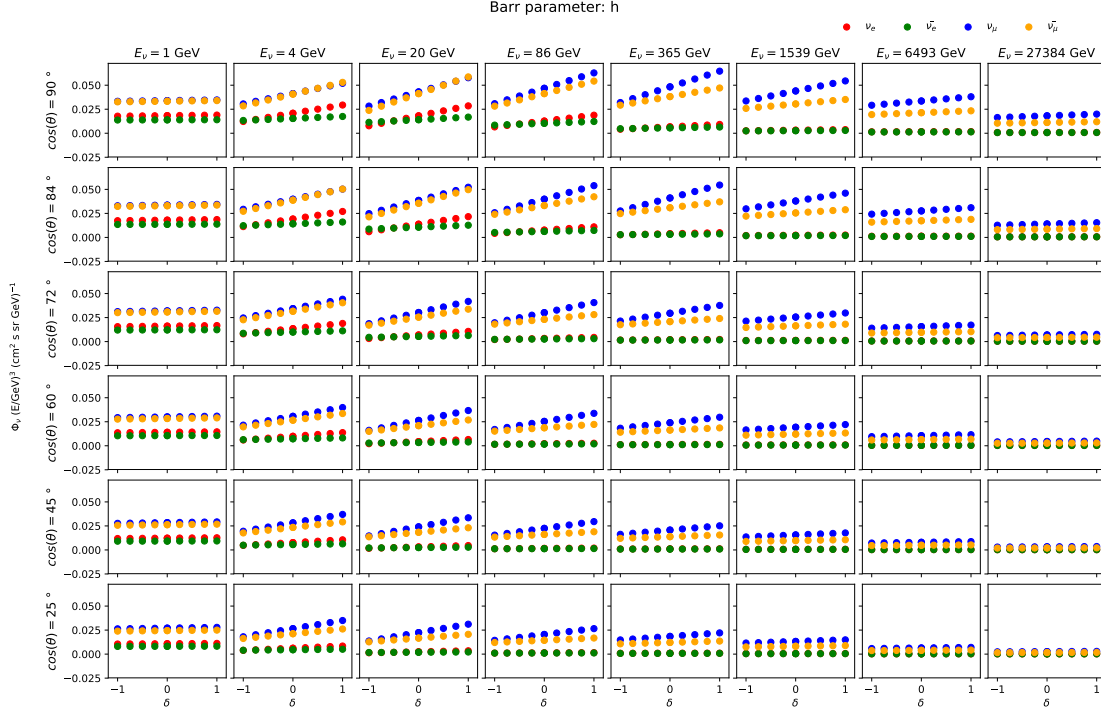


**Figure 8.5.** – The flux modification as a result of applying an uncertainty on the  $\pi^+$  production in the  $H$  region varies linearly with changing values of the magnitude of the modification. The result is valid for  $\nu_\mu$  (blue),  $\bar{\nu}_\mu$  (yellow),  $\nu_e$  (red) and  $\bar{\nu}_e$  (green). The result is shown for 6 different zenith angles, and 8 different energies

where  $B$  is the considered Barr variable. This is done for several points on a  $(E, \cos\theta_z)$ -grid, yielding the derivative of the Barr modification.

In this scheme, the derivatives of the Barr modifications are assumed to be linear. In Figure 8.5 this assumption is tested for 6 zenith angles, and 8 different energies. The result shows that modifications to the  $\nu_\mu$ ,  $\bar{\nu}_\mu$ ,  $\nu_e$ , and  $\bar{\nu}_e$  flux are linear for modifications of magnitude  $-100\% \lesssim b \lesssim +100\%$ ,  $b$  being the magnitude of the nuisance parameter. Figure 8.5 shows the result for the  $H$  Barr variable, but all Barr variables were tested and found to modify the flux linearly in the range  $-100\% \lesssim b \lesssim +100\%$ .

The uncertainty on the cosmic ray flux is taken into account by introducing an uncertainty on the spectral index of the energy-dependent neutrino flux

$$\Delta\phi = \left( \frac{E}{24\text{GeV}} \right)^{\Delta\gamma}. \quad (8.4)$$

The flux with uncertainties hereafter referred to as the *systematic flux* is then calculated as

$$\phi_{\text{sys}} = (\phi_{\text{nom}} \cdot \Delta\phi) + \left( b \cdot \frac{d\phi}{dB} \right). \quad (8.5)$$

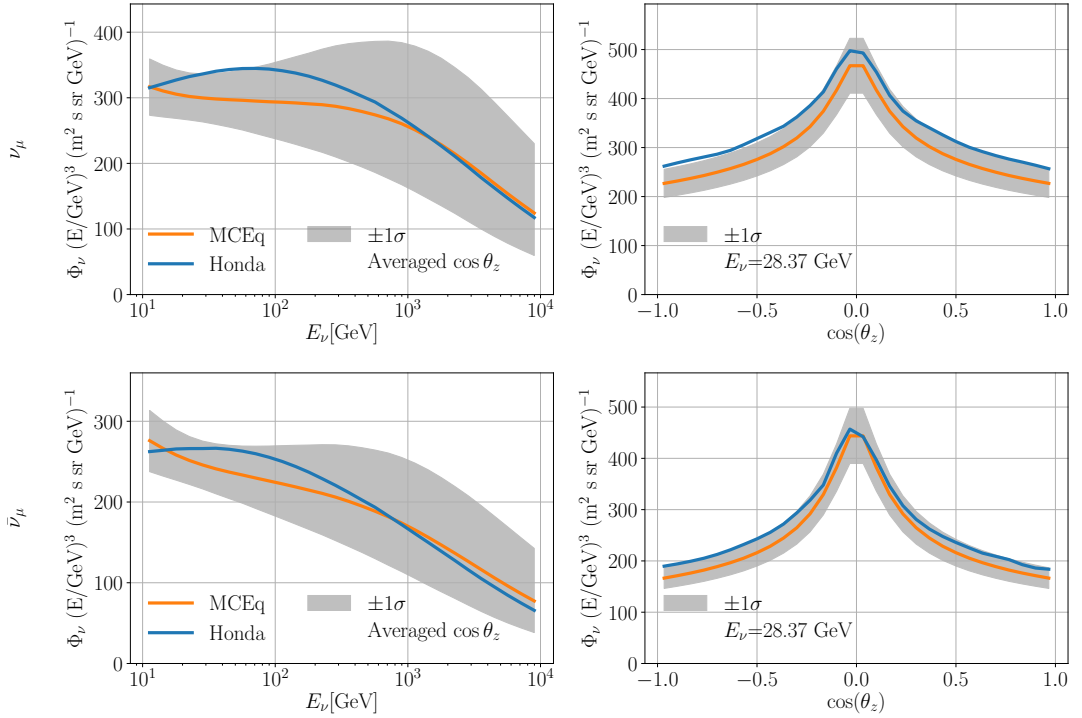


**Figure 8.6.** – The nominal  $\nu_\mu$  (upper) and  $\bar{\nu}_\mu$  (lower) flux as calculated with MCEq (orange) and Honda (blue stage). All nuisance parameters in the MCEq stage shifted by  $\pm 1\sigma$  and added in quadrature to make up the grey  $1\sigma$  band.

The flux template is then generated with the MCEq calculated nominal flux, multiplied by a shift in the spectral index which is generated from a prior defined in Table 8.1, plus a positive or negative increase that is due to the meson production uncertainty. The value of the meson production uncertainty,  $b$ , can assume values as defined in Table 8.1.

In Figure 8.4 all flux nuisance parameters in the MCEq stage are set to  $+1\sigma$ , and the resulting changes in predicted flux added in quadrature (orange, topmost row).

## 8.5 The MCEq stage vs. the Honda stage

The nominal flux predicted by Honda and MCEq disagrees (Figure 8.3). No comparison to atmospheric neutrino data is done in this work, so there is no indication that one prediction is «more correct» than the other. Recent results show that MCEq predictions agree with the best fit of the atmospheric muon flux measured in IceCube [71]. However, the Honda flux is not included in the study for comparison. Further studies must be undertaken in order to reveal whether the disagreement between the MCEq and Honda prediction is a real concern.

Taking the uncertainties on the flux into account, the disagreement is within  $\sim 1\sigma$  of the MCEq predicted flux. This is demonstrated in Figure 8.6. As the Honda prediction is within  $\sim 1\sigma$  of the MCEq flux, the likelihood will only be moderately penalized if the best fit flux nuisance parameters result in a flux prediction that

agrees with the Honda estimate. In other words, it is a possible outcome of the maximization of the likelihood that the MCEq and Honda prediction agree.

It is predominately the uncertainty on the spectral index that causes the Honda prediction to be within  $\sim 1 \sigma$  of the MCEq prediction. It is problematic to introduce such a large uncertainty without it being founded in data when the effect might potentially conceal model differences or relevant physics. This should be improved in future work on flux estimates within the IceCube collaboration.

**Advantages of the Honda flux stage** MCEq has lower energy limit of  $E_\nu \approx 10$  GeV. As the Honda flux calculation is a full 3D Monte Carlo simulation, it takes the geomagnetic field and the solar field into account. This means that the prediction is valid for the neutrino flux below  $E_\nu \approx 10$  GeV. At the moment, this is in the lower energy range of IceCube DeepCore, and the MCEq and Honda stage should be equally appropriate approaches. However, with the IceCube Upgrade, the sensitivity of IceCube will improve down to  $\sim 1$  GeV. In this case, the present implementation of the MCEq stage is no longer valid.

**Advantages of the MCEq flux stage** The MCEq stage is much more flexible than the Honda flux stage. Any user within the IceCube collaboration can estimate the atmospheric neutrino flux based on any selection of hadronic interaction, cosmic ray, and atmospheric density models. Newer models can also be implemented as they are developed. The user must then generate input-tables in the appropriate format, as discussed in Chapter 5. However, this requires less computational time than running the full Monte Carlo calculation in the manner of Honda et al. This allows new experimental cosmic ray or hadronic interaction data to be implemented consecutively.

The treatment of the flux systematic is more physically motivated within the MCEq stage, compared to the Honda stage. The parameterization of uncertainties of flavor ratios and directional ratios that makes up the basis for the Honda flux uncertainty are assumed to be uncorrelated. Within the MCEq stage, the uncertainty on meson production is applied directly as a modification on the  $(E, \cos \theta_z)$ -grid, keeping the correlation between flavor and directional ratios. Accounting for these correlations should decrease the contribution from neutrino flux uncertainties on the overall systematic uncertainty in analyses.

Additionally, the parameterizations of the Barr results that the Honda uncertainties are based on are calculated *including* the uncertainty on the cosmic ray flux. Thus, when both assuming the Barr parameterized uncertainties *and* an uncertainty on the spectral index, the uncertainty from cosmic ray flux is counted two times in the Honda stage. This will probably result in a larger systematic uncertainty from the atmospheric neutrino flux.

There are thus several reasons to expect that the developed MCEq stage should result in a lower systematic flux uncertainty. This prospect is investigated in the next section.

## 8.6 Atmospheric Tau Neutrino Appearance in DeepCore

Most neutrino oscillation experiments are based on measuring electron neutrino and muon neutrino appearance or disappearance. Prior to the IceCube results only two experiments (OPERA and SK) had measured the appearance of tau neutrinos through oscillation [72][73]. Tau neutrinos can appear through  $\nu_e \rightarrow \nu_\tau$ ,  $\nu_\mu \rightarrow \nu_\tau$ , and  $\nu_\tau \rightarrow \nu_\tau$ . The  $\nu_e \rightarrow \nu_\tau$  channel is experimentally disfavored as the signature of  $\nu_e$  and  $\nu_\tau$  is very similar, and as the magnitude of the oscillations is low due to the small mixing. The  $\nu_\tau \rightarrow \nu_\tau$  channel has the disadvantage of a very low flux of atmospheric  $\nu_\tau$  at energies relevant for neutrino oscillations. In practice,  $\nu_\mu \rightarrow \nu_\tau$  is the only feasible channel to measure oscillation parameters related to the tau neutrino. In the standard oscillation picture, the dominant appearance mode of  $\nu_\mu \rightarrow \nu_\tau$  is given by [74]

$$P_{\nu_\mu \rightarrow \nu_\tau} = \sum_{j,k} U_{\mu j} U_{\tau j}^* U_{\mu k}^* U_{\tau k} \exp\left(i \frac{\Delta m_{jk}^2 L}{2E_\nu}\right) \quad (8.6)$$

$$\approx \cos^4 \theta_{13} \sin^2 2\theta_{23} \sin^2 \left(\frac{\Delta m_{31}^2 L}{4E_\nu}\right) \quad (8.7)$$

where  $U$  are elements of the PMNS matrix,  $\Delta m_{31}^2 = m_3^2 - m_1^2$  are the mass-squared splitting,  $L$  is the oscillation baseline and  $E_\nu$  the neutrino energy. The mixing angles are defined as  $\theta_{13}$  and  $\theta_{23}$ .

As the  $\nu_\tau$  interaction is indistinguishable from interactions other than  $\nu_\mu$  CC in DeepCore, the  $\nu_\tau$  appearance analysis cannot be done on an event-by-event basis. However, if  $\nu_\tau$  do appear, this can be observed as a distortion in the 2D distribution of energy and zenith angle for tracks and cascades. Thus the analysis is based on a comparison between templates and observed distribution.

The physics parameter of the IceCube  $\nu_\tau$  appearance analysis is the  $\nu_\tau$  normalization,  $N_{\nu_\tau}$ . This is defined as the ratio of the measured  $\nu_\tau$  flux to that expected when assuming best-fit nuisance parameters, including muon neutrino disappearance oscillation parameters. This means that if  $N_{\nu_\tau} = 1$  we observe the same number of events as expected with standard neutrino oscillations.

The data  $x_i$  is compared to the template by minimizing the  $\chi^2$  of binned data for different values of  $N_{\nu_\tau}$  and nuisance parameters. The  $\chi^2$  function is defined as [30]

$$\chi^2 = \sum_{i \in \{\text{bins}\}} \frac{(N_i^{\text{exp}} - N_i^{\text{obs}})^2}{N_i^{\text{exp}} + (\sigma_i^{\text{exp}})^2} + \sum_{j \in \{\text{syst}\}} \frac{(s_j - \hat{s}_j)^2}{\sigma_{s_j}^2}, \quad (8.8)$$

where  $N_i^{\text{exp}}$  and  $N_i^{\text{obs}}$  is the expected and observed number of events in the  $i$ 'th bin respectively. The second term of equation (8.8) is the sum of penalty terms for nuisance parameters, where  $s_j$  is the central value of the prior of the  $j$ 'th systematic parameter,  $\hat{s}_j$  is the maximum likelihood estimator, and  $\sigma_{s_j}^2$  is the prior on the systematic uncertainty. The effect of the penalty terms is that if

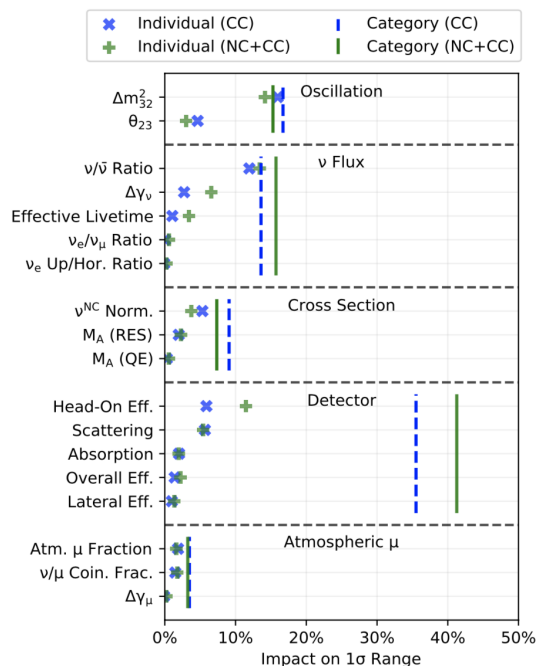


**Figure 8.7.** – The relative impact from each systematic uncertainty on the final  $1\sigma$  confidence interval width in the  $\nu_\tau$  appearance analysis. The line shows the combined systematic uncertainty from each group of systematics. From [30].

the variance on the nuisance parameter is large, or the estimated value of the nuisance parameter is far away from its expected nominal value, large deviations will be disfavored in the minimization.

In order to establish the individual contribution, or rank, of each systematic uncertainty, tests were completed where a specific parameter was fixed to its nominal value, and the analysis was rerun to examine the impact on the test statistic. The tests were done for individual systematic uncertainties, as well as groups of systematic uncertainty. Figure 8.7 shows the impact of each systematic uncertainty on the  $1\sigma$  confidence interval of the tau neutrino normalization. It shows that detector systematic uncertainties together account for 41% of the total systematic uncertainty, and atmospheric neutrino flux uncertainties and the uncertainty on neutrino oscillation parameters each account for  $\sim 15\%$  of the systematic uncertainty on the  $\nu_\tau$  normalization physics value. Thus limiting the uncertainty on the atmospheric neutrino flux will result in a more sensitive measurement of  $N_{\nu_\tau}$ .

The  $\nu_\tau$  analysis of [30] was done using the Honda stage, with flux nuisance parameters as defined in Table 8.1. Scanning over different values of the physics parameter, i.e.,  $0 < N_\tau < 2$ , the minimum of the test statistics given the best-fit nuisance parameters was found (blue curve of Figure 8.8). To test the effect of flux nuisance parameters on the  $\nu_\tau$  normalization sensitivity, all other nuisance parameters of the analysis were fixed at the mean value. The test statistic was based on MC generated data.

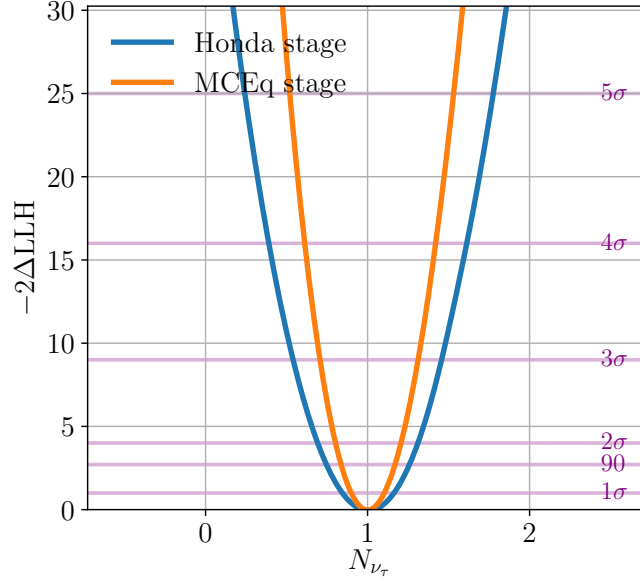


**Figure 8.8.** – Test statistic on Monte Carlo data for the tau neutrino appearance analysis. The width of the curve shows the precision of the measurement. All nuisance parameters are turned off, except the ones associated with the Honda (blue) stage and the MCEq (orange) stage.

The analysis was then rerun, with the same setup but with the MCEq stage taking the place of the Honda stage. The result is shown in Figure 8.8 (orange curve). The best-fit values for the individual nuisance parameters can be found in Appendix F. With the Honda stage, the physics parameter was determined to  $N_{\nu_\tau} = 1.00 \pm 0.17$ , with all nuisance parameters except the flux systematic uncertainties fixed at the mean value. Using the MCEq stage yielded  $N_{\nu_\tau} = 1.00 \pm 0.11$ . Thus the  $1\sigma$  sensitivity is on  $N_{\nu_\tau}$  in the tau neutrino appearance analysis improved by around 35%.

The result of this work is a developed neutrino flux stage in PISA, based on MCEq. The stage is completed and tested, and is to be implemented in the PISA framework and used in future IceCube analyses. The new flux stage is more physically motivated and ensures a more correlated treatment of the flux uncertainties. It is expected that this new flux uncertainty treatment will improve the precision of the new generation of DeepCore oscillation measurements currently under development.

The result of this work has been the development of a new, improved way of handling systematic uncertainties from the atmospheric neutrino flux in IceCube. Previously the flux treatment in IceCube relied on precomputed Monte Carlo tables by Honda et al.[48]. The new method is an improvement as it is more flexible to updates. If new models of hadronic interaction or the cosmic ray spectrum are developed and found to describe data better, the new method does not require re-running Monte Carlo simulations with updated models. The user can herself choose an appropriate combination of models. Additionally, if updated measurements are done on meson production, the uncertainties can be adjusted within the developed software without requiring reparameterizations.

Previously the uncertainty on the atmospheric neutrino flux has been based on parameterizations of results derived by Barr et al.[63]. The uncertainty on the atmospheric neutrino flux has been described in terms of the uncertainty on the neutrino–antineutrino ratio, and the up/horizontal neutrino flux ratio. These uncertainties are treated uncorrelated. This is unrealistic, as both sets of uncertainties fundamentally are caused by uncertainty on the meson production. In the developed stage, the effect of meson production uncertainty on neutrino flavor and direction is treated as being correlated. This entails an overall improvement in the treatment of neutrino flux systematic uncertainties in IceCube.

**Implementing PYTHIA in MCEq** The work presented here has primarily been focused on the uncertainties stemming from particle production. I have also extended an event generator, PYTHIA, to be used for atmospheric neutrino flux predictions, which is a new aspect of PYTHIA. This work aims to implement PYTHIA as a hadronic interaction model in MCEq, but work is yet to be done on the interface between these two softwares.

**Better treatment of the cosmic ray spectrum uncertainty** The uncertainty stemming from the cosmic ray spectrum has been somewhat sidelined in this work. The current implementation of the cosmic ray flux uncertainty is the same as the previous method and is not optimal. Implementing the cosmic ray flux uncertainty by shifting the spectral index of the neutrino flux is not the most favorable approach, especially at higher energies when the power law behavior is broken. As a continuation of this work, a better approach should be found. In this thesis, it is suggested to base the cosmic ray flux uncertainty on the GSF model.

**The IceCube Upgrade** The planned IceCube Upgrade will likely improve detector calibration considerably. The detector systematic uncertainty is currently on the order of 40% and is expected to decrease after the IceCube Upgrade is able to take data and conduct new calibrations. If so, the uncertainty on the atmospheric neutrino flux will have an even larger contribution to the overall systematic uncertainty in IceCube analyses. The work presented here is promising in this regard, as it indicates that the developed method will decrease the flux systematic uncertainty. However, the method developed builds on MCEq, which has a lower energy limit of  $E_\nu \gtrsim 10$  GeV. With the Upgrade, IceCube will be sensitive to a neutrino flux with energies extending down to 1 GeV. This flux cannot

presently be accurately modeled with MCEq. Work is being done on implementing geomagnetic field effects in MCEq to support the Upgrade. Independently of this work, two strategies can be investigated in order to use the developed scheme in the Upgrade

1. One can use 3D Monte Carlo flux estimates at low energies, and MCEq at higher energies where the 1D approximation is valid, and work out a method of extrapolation between the two energy regimes.
2. Methods of utilizing directional ratios can be explored. The up/down neutrino flux ratio will only be dependent on the geomagnetic field, and thus applying an uncertainty on the ratio, as found by Barr et al., can potentially describe the effect of the geomagnetic field on the 1D MCEq estimate.

Overall the new method is more physically motivated, and should thus yield a more accurate flux prediction. The prediction deviates from estimates by Honda et al., but within  $1\sigma$ . To determine the accuracy of the developed method comparison to neutrino flux data should be performed.

As the flux uncertainties are treated more correlated, the developed method should also be more precise, yielding smaller systematic uncertainties from the atmospheric neutrino flux. The developed method has been applied to an IceCube analysis on tau neutrino appearance, and the systematic uncertainty on  $1\sigma$  level was found to decrease by around 35% when taking only the flux nuisance parameters into account. The method should be applied to additional analyses before concluding whether it in general yields a smaller systematic flux uncertainty. However, it is expected that this new treatment will improve the sensitivity of the new generation of DeepCore oscillation studies currently under development.

# List of Figures

2.1	The Standard Model of particle physics. From [12] . . . . .	4
2.2	(a) Neutrinos can interact weakly either via charged current (left) or neutral current (right) interactions. (b) The diagram of a neutrino-quark scattering interaction. From [18]. . . . .	9
2.3	Neutrino (left) and antineutrino (right) charged current cross section. From [19]. . . . .	10
3.1	The geometry of Cherenkov radiation. From [18]. . . . .	11
3.2	Schematic of an IceCube Digital Optical Module (DOM) . . . . .	13
3.3	Layout of the IceCube detector. From [25]. . . . .	14
3.4	Possible experimental signatures of neutrino interaction in DeepCore. From [27] . . . . .	15
3.5	Event view of $\nu_e$ , $\nu_\mu$ , and $\nu_\tau$ events in the DeepCore detector. From [29]. . . . .	16
3.6	The survival probability of muon neutrinos undergoing oscillations. From [31] . . . . .	17
3.7	The IceCube Upgrade array geometry. From [33]. . . . .	18
3.8	Fully contained atmospheric $\nu_\mu$ (left) and $\nu_\tau$ (right) in the DeepCore (dashed lines) and Upgrade (full line) arrays. From [33]. . . . .	19
4.1	All particle cosmic ray data and parameterizations of the spectrum. Figure from [42] by R. Engel. . . . .	21
4.2	Particle multiplicity in an air shower as a function of altitude. From [47]. . . . .	22
4.3	(a) The hadron-air cross section, (b) The decay lengths for a selection of hadrons . . . . .	24
4.4	The total flux (upper) of electron (blue), muon (red) and tau neutrinos (green) and the flavor ratio (lower) averaged over zenith arrival angles. . . . .	26
4.5	Particle production modes of the atmospheric muon (left), electron (middle) and tau (right) neutrino flux. From [42]. . . . .	27
4.6	Azimuth angle dependence of neutrino flux at the South Pole. From [48]. . . . .	29
4.7	The zenith dependence of the muon neutrino flux at three different neutrino energies . . . . .	30
4.8	Seasonal variations of the atmospheric neutrino flux . . . . .	31

5.1	(a) A particle production table for $p \rightarrow \pi^+$ generated in SIBYLL2.3c, (b) Inclusive $\pi^+$ cross sections for different projectile proton energies $E_p$ . . . . .	37
6.1	PYTHIA calculated $\bar{p}(p)p$ , $K^-(K^+)p$ and $\pi^-(\pi^+)p$ cross sections compared to the COMPAS fit . . . . .	43
6.2	$K^+p$ cross section implemented in PYTHIA compared to COMPAS data and fit . . . . .	44
6.3	Distributions from PYTHIA/Angantyr on the differential cross section, for $K^+ + p \rightarrow C^+ + \kappa$ (left) and $K^+ + p \rightarrow \pi^- + \kappa$ (right), with respect to rapidity, compared to data. . . . .	46
6.4	Distributions from PYTHIA/Angantyr on the differential cross section with respect to pseudo-rapidity, compared to data. . . . .	47
6.5	(a) Multiplicity of negatively charged hadrons produced in kaon-aluminium collisions, and (b) kaon-gold collisions. . . . .	48
6.6	(a) Inclusive cross section of $pN \rightarrow \pi^+$ , (b) Inclusive cross section of $K^+N \rightarrow \pi^+$ generated in PYTHIA . . . . .	49
7.1	The absolute electron and muon neutrino flux modified by introducing an uncertainty on $K^+$ (left) and $K^-$ (right) production yield . .	51
7.2	Available accelerator data for primaries with $1 \text{ GeV} < E_i < 1 \text{ TeV}$ . From [63]. . . . .	52
7.3	Barr blocks: uncertainty of pion and kaon production. Modified from [63]. . . . .	53
7.4	Barr Modification matrix in MCEq . . . . .	55
7.5	Estimation of $\nu_\mu$ and $\bar{\nu}_\mu$ flux from four different hadronic interaction models compared to applying all Barr uncertainties . . . . .	56
7.6	Estimation of $\nu_\mu$ and $\bar{\nu}_\mu$ flux from four different cosmic ray models compared to shifting the spectral index . . . . .	57
7.7	The percentage contribution of each source of uncertainty on the $\nu_\mu$ (left) and $\bar{\nu}_\mu$ (right) flux as a function of neutrino energy . . . . .	59
7.8	Cancellation of uncertainty in flux ratios: The individual uncertainty on $\nu_\mu$ and $\bar{\nu}_\mu$ and the uncertainty on $\nu_\mu/\bar{\nu}_\mu$ ratio. Reproduction of results from Figure 6 of [63] . . . . .	60
7.9	The uncertainty in % on the $\nu_\mu/\bar{\nu}_\mu$ flux (black), $\nu_e/\bar{\nu}_e$ flux (red), and $(\nu_\mu + \bar{\nu}_\mu)/(\nu_e + \bar{\nu}_e)$ flux (green). Reproduction of results from Figure 7 of [63] . . . . .	61
7.10	Breakdown of uncertainties in flavor ratios for (top) $\nu_\mu/\bar{\nu}_\mu$ (middle) $\nu_e/\bar{\nu}_e$ (bottom) $(\nu_\mu + \bar{\nu}_\mu)/(\nu_e + \bar{\nu}_e)$ . . . . .	62
7.11	Uncertainties in directional ratios as a function of neutrino energy. Reproduction of results from Figure 9 of [63] . . . . .	63
8.1	Illustration of the staged approach in PISA. From [66] . . . . .	66
8.2	Nominal $\nu_\mu$ (left column) and $\bar{\nu}_\mu$ (right column) flux as calculated with the MCEq PISA stage and the Honda stage in 2D . . . . .	67
8.3	Nominal $\nu_\mu$ (upper) and $\bar{\nu}_\mu$ flux as calculated with the MCEq PISA stage and the Honda stage in 1D . . . . .	68

8.4	All flux nuisance parameters shifted by $+1\sigma$ in MCEq and Honda PISA stage, 2D . . . . .	70
8.5	Barr modified flux has a linear dependency on the magnitude of the modification . . . . .	71
8.6	All nusaince parameters in the MCEq stage added in quadrature to make a $1\sigma$ uncertainty band in 1D, shows that the Honda flux is within $\sim 1\sigma$ of the nominal MCEq flux . . . . .	72
8.7	The relative impact from each systematic uncertainty on the final $1\sigma$ confidence interval width in the $\nu_\tau$ apperance analysis. From [30].	75
8.8	Result from likelihood analysis for the tau neutrino appearance analysis with the Honda and MCEq stage. . . . .	76
D.1	The percentage contribution of each source of uncertainty on the $\nu_e$ (left) and $\bar{\nu}_e$ (right) flux as a function of neutrino energy . . . . .	93
D.2	Estimation of $\nu_e$ and $\bar{\nu}_e$ flux from four different hadronic interaction models compared to applying all Barr uncertainties . . . . .	94
D.3	Estimation of $\nu_e$ and $\bar{\nu}_e$ flux from four different cosmic ray models compared to shifting the spectral index . . . . .	94
D.4	Nominal $\nu_e$ (left column) and $\bar{\nu}_e$ (right column) flux as calculated with the MCEq PISA stage and the Honda stage in 2D . . . . .	95
D.5	Nominal $\nu_e$ (upper) and $\bar{\nu}_e$ flux as calculated with the MCEq PISA stage and the Honda stage in 1D . . . . .	96
D.6	All nusaince parameters in the MCEq stage added in quadrature to make a $1\sigma$ uncertainty band in 1D on the $\nu_e$ and $\bar{\nu}_e$ flux . . . . .	96
D.7	All flux nuisance parameters on the $\nu_e$ (left column) and $\bar{\nu}_e$ flux (right column) shifted by $+1\sigma$ in MCEq and Honda PISA stage, 2D . . . . .	97
E.1	Breakdown of uncertainties in up/horizontal ratio . . . . .	98
F.1	Best-fit values for all flux nuisance parameters for $0 < N_{\nu_\tau} < 2$ . . . . .	100

## List of Tables

0.1	Relationship between S.I. and natural units . . . . .	v
8.1	Nuisance parameters of the Honda and MCEq PISA stage . . . . .	69
B.1	Hadronic interaction models incorporated in MCEq. From [1]. . . . .	89
B.2	Models for the density of the Earth's atmosphere, implemented in MCEq. From [1]. . . . .	89
B.3	Models of the cosmic ray flux incorporated in MCEq. From [1]. . . . .	90

# List of Abbreviations

**ATWD** Analogue Transient Waveform Digitiser. 13

**CC** Charged current interaction is the exchange of a  $W^\pm$  boson. 9

**D-Egg** Dual optical sensors in an Ellipsoid Glass for Gen2, new optical sensor to be deployed in the IceCube upgrade. 18

**DIS** Deep Inelastic Scattering, a neutrino-nucleon interaction where the nucleon breaks up and hadronize 2.5. 9

**DOM** Digital Optical Module, the fundamental detector unit of IceCube consists of a PMT and specific electronics 3.3. 12, 81

**fADC** Fast Analogue-to-Digital Converter. 13

**LED** Light Emitting Diode, an electronic device that emits light when an electrical current is passed through it. 12

**LEP** Large Electron-Positron Collider was an lepton accelerator that run from 1989 to 2000, in the present day LHC tunnell at CERN. 5

**LHC** Large Hadron Collider is a particle accelerator located at CERN outside Geneva. 40

**MC** Monte Carlo is a broad class of computational algorithms to create a random data sample. 33

**MCEq** Matrix Cascade Equation is a software tool to analytically solve the cascade equation in matrix form. iv, 33

**mDOM** Multi-PMT Digital Optical Module, new optical sensor to be deployed in the IceCube upgrade. 18

**NC** Neutral current interaction is the exchange of a  $Z$  boson. 9

**PDF** Parton Distribution Function is the probability density of finding a particle with a momentum fraction  $x$  at a resuolution scale  $Q^2$ .. 50

**PISA** **PINGU Simulation & Analysis** is an analysis framework used within the IceCube collaboration. iv, 82

**PMNS** Pontecorvo–Maki–Nakagawa–Sakata matrix is a unitary mixing matrix containing information on how the neutrino mass eigenstates propagate. 6, 75

**PMT** **Photomultiplier Tube** is a photoemissive device in which the absorption of a photon results in the emission of an electron, which is amplified. 12, 84

**QCD** **Quantum Chromodynamics** is the quantum field theory of the strong interaction. 3

**QED** **Quantum Electrodynamics** is the relativistic quantum field theory of electrodynamic interaction. 3, 4

**SK** **Super-Kamiokande** is a water Cherenkov neutrino detector in Japan. 1



# Appendices

# Derivation of Oscillation Probability

Starting from equation (2.9):

$$P_{\nu_\alpha \rightarrow \nu_\beta}(L, E) = \sum_{k,j} U_{\alpha k}^* U_{\beta k} U_{\alpha j} U_{\beta j}^* \exp\left(-i \frac{\Delta m_{kj}^2 L}{2E}\right) \quad (\text{A.1})$$

$$= \sum_k U_{\alpha k}^* U_{\beta k} U_{\alpha k} U_{\beta k}^* + \sum_{k \neq j} U_{\alpha k}^* U_{\beta k} U_{\alpha j} U_{\beta j}^* \exp\left(-i \frac{\Delta m_{kj}^2 L}{2E}\right). \quad (\text{A.2})$$

We can derive the following identity

$$e^{iA} = \cos A + i \sin A \quad (\text{A.3})$$

$$= 1 - 2 \sin^2 \frac{A}{2} + i \sin A. \quad (\text{A.4})$$

As  $\Delta m_{kj}^2 = -\Delta m_{jk}^2$ , we can assign  $A = \Delta m_{jk}^2 \frac{L}{2E}$  and rewrite equation(A.2) as

$$P_{\nu_\alpha \rightarrow \nu_\beta}(L, E) = \sum_k U_{\alpha k}^* U_{\beta k} U_{\alpha k} U_{\beta k}^* \quad (\text{A.5})$$

$$+ \sum_{k \neq j} U_{\alpha k}^* U_{\beta k} U_{\alpha j} U_{\beta j}^* \quad (\text{A.6})$$

$$- 2 \sum_{k \neq j} U_{\alpha k}^* U_{\beta k} U_{\alpha j} U_{\beta j}^* \sin^2 \left( \Delta m_{jk}^2 \frac{L}{4E} \right) \quad (\text{A.7})$$

$$+ i \sum_{k \neq j} U_{\alpha k}^* U_{\beta k} U_{\alpha j} U_{\beta j}^* \sin \left( \Delta m_{jk}^2 \frac{L}{2E} \right). \quad (\text{A.8})$$

Expanding term (A.7) we get

$$\sum_{k \neq j} U_{\alpha k}^* U_{\beta k} U_{\alpha j} U_{\beta j}^* \sin^2 \left( \Delta m_{jk}^2 \frac{L}{4E} \right) \quad (\text{A.9})$$

$$= \sum_{k > j} U_{\alpha k}^* U_{\beta k} U_{\alpha j} U_{\beta j}^* \sin^2 \left( \Delta m_{kj}^2 \frac{L}{4E} \right) + \sum_{k < j} U_{\alpha k}^* U_{\beta k} U_{\alpha j} U_{\beta j}^* \sin^2 \left( \Delta m_{kj}^2 \frac{L}{4E} \right) \quad (\text{A.10})$$

$$= \sum_{k > j} U_{\alpha k}^* U_{\beta k} U_{\alpha j} U_{\beta j}^* \sin^2 \left( \Delta m_{kj}^2 \frac{L}{4E} \right) + \sum_{k > j} U_{\alpha j}^* U_{\beta j} U_{\alpha k} U_{\beta k}^* \sin^2 \left( \Delta m_{kj}^2 \frac{L}{4E} \right) \quad (\text{A.11})$$

$$= \sum_{k > j} \sin^2 \left( \Delta m_{kj}^2 \frac{L}{4E} \right) (U_{\alpha k}^* U_{\beta k} U_{\alpha j} U_{\beta j}^* + U_{\alpha j}^* U_{\beta j} U_{\alpha k} U_{\beta k}^*) \quad (\text{A.12})$$

$$= \sum_{k > j} \sin^2 \left( \Delta m_{kj}^2 \frac{L}{4E} \right) (U_{\alpha k}^* U_{\beta k} U_{\alpha j} U_{\beta j}^* + U_{\alpha k} U_{\beta k}^* U_{\alpha j}^* U_{\beta j}) \quad (\text{A.13})$$

$$= \sum_{k > j} \sin^2 \left( \Delta m_{kj}^2 \frac{L}{4E} \right) (U_{\alpha k}^* U_{\beta k} U_{\alpha j} U_{\beta j}^* + (U_{\alpha k}^* U_{\beta k} U_{\alpha j} U_{\beta j}^*)^*) \quad (\text{A.14})$$

$$= 2 \sum_{k > j} \text{Re}(U_{\alpha k}^* U_{\beta k} U_{\alpha j} U_{\beta j}^*) \sin^2 \left( \Delta m_{kj}^2 \frac{L}{4E} \right), \quad (\text{A.15})$$

where  $\text{Re}(A)$  is the real part of a complex number  $A$ . We can interchange the indices in equation (A.10) without changing signs as  $\sin^2$  is an even function. A similar exercise for term A.8 yields

$$\sum_{k \neq j} U_{\alpha k}^* U_{\beta k} U_{\alpha j} U_{\beta j}^* \sin \left( \Delta m_{jk}^2 \frac{L}{2E} \right) \quad (\text{A.16})$$

$$= 2i \sum_{k > j} \text{Im}(U_{\alpha k}^* U_{\beta k} U_{\alpha j} U_{\beta j}^*) \sin \left( \Delta m_{kj}^2 \frac{L}{2E} \right). \quad (\text{A.17})$$

where  $\text{Im}(A)$  is the imaginary part of a complex number  $A$ . The sign is reversed as  $\sin$  is an odd function.

As term (A.5) plus term (A.6) equals

$$\sum_k U_{\alpha k}^* U_{\beta k} U_{\alpha k} U_{\beta k}^* + \sum_{k \neq j} U_{\alpha k}^* U_{\beta k} U_{\alpha j} U_{\beta j}^* \quad (\text{A.18})$$

$$= \sum_i \sum_j U_{\alpha k}^* U_{\beta k} U_{\alpha j} U_{\beta j}^* \quad (\text{A.19})$$

$$= \sum_k (U_{\alpha k}^* U_{\beta k}) \sum_j (U_{\alpha j} U_{\beta j}^*) \quad (\text{A.20})$$

As  $U$  is unitary  $\sum_k U_{\alpha k} U_{\beta k}^* = \delta_{\alpha\beta}$ , where  $\delta$  is the Kronecker delta function. This means that the (A.5) + (A.6) =  $\delta_{\alpha\beta}$ .

Putting all terms together we find

$$P_{\nu_\alpha \rightarrow \nu_\beta}(L, E) = \delta_{\alpha\beta} - 4 \sum_{k>j} \text{Re}(U_{\alpha k}^* U_{\beta k} U_{\alpha j} U_{\beta j}^*) \sin^2 \left( \Delta m_{kj}^2 \frac{L}{4E} \right) \quad (\text{A.21})$$

$$+ 2 \sum_{k>j} \text{Im}(U_{\alpha k}^* U_{\beta k} U_{\alpha j} U_{\beta j}^*) \sin \left( \Delta m_{kj}^2 \frac{L}{2E} \right) \quad (\text{A.22})$$

## B.1 Hadronic Interaction Models in MCEq

**Table B.1.** – Hadronic interaction models representations in MCEq for proton-air simulations. The (pp) version is for a hydrogen target. Copied from [1].

Name	Reference
SIBYLL 2.1	[75]
SIBYLL 2.3	[76]
SIBYLL 2.3c	[53]
SIBYLL 2.3c (pp)	[53]
QGSJET 01-c, II-03, II-04	[51]
EPOS LHC	[52]
DPMJET-III	[54]
DPMJET-III 2017	[64]

## B.2 Density Profile of the Atmosphere

The isothermal model is

$$\rho(a) = \frac{X_0}{a_{iso}} e^{-\frac{a}{a_{iso}}} \quad (\text{B.1})$$

where  $X_0$  and  $a_{iso}$  are chosen to resemble a good approximation of the density at relevant altitudes  $a$  for neutrino production.

**Table B.2.** – Table of models for the density of the Earth’s atmosphere, incorporated in MCEq. Copied from [1].

Name	Reference	Description
Isothermal	[77]	According to eq. (B.1) with $X_0 = 1300\text{g/cm}^2$ and $a_{iso} = 6.3\text{ km}$
CORSIKA	[49]	Piece-wise fit of 5 exponentials to other models or data.
NRLMSISE-00	[50]	Global numerical static atmospheric model.
Tabulated atmosphere		Template class for tabulated atmospheres, which can be extrapolated at high altitudes with NRLMSISE-00
GeneralizedTarget		A piece-wise defined homogeneous target density (for general purpose calculations of cascades)

## B.3 Cosmic Ray Models

The most relevant cosmic ray flux models implemented in MCEq are described below. Other models, such as poly-gonato[78] or Zatsepin-Sokolskaya[79] are also implemented, but describe new data worse than the four models mentioned below [42].

**H3a** [44] Based on a proposal of Hillas, the model assumes three populations of cosmic rays. The first population is associated with the acceleration of supernova remnants, with the «knee» signaling the cut-off. The second population is a higher-energy galactic component of unknown origin, while the highest energy population is assumed to be of extragalactic origin. All three components contain

five groups of nuclei and cut off exponentially at a characteristic rigidity  $R_{c,j}$ , as suggested by B. Peters. The all-particle spectrum is given by

$$\phi_i(E) = \sum_{j=1}^3 a_{i,j} E^{\gamma_{i,j}} \times \exp\left[-\frac{E}{Z_i R_{c,j}}\right], \quad (\text{B.2})$$

where the subscript  $i$  runs over the standard five groups (p, He, CNO, Mg-Si and Fe) and  $a$  is a normalization constant. The parameters are adjusted to CREAM data at lower energies, and the majority of high energy observations. An alternative version, H4a, contains only protons in the third population.

**GST-3/GST-4** [45] The *Gaisser-Stanev-Tilav* model is building on many of the same considerations as H3a, assuming three populations and five groups. The spectrum is fitted, rather than adjusted, to data using equation (B.2). The fit is restricted to certain rigidity cut-offs for each group, in order to reproduce features like the «second knee» as reported by KASCADE [80]. GST-4 is an alternative version with four generations and only protons above the «knee».

**GH** [46] The *Gaisser-Honda* model, is somewhat older (2002). The primary flux is assumed to follow

$$\phi(E_h) = K \times (E_k + b \exp[-c\sqrt{E_h}])^{-\alpha}, \quad (\text{B.3})$$

and is fitted to balloon measurements (AMS and BESS). Thus it is developed for data below the PeV scale and does not aim to model the high energy features as the «knee» and «ankle» [42].

**Table B.3.** – Table of models included in the sub-module CRFluxModels in MCEq. Copied from [1].

Short name	Reference	Description	Valid range [GeV]
H3a	[44]	three astrophysical populations, broken power laws, five mass groups, heavier composition at ultra-high energies (UHE)	$10^3 - 10^{11}$ GeV
H4a	[44]	same as H3a but with proton composition at UHE	$10^3 - 10^{11}$ GeV
GST-3	[45]	three population, broken power-law fit heavier composition between «knee» and «ankle» («second knee»)	$10^3 - 10^{11}$ GeV
GST-4	[45]	like GST-3 but with an fourth extragalactic proton component at UHE	$10^3 - 10^{11}$ GeV
GH	[46]	power-law model with five mass groups, often used in atmospheric neutrino flux calculations below «knee» energies	<PeV
cHGp	[44] [46] [81]	combination of GH at low energy and H4a above	tens – $10^{11}$ GeV
cHGm	[44] [46] [81]	like cHGp but with H3a instead of H4a	tens – $10^{11}$ GeV
Polygonato	[78]	broken power-law fit, based on renormalization of various cosmic ray measurements up to «knee» energies	few TeV – PeV
ZS	[79]	original model by Zatsepin and Sokolskaya, also including re-fitted parameters by the PAMELA collaboration	tens GeV – PeV
TIG		simple broken power law spectrum of nucleons (protons)	TeV – PeV
GSF	[65]	Global Spline Fit to recent cosmic ray observations with errors	10 GeV – $10^{12}$ GeV

## C.1 Diffractive Cross Sections

We can include diffractive excitation by introducing fluctuations in the individual nucleon-nucleon interaction<sup>1</sup>. We can do this by assuming that the mass eigenstate of the nucleon  $\Psi_i$ , differs from the elastic scattering eigenstate  $\Phi_l$  with corresponding eigenvalues  $T_k$ . The mass eigenstates are linear combinations of the elastic eigenstates:  $\Psi = \sum_i a_{ij} \Phi_l$ .

The transition amplitude going from an initial state to the  $i$ 'th state is

$$\langle \Psi_i | T | \Psi_0 \rangle = \sum_k a_{ik} T_k a_{0k}. \quad (\text{C.1})$$

An elastic process corresponds to no change in mass state, and thus the elastic cross-section at a fixed  $\mathbf{b}$  is

$$\frac{d\sigma_{el}}{d^2b} = \langle \Psi_0 | T | \Psi_0 \rangle^2 = \langle T(\mathbf{b}) \rangle^2. \quad (\text{C.2})$$

The total diffractive scattering at fixed  $\mathbf{b}$  (including the elastic) is the transition to all states  $\Psi_i$ , so that

$$\frac{\sigma_{\text{diff}}}{d^2b} = \sum_i \langle \Psi_0 | T | \Psi_i \rangle \langle \Psi_i | T | \Psi_0 \rangle = \langle T^2(\mathbf{b}) \rangle. \quad (\text{C.3})$$

Consequently the cross section for diffractive excitations given by the fluctuations is

$$\frac{d\sigma_D}{d^2b} = \frac{d\sigma_{\text{diff}}}{d^2b} - \frac{d\sigma_{el}}{d^2b} = \langle T^2(\mathbf{b}) \rangle - \langle T(\mathbf{b}) \rangle^2. \quad (\text{C.4})$$

Both target and projectile can fluctuate. For an elastic process we can average over all states. In a single diffractive process, where e.g. the projectile is excited, we can average over the target states. Finally we can find the cross section for a double diffractive process by subtracting the cross section of the single diffractive processes ( $Dt$  and  $pD$ ) from the total diffractive cross section of equation (C.4). The result is

<sup>1</sup>This approach is called the Good-Walker formalism [82]

$$d\sigma_{\text{tot}}/d^2b = \langle 2T(\mathbf{b}) \rangle_{proj,t}, \quad (\text{C.5})$$

$$d\sigma_{\text{abs}}/d^2b = \langle 2T(\mathbf{b}) - T^2(\mathbf{b}) \rangle_{proj,t}, \quad (\text{C.6})$$

$$d\sigma_{\text{el}}/d^2b = \langle T(\mathbf{b}) \rangle_{proj,t}^2, \quad (\text{C.7})$$

$$d\sigma_{Dt}/d^2b = \langle \langle T(\mathbf{b}) \rangle_{proj}^2 \rangle_t - \langle T(\mathbf{b}) \rangle_{proj,t}^2, \quad (\text{C.8})$$

$$d\sigma_{pD}/d^2b = \langle \langle T(\mathbf{b}) \rangle_t^2 \rangle_{proj} - \langle T(\mathbf{b}) \rangle_{proj,t}^2, \quad (\text{C.9})$$

$$d\sigma_{DD}/d^2b = \langle T^2(\mathbf{b}) \rangle_{proj,t} - \langle \langle T(\mathbf{b}) \rangle_{proj}^2 \rangle_t - \langle \langle T(\mathbf{b}) \rangle_t^2 \rangle_{proj} + \langle T(\mathbf{b}) \rangle_{proj,t}^2, \quad (\text{C.10})$$

where *proj* and *t* denotes averages over the projectile and target state, respectively.

## C.2 Distribution of T

In [57] it is shown that  $T(b)$  can be assumed to follow the distribution:

$$T(b) = T_0(r_p + r_t) \Theta \left( \sqrt{\frac{(r_p + r_t)^2}{2T_0}} - b \right), \quad (\text{C.11})$$

where  $T_0$  is an opacity parameter  $T_0 \leq 1$ .

We have seen that introducing diffractive excitation in the form of a fluctuation modifies the cross sections. This corresponds to fluctuating the internal structure of the nucleus, i.e., we must allow  $r_p$  and  $r_t$  to fluctuate according to some distribution, found in [83][57]

$$P(r) = \frac{r^{k-1} e^{-r/r_0}}{\Gamma(k) r_0^k}, \quad (\text{C.12})$$

$k$  being a shape parameter and  $r_0$  setting the position of the distribution. The function  $\Gamma(k)$  is  $\Gamma(k) = (k-1)!$  evaluated at  $k$ . The opacity has an exponential shape, so that:

$$T_0(r_p + r_t) = 1 - \exp \left( -\pi(r_p + r_t)^2 / \sigma_t \right) \quad (\text{C.13})$$

giving three free parameters:  $\sigma_t, r_0, k$ .

## Results on the Atmospheric Electron Neutrino Flux

In Chapter 7 and Chapter 8 most results are shown for  $\nu_\mu$  and  $\bar{\nu}_\mu$  flux. In this Appendix results are repeated for the  $\nu_e$  and  $\bar{\nu}_e$  flux.

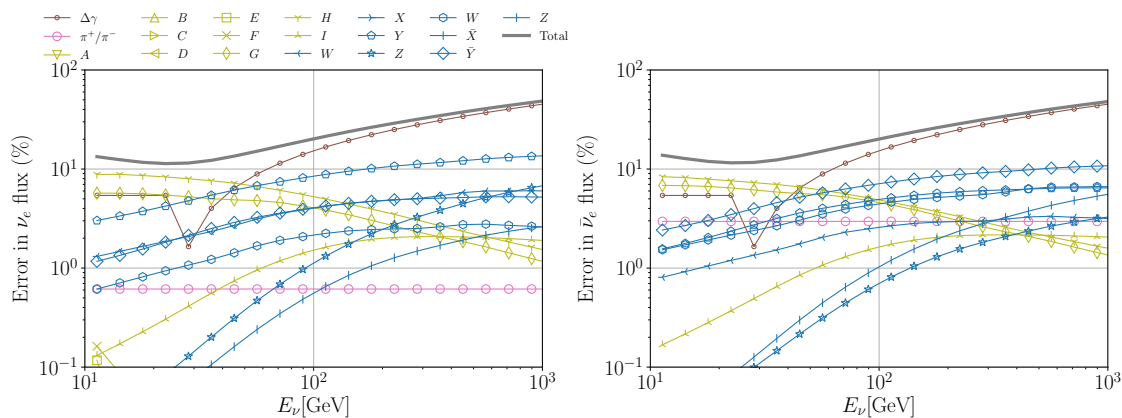


**Figure D.1.** – Breakdown of the uncertainties (averaged over zenith angles) on the  $\nu_e$  (left) and  $\bar{\nu}_e$  (right) flux, with different regions of meson production as a function of neutrino energy. The capital letters correspond to the Barr variables of diagram 7.3. Green curves are uncertainty stemming from pion production, blue from kaon production. The uncertainty on the pion ratio is represented by  $\pi^+/\pi^-$  (pink). The brown curve represents the uncertainty arising from the spectral index of the cosmic ray spectrum. The topmost, gray line is the total uncertainty on the flux. The estimate by Barr et al. is plotted in gray, dashed line for comparison [63]

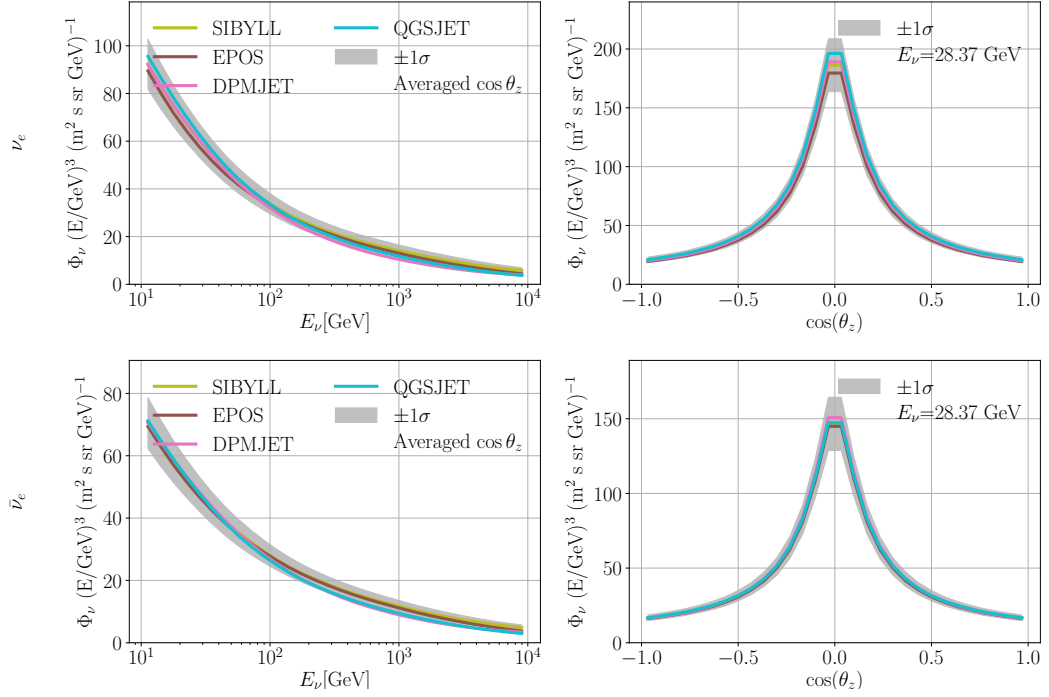


**Figure D.2.** – The nominal  $\nu_e$  (upper) and  $\bar{\nu}_e$  (lower) flux as calculated with four different hadronic interaction models. The gray band indicate all uncertainties on particle production, i.e., all Barr variables, shifted by  $\pm 1\sigma$  as compared to the SIBYLL2.3c flux and added in quadrature.

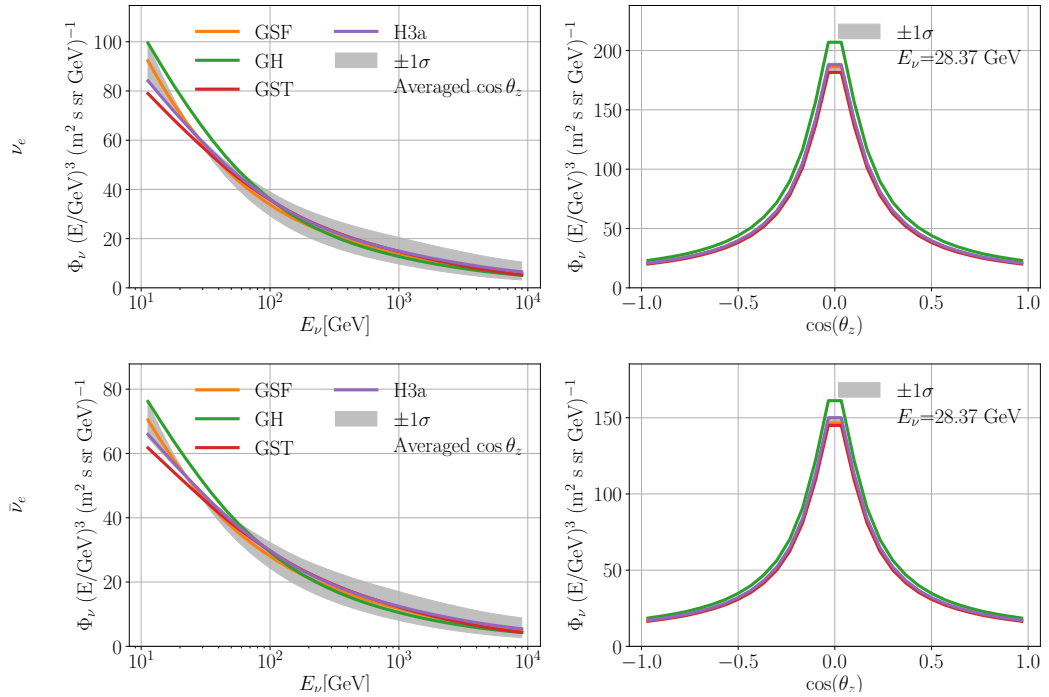


**Figure D.3.** – The nominal  $\nu_e$  (upper) and  $\bar{\nu}_e$  (lower) flux as calculated with four different cosmic ray models. The gray band indicates the result of shifting the spectral index with  $\pm 1\sigma = 0.1$ , assuming that the nominal flux is that calculated with GSF.

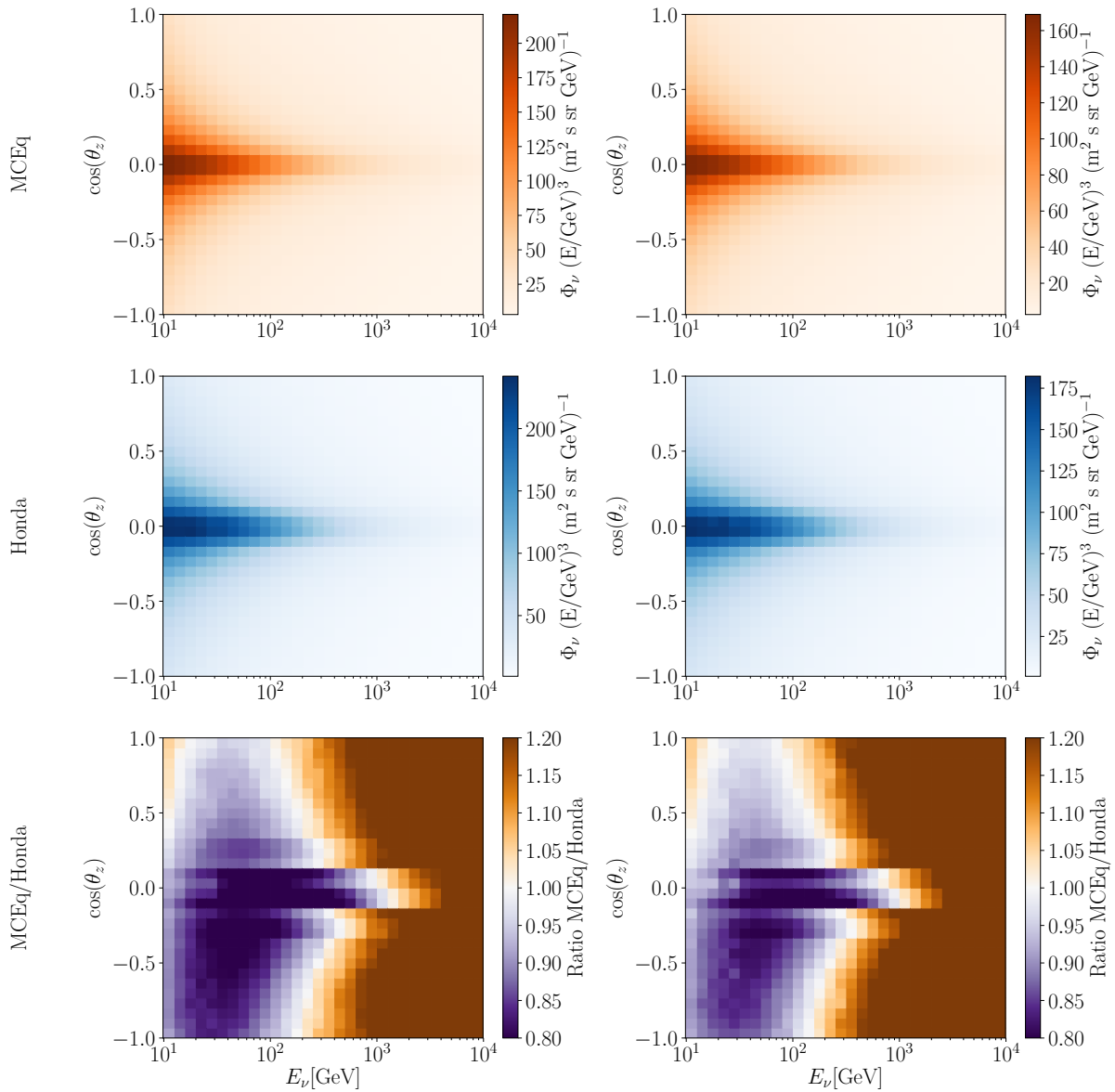


**Figure D.4.** – The nominal  $\nu_e$  (left column) and  $\bar{\nu}_e$  (right column) flux as calculated with the MCEq PISA stage (topmost, orange row) and the Honda stage (middle, blue row). The ratio of the two is shown in lower row.

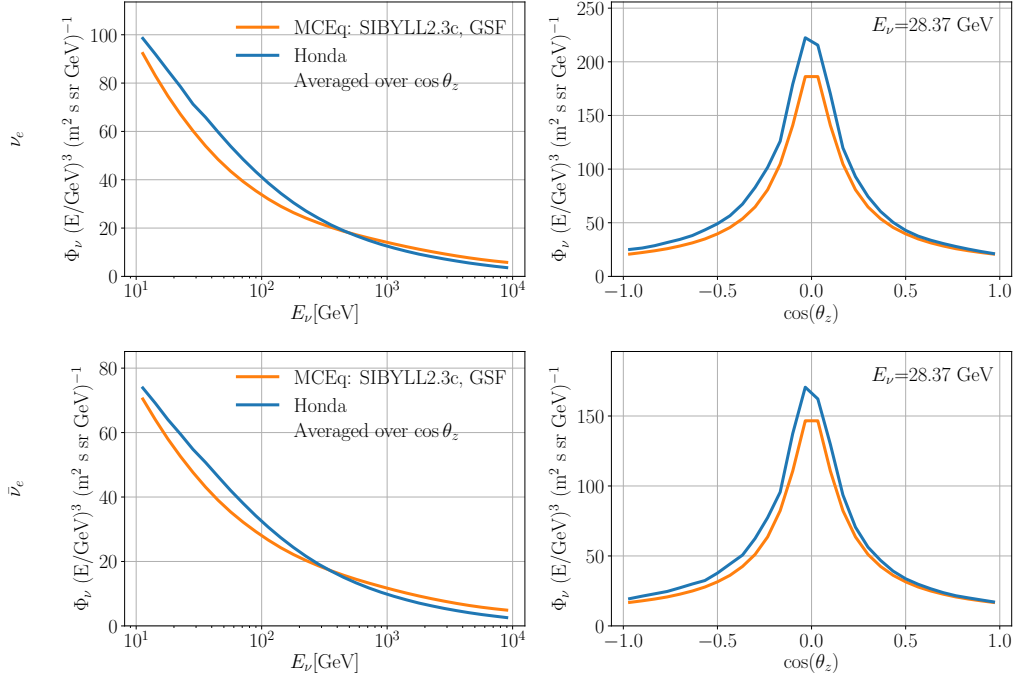


**Figure D.5.** – The nominal  $\nu_e$  (upper) and  $\bar{\nu}_e$  flux as calculated with the MCEq PISA stage (orange) and the Honda PISA stage (blue)

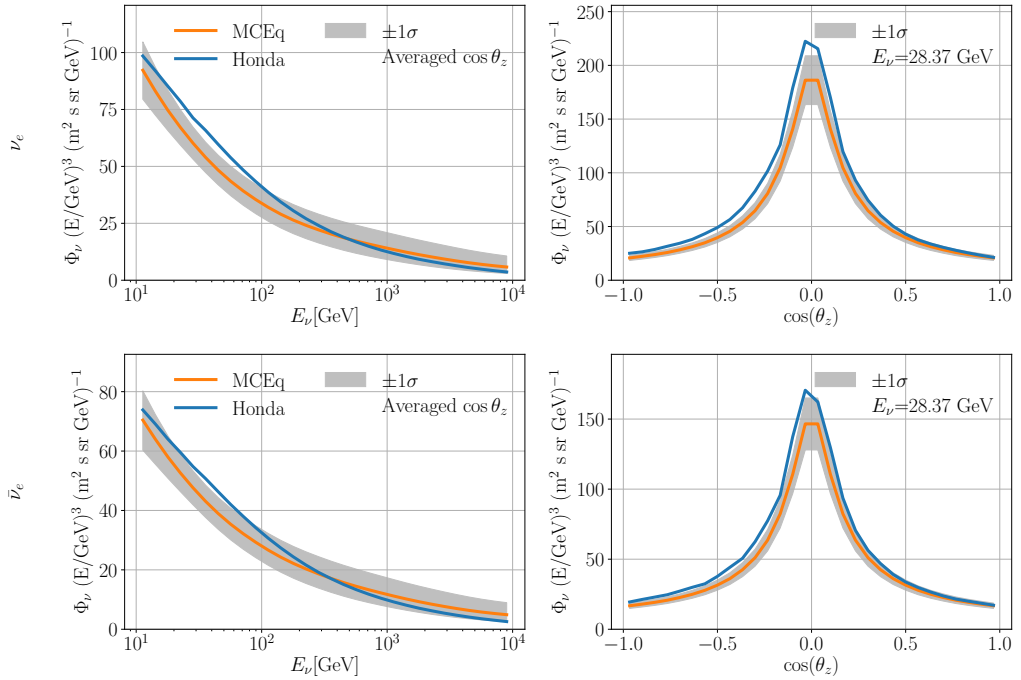


**Figure D.6.** – The nominal  $\nu_\mu$  (upper) and  $\bar{\nu}_\mu$  (lower) flux as calculated with MCEq (orange) and Honda (blue stage). All nuisance parameters in the MCEq stage shifted by  $\pm 1\sigma$  and added in quadrature to make up the grey  $1\sigma$  band.

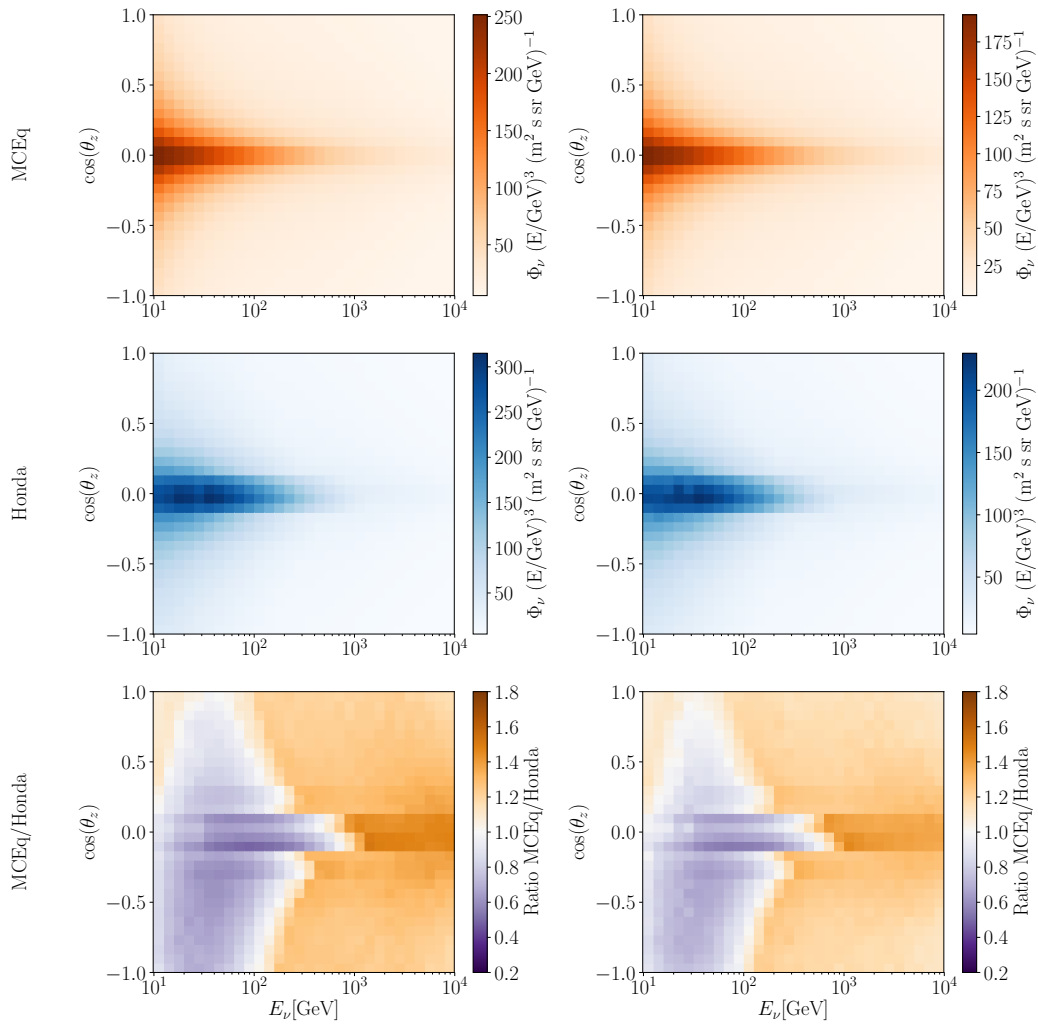


**Figure D.7.** – All flux nuisance parameters shifted by  $+1\sigma$  and added in quadrature as calculated in the MCEq stage (topmost, orange) and in the Honda stage (middle, blue). The ratio between the systematic fluxes are plotted in the lowermost row.

# Breakdown of Uncertainties on Neutrino Ratios

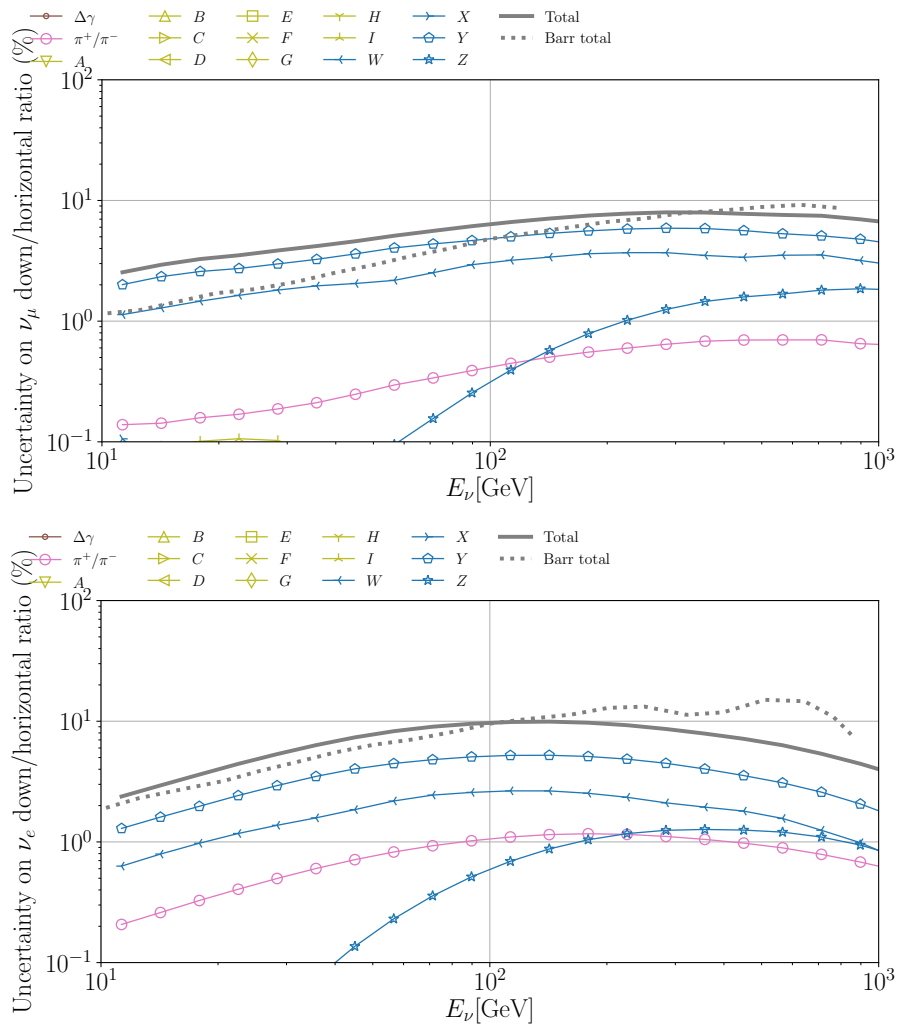


**Figure E.1.** – Breakdown of uncertainties in up/horizontal ratio. (1)  $\nu_\mu + \bar{\nu}_\mu$  and (2)  $\nu_e + \bar{\nu}_e$

# Atmospheric Flux Nuisance Parameters

F

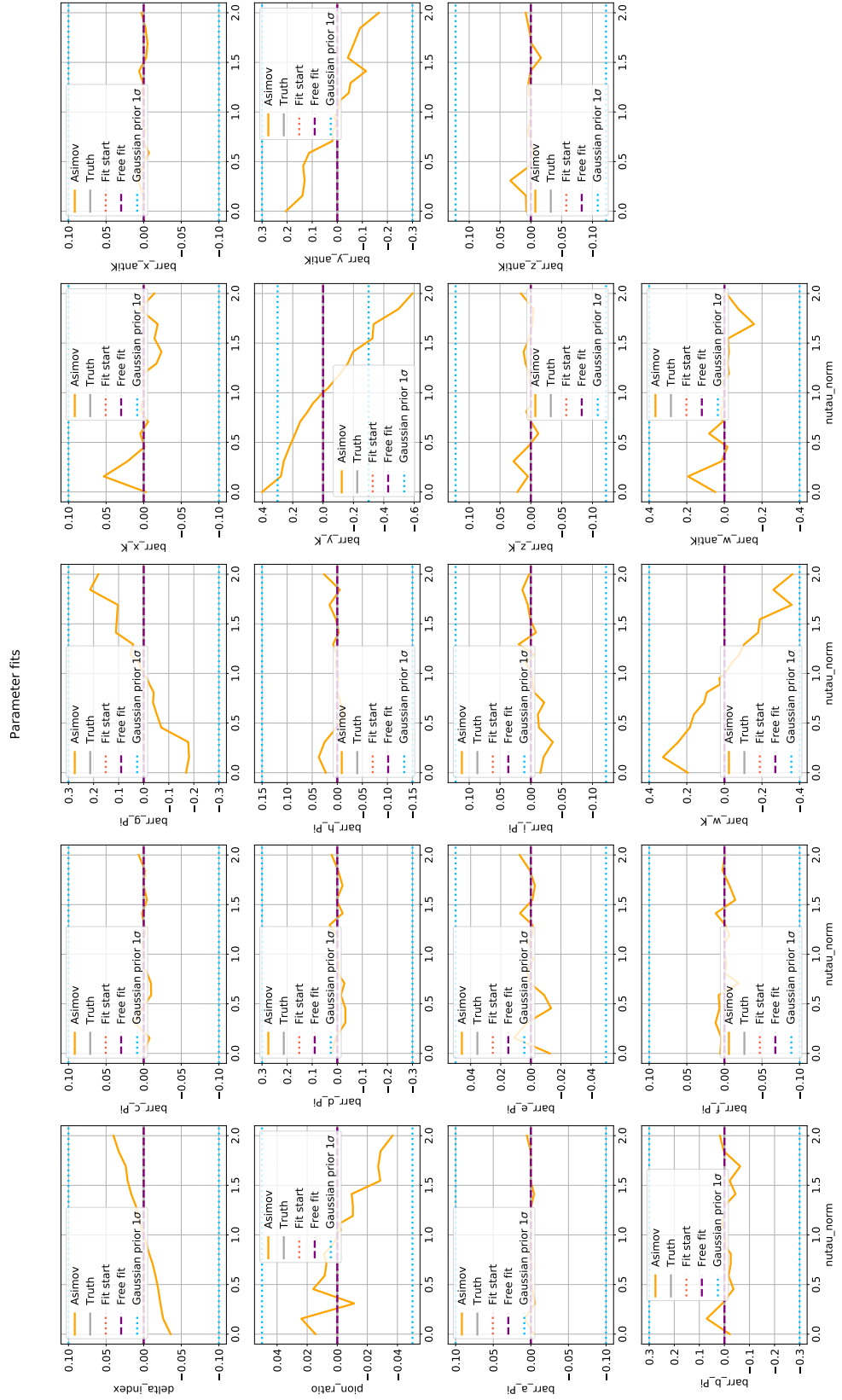


Figure F.1. – Best-fit values for all flux nuisance parameters for  $0 < N_{\nu_\tau} < 2$ .

# Bibliography

- [1] Anatoli Fedynitch, Ralph Engel, Thomas K. Gaisser, Felix Riehn, and Todor Stanev. “Calculation of Conventional and Prompt Lepton Fluxes at Very High Energy”. In: *EPJ Web Conf.* 99 (2015), p. 08001 (cit. on pp. iv, 30–32, 34, 37, 89, 90).
- [2] F. Hoyle. “Concluding Remarks”. In: *Proceedings of the Royal Society of London A : Mathematical, Physical and Engineering Sciences*. Vol. 301. 1967, p. 171 (cit. on p. 1).
- [3] W. Pauli. “Pauli letter collection: letter to Lise Meitner”. Typed copy. 1930 (cit. on p. 1).
- [4] J. Chadwick. “Intensitätsverteilung im magnetischen spektrum der betastrahlen von radium B+C ”. In: *Verhandlungen der deutschen Physikalischen Gesellschaft* 16 (1914) (cit. on p. 1).
- [5] C. L. Cowan, F. Reines, F. B. Harrison, H. W. Kruse, and A. D. McGuire. “Detection of the Free Neutrino: a Confirmation”. In: *Science* 124.3212 (1956), pp. 103–104 (cit. on p. 1).
- [6] G. Danby, J-M. Gaillard, K. Goulianos, et al. “Observation of High-Energy Neutrino Reactions and the Existence of Two Kinds of Neutrinos”. In: *Phys. Rev. Lett.* 9 (1 1962), pp. 36–44 (cit. on p. 1).
- [7] K. Kodama et al. “Observation of tau neutrino interactions”. In: *Phys. Lett.* B504 (2001), pp. 218–224 (cit. on p. 1).
- [8] J. N. Bahcall. *Neutrino astrophysics*. 1989 (cit. on p. 1).
- [9] B. T. Cleveland, Timothy Daily, Raymond Davis Jr., et al. “Measurement of the solar electron neutrino flux with the Homestake chlorine detector”. In: *Astrophys. J.* 496 (1998), pp. 505–526 (cit. on p. 1).
- [10] Q. R. Ahmad et al. “Measurement of the rate of  $\nu_e + d \rightarrow p + p + e^-$  interactions produced by  $^8B$  solar neutrinos at the Sudbury Neutrino Observatory”. In: *Phys. Rev. Lett.* 87 (2001), p. 071301 (cit. on p. 1).
- [11] Takaaki Kajita. “Atmospheric neutrino results from Super-Kamiokande and Kamiokande – Evidence for tau neutrino oscillations”. In: *Nuclear Physics B - Proceedings Supplements* 77.1 (1999), pp. 123–132 (cit. on p. 1).
- [12] The United States at the LHC. *The Standard Model and beyond*. URL: <http://united-states.cern/physics/standard-model-and-beyond> (visited on May 4, 2019) (cit. on p. 4).

- [13] G. 't Hooft and M. Veltman. “Regularization and renormalization of gauge fields”. In: *Nuclear Physics B* 44 (July 1972), pp. 189–213 (cit. on p. 5).
- [14] S. Schael et al. “Precision electroweak measurements on the  $Z$  resonance”. In: *Phys. Rept.* 427 (2006), pp. 257–454 (cit. on p. 5).
- [15] Z. Maki, M. Nakagawa, and S. Sakata. “Remarks on the Unified Model of Elementary Particles”. In: *Progress of Theoretical Physics* 28 (Nov. 1962), pp. 870–880 (cit. on p. 6).
- [16] Carlo Giunti and Chung W. Kim. *Fundamentals of Neutrino Physics and Astrophysics*. 2007 (cit. on p. 6).
- [17] M. et. al Tanabashi. “Review of Particle Physics”. In: *Phys. Rev. D* 98 (3 2018), p. 030001 (cit. on pp. 7, 8).
- [18] Mark Thomson. *Modern particle physics*. Cambridge: Cambridge University Press, 2013 (cit. on pp. 9, 11).
- [19] J. A. Formaggio and G. P. Zeller. “From eV to EeV: Neutrino Cross Sections Across Energy Scales”. In: *Rev. Mod. Phys.* 84 (2012), pp. 1307–1341 (cit. on p. 10).
- [20] M. G. Aartsen et al. “Evidence for High-Energy Extraterrestrial Neutrinos at the IceCube Detector”. In: *Science* 342 (2013), p. 1242856 (cit. on p. 11).
- [21] P. A. Cherenkov. “Visible luminescence of pure liquids under the influence of  $\gamma$ -radiation”. In: *Dokl. Akad. Nauk SSSR* 2.8 (1934), pp. 451–454 (cit. on p. 11).
- [22] M. G. Aartsen et al. “Measurement of South Pole ice transparency with the IceCube LED calibration system”. In: *Nucl. Instrum. Meth.* A711 (2013), pp. 73–89 (cit. on p. 12).
- [23] M. Ackermann, J. Ahrens, X. Bai, et al. “Optical properties of deep glacial ice at the South Pole”. In: *Journal of Geophysical Research: Atmospheres* 111.D13 (2006) (cit. on p. 12).
- [24] M. G. Aartsen et al. “The IceCube Neutrino Observatory: Instrumentation and Online Systems”. In: *JINST* 12.03 (2017), P03012 (cit. on pp. 12, 13).
- [25] Markus Ahlers, Klaus Helbing, and Carlos Pérez de los Heros. “Probing Particle Physics with IceCube”. In: *Eur. Phys. J.* C78.11 (2018), p. 924 (cit. on p. 14).
- [26] R. Abbasi et al. “The Design and Performance of IceCube DeepCore”. In: *Astropart. Phys.* 35 (2012), pp. 615–624 (cit. on p. 14).
- [27] Juan Pablo Yáñez Garza. “Measurement of neutrino oscillations in atmospheric neutrinos with the IceCube DeepCore detector”. PhD thesis. Humboldt-Universität zu Berlin, Mathematisch-Naturwissenschaftliche Fakultät, 2014 (cit. on p. 15).
- [28] C. Patrignani et al. “Review of Particle Physics”. In: *Chin. Phys.* C40.10 (2016), p. 100001 (cit. on p. 16).

- [29] S. Euler. “Observation of oscillations of atmospheric neutrinos with the IceCube Neutrino Observatory”. Ph.D. Rheinisch-Westfälische Technische Hochschule (RWTH), 2013 (cit. on p. 16).
- [30] M. G. Aartsen et al. “Measurement of Atmospheric Tau Neutrino Appearance with IceCube DeepCore”. In: *Phys. Rev. D* 99.3 (2019), p. 032007 (cit. on pp. 17, 18, 74, 75).
- [31] M. G. Aartsen et al. “The IceCube Neutrino Observatory Part V: Neutrino Oscillations and Supernova Searches”. In: *Proceedings, 33rd International Cosmic Ray Conference (ICRC2013): Rio de Janeiro, Brazil, July 2-9, 2013*. 2013 (cit. on p. 17).
- [32] Niels Bohr Institute. *A New Upgrade for the IceCube Detector*. URL: <https://www.nbi.ku.dk/english/news/news19/upgrade-of-a-research-icecube/> (cit. on p. 18).
- [33] The IceCube Collaboration. “The IceCube Upgrade - Design and Science Goals”. In: *36th International Cosmic Ray Conference*. Ed. by A. Ishihara. (Cit. on pp. 18, 19).
- [34] M. G. Aartsen et al. “IceCube-Gen2: A Vision for the Future of Neutrino Astronomy in Antarctica”. In: (2014) (cit. on p. 19).
- [35] J. Alcaraz, D. Alvisi, B. Alpat, et al. “Protons in near earth orbit”. In: *Physics Letters B* 472.1 (2000), pp. 215–226 (cit. on p. 20).
- [36] O. Adriani, G. C. Barbarino, G. A. Bazilevskaya, et al. “PAMELA Measurements of Cosmic-Ray Proton and Helium Spectra”. In: *Science* 332.6025 (2011), pp. 69–72 (cit. on p. 20).
- [37] A. D. Panov et al. “Energy Spectra of Abundant Nuclei of Primary Cosmic Rays from the Data of ATIC-2 Experiment: Final Results”. In: *Bull. Russ. Acad. Sci. Phys.* 73.5 (2009), pp. 564–567 (cit. on p. 20).
- [38] H. S. Ahn, P. Allison, M. G. Bagliesi, et al. “Energy Spectra of Cosmic-ray Nuclei at High Energies”. In: *The Astrophysical Journal* 707.1 (2009), pp. 593–603 (cit. on p. 20).
- [39] M. Ave, P. J. Boyle, F. Gahbauer, et al. “Composition of Primary Cosmic-Ray Nuclei at High Energies”. In: *Astrophys. J.* 678 (2008), p. 262 (cit. on p. 20).
- [40] Alexander Aab et al. “Combined fit of spectrum and composition data as measured by the Pierre Auger Observatory”. In: *JCAP* 1704.04 (2017), p. 038 (cit. on p. 20).
- [41] W. D. Apel et al. “KASCADE-Grande measurements of energy spectra for elemental groups of cosmic rays”. In: *Astropart. Phys.* 47 (2013), pp. 54–66 (cit. on p. 20).
- [42] Anatoli Fedynitch. “Cascade equations and hadronic interactions at very high energies”. PhD thesis. KIT, Karlsruhe, Dept. Phys., 2015-11-01 (cit. on pp. 21, 27, 89, 90).

- [43] B. Peters. “Primary cosmic radiation and extensive air showers”. In: *Il Nuovo Cimento (1955-1965)* 22.4 (1961), pp. 800–819 (cit. on p. 20).
- [44] Thomas K. Gaisser. “Spectrum of cosmic-ray nucleons, kaon production, and the atmospheric muon charge ratio”. In: *Astropart. Phys.* 35 (2012), pp. 801–806 (cit. on pp. 20, 58, 89, 90).
- [45] Thomas K. Gaisser, Todor Stanev, and Serap Tilav. “Cosmic Ray Energy Spectrum from Measurements of Air Showers”. In: *Front. Phys.(Beijing)* 8 (2013), pp. 748–758 (cit. on pp. 20, 58, 90).
- [46] T. K. Gaisser and M. Honda. “Flux of atmospheric neutrinos”. In: *Ann. Rev. Nucl. Part. Sci.* 52 (2002), pp. 153–199 (cit. on pp. 20, 28, 58, 66, 90).
- [47] R. Fedynitch A. and Engel. “MCEq - efficient computation of particle particle cascades in the atmosphere”. Unpublished. 2018 (cit. on p. 22).
- [48] M. Honda, M. Sajjad Athar, T. Kajita, K. Kasahara, and S. Midorikawa. “Atmospheric neutrino flux calculation using the NRLMSISE-00 atmospheric model”. In: *Phys. Rev. D* 92.2 (2015), p. 023004 (cit. on pp. 29, 32, 65, 66, 77).
- [49] D. Heck, J. Knapp, J. N. Capdevielle, G. Schatz, and T. Thouw. “CORSIKA: A Monte Carlo code to simulate extensive air showers”. In: *FZKA-6019* (1998) (cit. on pp. 30, 38, 89).
- [50] J. M. Picone, A. E. Hedin, D. P. Drob, and A. C. Aikin. “NRLMSISE-00 empirical model of the atmosphere: Statistical comparisons and scientific issues”. In: *Journal of Geophysical Research: Space Physics* 107.A12 (2002) (cit. on pp. 30, 38, 66, 89).
- [51] Sergey Ostapchenko. “Monte Carlo treatment of hadronic interactions in enhanced Pomeron scheme: I. QGSJET-II model”. In: *Phys. Rev. D* 83 (2011), p. 014018 (cit. on pp. 33, 56, 89).
- [52] T. Pierog, Iu. Karpenko, J. M. Katzy, E. Yatsenko, and K. Werner. “EPOS LHC: Test of collective hadronization with data measured at the CERN Large Hadron Collider”. In: *Phys. Rev. C* 92.3 (2015), p. 034906 (cit. on pp. 33, 56, 89).
- [53] Felix Riehn, Hans P. Dembinski, Ralph Engel, et al. “The hadronic interaction model SIBYLL 2.3c and Feynman scaling”. In: *PoS ICRC2017* (2018), p. 301 (cit. on pp. 33, 56, 89).
- [54] Stefan Roesler, Ralph Engel, and Johannes Ranft. “The Monte Carlo event generator DPMJET-III”. In: *Advanced Monte Carlo for radiation physics, particle transport simulation and applications. Proceedings, Conference, MC2000, Lisbon, Portugal, October 23-26, 2000.* 2000, pp. 1033–1038 (cit. on pp. 33, 66, 89).
- [55] A. D. Martin, M. G. Ryskin, and A. M. Stasto. “Prompt neutrinos from atmospheric  $c\bar{c}$  and  $b\bar{b}$  production and the gluon at very small  $x$ ”. In: *Acta Phys. Polon.* B34 (2003), pp. 3273–3304 (cit. on p. 38).

- [56] Torbjörn Sjöstrand, Stefan Ask, Jesper R. Christiansen, et al. “An Introduction to PYTHIA 8.2”. In: *Comput. Phys. Commun.* 191 (2015), pp. 159–177 (cit. on p. 39).
- [57] Christian Bierlich, Gösta Gustafson, Leif Lönnblad, and Harsh Shah. “The Angantyr model for Heavy-Ion Collisions in PYTHIA8”. In: *JHEP* 10 (2018), p. 134 (cit. on pp. 39, 42, 92).
- [58] V. N. Gribov. “Glauber corrections and the interaction between high-energy hadrons and nuclei”. In: *Sov. Phys. JETP* 29 (1969), pp. 483–487 (cit. on p. 41).
- [59] Gerhard A. Schuler and Torbjörn Sjöstrand. “Hadronic diffractive cross sections and the rise of the total cross section”. In: *Phys. Rev. D* 49 (5 1994), pp. 2257–2267 (cit. on p. 42).
- [60] C. Patrignani et al. “Review of Particle Physics”. In: *Chin. Phys.* C40.10 (2016) (cit. on pp. 42, 43).
- [61] M. Adamus et al. “Charged Particle Production in  $K^+p$ ,  $\pi^+p$  and  $pp$  Interactions at 250-GeV/c”. In: *Z. Phys.* C39 (1988), pp. 311–329 (cit. on pp. 44, 45).
- [62] EHS-NA22 Collaboration. “Multiplicity distribution in K+ Al and K+ Au collisions at 250 GeV/c and a test of the multiple collision model”. In: *Zeitschrift für Physik C Particles and Fields* 42.3 (1989), pp. 377–385 (cit. on p. 48).
- [63] G. D. Barr, T. K. Gaisser, S. Robbins, and Todor Stanev. “Uncertainties in Atmospheric Neutrino Fluxes”. In: *Phys. Rev.* D74 (2006), p. 094009 (cit. on pp. 50–53, 59–61, 63, 68, 77, 93).
- [64] A Fedynitch and R Engel. “Revision of the high energy hadronic interaction models PHOJET/DPMJET-III”. In: *14th International Conference on Nuclear Reaction Mechanisms* (2015) (cit. on pp. 56, 89).
- [65] Hans Dembinski, Ralph Engel, Anatoli Fedynitch, et al. “Data-driven model of the cosmic-ray flux and mass composition from 10 GeV to  $10^{11}$  GeV”. In: *35th International Cosmic Ray Conference*. Trieste, Italy: Sissa Medialab, 2017, p. 533 (cit. on pp. 21, 57, 58, 90).
- [66] M. G. Aartsen et al. “Computational Techniques for the Analysis of Small Signals in High-Statistics Neutrino Oscillation Experiments”. In: (2018). arXiv: 1803.05390 [physics.data-an] (cit. on pp. 65, 66).
- [67] Koji Niita, Tatsuhiko Sato, Hiroshi Iwase, et al. “PHITS – a particle and heavy ion transport code system”. In: *Radiation Measurements* 41.9 (2006). Space Radiation Transport, Shielding, and Risk Assessment Models, pp. 1080–1090 (cit. on p. 66).
- [68] M. Honda, T. Kajita, K. Kasahara, and S. Midorikawa. “Improvement of low energy atmospheric neutrino flux calculation using the JAM nuclear interaction model”. In: *Physical Review D* 83.12, 123001 (2011), p. 123001 (cit. on p. 66).

- [69] Erwan Thébault, Christopher C. Finlay, Ciarán D. Beggan, et al. “International Geomagnetic Reference Field: the 12th generation”. In: *Earth, Planets and Space* 67.1 (2015), p. 79 (cit. on p. 66).
- [70] J. Becker Tjus A. Fedynitch and P. Desiati. *crflux 1.0.Orc1 documentation*. 2019. URL: <https://crfluxmodels.readthedocs.io/en/latest/index.html#> (cit. on p. 66).
- [71] A. A. Kochanov, A. D. Morozova, T.S. Sinegovskaya, and S. I. Sinegovsky. “High-energy atmospheric muon flux calculations in comparison with recent measurements”. In: *J. Phys. Conf. Ser.* 1181.1 (2019), p. 012054 (cit. on p. 72).
- [72] N. Agafonova et al. “Final Results of the OPERA Experiment on  $\nu_\tau$  Appearance in the CNGS Neutrino Beam”. In: *Phys. Rev. Lett.* 120.21 (2018), p. 211801 (cit. on p. 74).
- [73] Z. Li et al. “Measurement of the tau neutrino cross section in atmospheric neutrino oscillations with Super-Kamiokande”. In: *Phys. Rev.* D98.5 (2018), p. 052006 (cit. on p. 74).
- [74] Stephen Parke and Mark Ross-Lonergan. “Unitarity and the three flavor neutrino mixing matrix”. In: *Phys. Rev.* D93.11 (2016), p. 113009 (cit. on p. 74).
- [75] Eun-Joo Ahn, Ralph Engel, Thomas K. Gaisser, Paolo Lipari, and Todor Stanev. “Cosmic ray interaction event generator SIBYLL 2.1”. In: *Phys. Rev.* D80 (2009), p. 094003 (cit. on p. 89).
- [76] Felix Riehn, Ralph Engel, Anatoli Fedynitch, Thomas K. Gaisser, and Todor Stanev. “Charm production in SIBYLL”. In: *EPJ Web Conf.* 99 (2015), p. 12001 (cit. on p. 89).
- [77] M. Thunman, G. Ingelman, and P. Gondolo. “Charm production and high energy atmospheric muon and neutrino fluxes”. In: *Astroparticle Physics* 5.3 (1996), pp. 309–332 (cit. on p. 89).
- [78] Joerg R. Hoerandel. “On the knee in the energy spectrum of cosmic rays”. In: *Astropart. Phys.* 19 (2003), pp. 193–220 (cit. on pp. 89, 90).
- [79] V. I. Zatsepin and Natalia V. Sokolskaya. “Three component model of cosmic ray spectra from 100 GeV up to 100 PeV”. In: *Astron. Astrophys.* 458 (2006), pp. 1–5 (cit. on pp. 89, 90).
- [80] Andreas Haungs et al. “Investigating the 2nd knee: The KASCADE-Grande experiment”. In: *J. Phys. Conf. Ser.* 47 (2006), p. 238 (cit. on p. 90).
- [81] Anatoli Fedynitch, Julia Becker Tjus, and Paolo Desiati. “Influence of hadronic interaction models and the cosmic ray spectrum on the high energy atmospheric muon and neutrino flux”. In: *Physical Review D* 86.11, 114024 (2012), p. 114024 (cit. on p. 90).
- [82] M. L. Good and W. D. Walker. “Diffraction Dissociation of Beam Particles”. In: *Phys. Rev.* 120 (5 1960), pp. 1857–1860 (cit. on p. 91).

- [83] Christian Bierlich, Gösta Gustafson, and Leif Lönnblad. “Diffractive and non-diffractive wounded nucleons and final states in pA collisions”. In: *JHEP* 10 (2016), p. 139 (cit. on p. 92).